DEVELOPMENT AND CHARACTERIZATION OF EXTRACELLULAR MATRIX INSPIRED PEPTIDES FOR NANOPARTICLE SELF-ASSEMBLY

by

Lucas C. Dunshee

A thesis submitted to the Faculty of the University of Delaware in partial fulfillment of the requirements for the degree of Master of Chemical Engineering

Fall 2017

DEVELOPMENT AND CHARACTERIZATION OF

EXTRACELLULAR MATRIX INSPIRED PEPTIDE FOR

NANOPARTICLE SELF-ASSEMBLY

by

Lucas C. Dunshee

Approved: _____
Millicent O. Sullivan, Ph.D.
Professor in charge of thesis on behalf of the Advisory Committee

Approved: _____
Kristi L. Kiick, Ph.D.
Professor in charge of thesis on behalf of the Advisory Committee

Approved: _____
Eric M. Furst, Ph.D.
Chair of the Department of Chemical & Biomolecular Engineering

Approved: _____
Babatunde A. Ogunnaike, Ph.D.
Dean of the College of Engineering

Approved: _____

Ann L. Ardis, Ph.D.
Senior Vice Provost for Graduate and Professional Education

DEDICATION

This work is dedicated to my grandfather, Roger Leo Hingtgen.

You will be missed but not forgotten as the joy and love you created carry on.

ACKNOWLEDGMENTS

Thank you first and foremost to my advisers Professor Millicent O. Sullivan and Professor Kristi L. Kiick, for providing me with the resources and guidance necessary to complete this work. In the past year I have learned a great deal about the best ways to go about doing good science, formulating hypotheses, and overall obtaining a higher level of critical thinking. You both have been of great aide to me in these regards, and for that I am profoundly grateful.

I would also like to thank the members of my committee, Professor Christopher J. Kloxin and Professor Wilfred Chen, for their continued support and guidance. You both have probably been of more guidance to me than you may realize, and the lessons you both have provided me are well remembered.

Additionally I am grateful to both the Sullivan and Kiick lab members for their support in all of my endeavors. A degree of extra thanks are given to the Sullivan lab group for countless discussions, troubleshooting, and for imparting me with an overall feeling of wellbeing and joy. The large majority of group members from both groups have provided advice or support in one form or another to me and I consider myself lucky to have you all as colleagues. Special thanks are given to Dr. Morgan Urello and Dr. Tianzhi Luo for their roles as mentors and for efforts in my initial training in nearly all respects of lab work.

There are several other individuals that have been of assistance to me in the past year for which I am particularly grateful for. I'd like to thank Dr. Papa Nii Asare-Okai for his assistance and discussions related to mass spectrometry and the mass

directed purification system. I'd like to also thank Dr. Yong Zhao, Dr. Jennifer Sloppy, and Shannon Modla for their guidance, assistance, and overall support related to all things with TEM. Thanks are also given to Rachel Edelstein for providing access and use of the Day group sonicator probe and microcentrifuge equipment for a project mostly unrelated to the one presented here. I would also like to thank Eric Fowler for his willingness to hear out my troubleshooting ideas and for our countless discussions regarding peptide synthesis and purification.

I would like to thank Rachel Lieser for always being there for me through thick and thin. Your support of me and my work is unmeasurable and I will be forever grateful for that. The past five years have been an absolute treasure and I can't wait to see what the future has in store.

Lastly, I would also like to thank my family for their everlasting support and love. We may be half the country away but the mental and emotional support you all have provided to me have aided me just as it would if you were here.

TABLE OF CONTENTS

LIST OF TABLES

LIST OF FIGURES

ABSTRACT

The extracellular matrix (ECM) is a dense mesh-like network of proteins, proteoglycans, and glycoproteins that imparts physical stability to tissues and plays key roles in cell signaling and behavior such as cell adhesion, proliferation, differentiation, and survival. Physiochemical irregularities or disruptions to certain components of the ECM, such as collagen, can lead to diseases like osteogenesis imperfecta, and osteoarthritis. Current systemic delivery approaches to treat such diseases suffer from off-target effects, suggesting a significant need for ECM targeted therapeutics.

In the last decade ECM inspired polypeptide materials, including elastin like peptides (ELPs) and collagen-like peptides (CLPs), have garnered significant interest in the field of drug delivery. This is owed to the general biocompatibility and thermoresponsivity of both peptides, but also the ability of CLP to target and hybridize to denatured collagen protein in the body. Recently, our group has reported on the assembly of thermoresponsive elastin-*b*-collagen like peptide nanovesicles that are capable of dissociating at high temperature (70°C). In an effort to modify this temperature of dissociation, and in turn the temperature of CLP-collagen hybridization, a small library of CLP sequences was synthesized. The propensity of four different CLP sequences to form triple helices was measured using circular dichroism wavelength scans and the melting temperatures for each were determined. Characterization of the inverse transition temperature of two different ELP sequences

was also completed through light scattering experiments to ensure its role in nanoparticle formation.

Lastly the conjugation of a particular ELP to a small selection of CLPs was performed and characterized for their ability to form nanoparticles. The melting temperature and repeat length of the CLP domain was found to be of critical importance to nanoparticle formation, with one CLP forming particles, while the same CLP with a single repeat unit shorter was not. The ability of these two conjugate systems to form nanoparticles was correlated with their overall triple helical stability and melting temperature. Additionally, the conjugate that was shown to form particles was found to possess characteristics that were more idealized for drug delivery than the previous system. Future work will be focused on determining if the effect of the nanoparticle formation and lower critical solution temperature properties of the particle is a result of CLP triple helical melting temperature or simply an artefact of assembly of a particle with a smaller hydrophilic volume fraction.

Chapter 1

INTRODUCTION AND MOTIVATION

The extracellular matrix (ECM) is a three dimensional acellular microenvironment comprised of macromolecular fibrous proteins (such as elastin, collagen, and fibronectin), glycoproteins, and proteoglycans that forms the basis for all tissues that are essential for multicellular organisms.[1,2] The most obvious function of the ECM is the structural and mechanical stability it provides as a scaffold to cells. However, the ECM also plays a role as a dynamic regulator of cell migration, proliferation, differentiation, and survival, among other functions.[3] Dysregulation of any of these processes that are required for tissue development and homeostasis can lead to diseased states such as cancer, fibrosis, and bone disorders.[1,4,5] Collagen in particular, given its abundance and ubiquity in the ECM, is well known to be a central figure in many of these ECM diseases including cancer.[6,7]

Similar to other biological targets, systemic delivery of 'free' drugs to collagens to treat these diseases can come with a variety of limitations including poor biodistribution (negative off target side-effects), rapid drug clearance, lack of target selectivity, and tissue damage due to extravasation.[8] While certain nanocarriers functionalized with collagen targeting anti-bodies have been explored as a means to circumvent some of the issues with systemic delivery, target specificity for diseased tissue remains a challenge for ECM drug delivery.[9,10]

This chapter will begin in section 1.1 with a brief discussion of collagen in disease, specifically relating to collagens role in cancer and other diseases. In section

1.2 the structure and characteristics of the collagen-like peptide will be introduced, followed by its unique targeting properties to denatured native collagen protein in the body. From there an idealized drug delivery system for ECM targeting is envisioned in section 1.3 and discussed. Section 1.4 we will highlight the elastin-like peptide its properties and how those properties can be exploited in drug delivery systems. Lastly, the elastin-like-block-collagen-like peptide nanoparticle, its thermal characteristics, cell viability and uptake, and its desired modifications to better suit drug delivery will be discussed in section 1.5.

1.1 Collagen in Disease

1.1.1 Brief background of collagen

Collagen is not only the most ubiquitous protein in the ECM, but is overall the most abundant protein in the human body.[10,11] To date, there are 28 known types of collagens that are comprised of at least 46 unique polypeptide chains.[12] The collagen family has historically been categorized into two distinct groups, fibrillar and network forming collagens, though there are three other categories for collagens with interrupted secondary structures.[12]

The chief characteristic of collagens is their unique secondary structure which is comprised of three parallel left-handed polyproline type II (type II designating the trans configuration for every proline residue) helical chains (often called α chains in collagen nomenclature) that coil with one another with a one residue stagger into a right handed triple helix.[12-14] In order to form these secondary structure characteristics, a glycine residue must occur at every third residue in the primary sequence due to the close packing required by this position in the folded state.[12] If the glycine residue is

not present then the triple helix is dramatically destabilized.[15] This is repetition of glycine is typically viewed as (Gly-X_{AA}-Y_{AA}) repeats where X_{AA} and Y_{AA} can be any amino acid, but in order to form the triple helix, the imino acids (proline or hydroxyproline) must make up a large proportion (about 20%).[12,13,15] The large number of imino acids stereochemically restrict the chains to the polyproline(II) confirmation and together with interstrand N-$H_{(Gly)}$···O=$C_{(Xaa)}$ hydrogen bonds, stabilize the triple helix structure.[13,15]

The three polyproline strands in the triple helix can either be homotrimers or heterotrimers depending on the type of collagen. As an example, collagen type II is a homotrimer found in cartilage, while collagen type IV is a heterotrimer found in basement membranes.[7.12] Other collagens of various types are found all over the body ranging from collagen VIII in the brain and heart, collagen III in the skin and intestine, and collagen IX in the cornea.[7,12] It should be noted that the various tissues that contain collagens are heterogeneous with regard to the types located in that tissue. For instance, cartilage contains predominately collagen type II but also contains small amounts of collagens VI, IX, X, XI, and XIV.[12]

1.1.2 Collagens role in cancer

Cancer is the second leading cause of death in the United States.[16] Among the vast body of literature regarding cancer is a growth in the understanding of the tumor microenvironment, which has been of specific interest in the last decade.[17] The collagen family, as part of the tumor microenvironment, plays a complex and diverse role in tumor progression.

As a tumor progresses to a more malignant stage, it begins to alter nearby collagen scaffolds significantly. One alteration is the deposition of abundant amounts

of collagen type I and fibronectin by cancer-associated fibroblasts (CAFs).[18] However, the collagen and fibronectin deposited are post translationally modified and as a result, have increased stiffness. The deposited fibronectin becomes partially unfolded (exposing cryptic binding sites) and leads to increased stiffness and binding to ECM molecules such as glycosaminoglycans. The deposited collagen I becomes linearized and crosslinked by lysyl oxidase or transglutamination, also leading to an increase in rigidity.[18] The net effect of the modified excess ECM molecules is enhanced tumor stiffness which in turn effects cell differentiation, proliferation, migration, and survival, ultimately driving tumor progression.[18,19] Indeed, the increased linearity and stiffness of collagen I may mechanistically activate integrin binding sites, thereby making collagen fibers an invasion 'highway' for cancer cells.[19]

The excessive breakdown of existing collagen networks by ECM proteinases is also critical in tumor growth and metastasis. This is because the ECM can act as a physical barrier to cancer cell growth and invasion. Of the ECM proteinases, matrix metalloproteinases (MMPs) have been specifically implicated in cancer for more than 40 years.[20,21] In healthy physiological conditions, MMPs are tightly regulated on many levels including transcription, activation, interactions with the ECM, and specific inhibitors.[21,22] However, in the tumor microenvironment, MMPs have increased expression that is induced by tumor promoters, cytokines, growth factors, and physical stress among others.[23] This increased expression leads to the MMP mediated degradation of ECM (in particular collagen types I and IV) and leads to cancer cell invasion and metastasis.[19-23] However, these enzymes do more than simply degrade collagen and other ECM components; they also affect cell signaling pathways, angiogenesis, and the inflammatory response, along with other specific functions.[21] As

seen in Figure 1.1, all of these factors contribute to cancer cell proliferation, invasion, and, metastasis.[21,23]

The tumor microenvironment has become of great interest due to its susceptibility to 'passive' targeting drug delivery strategies. However, the role of MMPs and their degradation of ECM in the tumor microenvironment may also offer promising active targets for drug delivery as will be discussed in section 1.3.

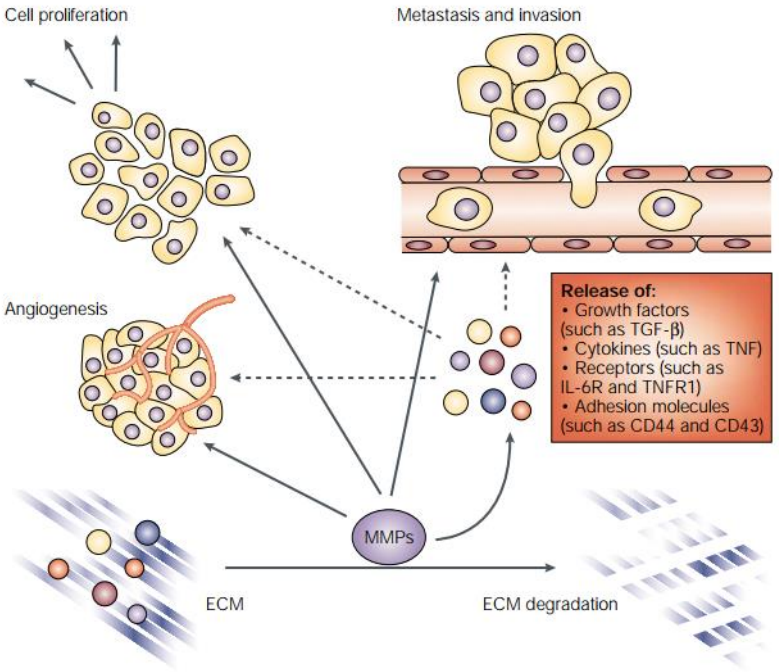

Figure 1.1: The role of MMPs in ECM breakdown, angiogenesis, cell proliferation, and tumor invasion and metastasis. Reprinted by permission from Macmillan Publishers Ltd: Nature Reviews Cancer. Rao, J. S., Molecular mechanisms of glioma invasiveness: The role of proteases. Nature Reviews Cancer 2003, 3 (7), 489-501.[23] copyright 2003.

1.1.3 Collagen in other diseases

Besides cancer, collagens role in other diseases has been well characterized. In at least 12 types of collagens, more than 1000 different mutations leading to human disorders have been identified, yet estimates suggest that the number of uncharacterized collagen mutations is extremely large.[24] Common diseases associated with collagen and its mutations include: osteogenesis imperfecta (OI), Ehlers-Danlos syndrome, Marfan's syndrome, and Alport syndrome.[24,25]

In some of these diseases (such as OI), the majority of mutations take place with a single base substitution of glycine codons.[26] As previously discussed, the substitution of a glycine residue for any other amino acid can have a dramatic destabilization effect on the triple helical secondary structure.[15] Even minor changes such as an glycine to alanine substitution (difference of a single methyl group) can destabilize the triple helix and can lead to both physiochemical and cell-matrix (or even cell phenotype) alterations.[25-27] In OI, more than 150 unique mutations have been identified in the α(1 or 2) chains of collagen type I, with glycine substitutions taking place at varying sites along the chains.[26] The substitutions cause abnormal fibril assembly, delayed collagen folding, increased intracellular breakdown, and other abnormal effects to collagen function that ultimately result in the symptoms of poorly mineralized/brittle bones that are found in OI.[26]

Ehlers-Danlos syndrome is a disease marked by skin hyperextensibility, joint hypermobility, and possibly skeletal deformities and organ rupturing.[24] The disease has many subtypes, but like OI, the most common subtypes (I and II) possess either a glycine to arginine substitution in collagen type V, or a cysteine to arginine substitution in the X_{AA} position of a (G-X_{AA}-Y_{AA}) triplet in collagen type I.[24,28]

Other diseases, relate to collagen as a result or progression of the disease rather than being the direct cause of the disease. Rheumatoid and osteoarthritis (RA and OA respectively), like cancer, possess upregulated MMPs that degrade collagens in the ECM of joints.[25,29] While the etiology of these diseases still remains poorly understood, some of the details of their pathophysiology have been determined.[30,31]

RA is an autoimmune disorder marked by an aggressive proinflammatory state where the synovium is inundated with inflammatory cells like CD4+ T-cells that produce cytokines such as TNF-α that upregulate MMP production.[32,33] This ultimately results in the breakdown of underlying subchondral bone and articular cartilage (particularly collagen type II).[30,32] In the last decade new monocolonal antibody therapeutics such as TNF-α inhibiting Adalimuab®, have been developed and have shown good efficacy for treatment of RA.[32] Yet the drug still faces significant safety concerns regarding negative side-effects such as the overall suppression of the immune system leading increased risk of infection.[34] Therefore, modern treatments of the disease still leave something to be desired for future therapeutics to be developed.

In OA, the inflammatory state and ECM degradation are not a result of an aberrant immune response, but rather the result of joint wear and tear combined with subtle genetic factors that manifest with age.[35] Similar to RA, the same cytokines (TNF-α) and MMPs are produced by chondrocytes and ultimately result in the degradation of the collagen II ECM found in the joint cartilage.[36]

Given the abundance of collagen throughout the human body it is no surprise that it is either responsible or takes part in a number of different diseases and disorders. The diseases can range from a single glycine residue alteration to the

overproduction/over degradation of collagen proteins. As will be briefly discussed in sections 1.2 and 1.3, the over degradation of collagen protein may offer a unique methodology of ECM drug targeting and delivery.

1.2 Collagen-like Peptides

1.2.1 Background, characteristics, and properties of collagen-like peptides

Collagen-like peptides (CLPs), also known as collagen-mimetic peptides (CMPs), collagen-hybridizing peptides (CHPs), or collagen related peptides (CRPs), are short synthetic peptides that follow the $(G\text{-}X_{AA}\text{-}Y_{AA})_n$ sequence motif found in natural collagen.[12,37,38] Like collagen, CLPs can form the right handed triple helical secondary structure composed of three staggered parallel left-handed polyproline type II α chains, so long as glycine is every third residue and there is a high proportion of imino acids in the X_{AA} and Y_{AA} positions.[12,13,15,38] Just as with collagen protein, these requirements are necessary due to the close packing of glycine inside the wound chains and the favorable conformational stability of polyproline type II created by the stereochemical restrictions of the imino acid rings. The triple helical structure of CLPs can be thought of as long rods with a dimeter of approximately 1 nm and the typical lengths of CLPs studied range from 6 to 15 repeats (approximately 5 to 13 nm in length) compared to native collagen type I which has 338 repeats and is about 300 nm long.[12,39,40]

Native collagen proteins are bulky and insoluble, and as a result, they are extremely difficult to study.[12] Because of this, CLPs were developed in order to better understand the structure and folding properties collagen.[12,39]

Through the use of CLPs, the first crystal structure of a triple helical protein was ascertained by Bella *et al*, and with it, a confirmation of the $N\text{-}H_{(Gly)}\cdots O{=}C_{(Xaa)}$ peptide backbone hydrogen bond that had previously only been suggested by Rich and Crick via fiber diffraction.[41] Later studies found evidence of alpha carbon hydrogen bonding ($C^{\alpha}\text{-}H_{(Gly/Yaa)}\cdots O{=}C_{(Xaa/Gly)}$) as well as extensive water hydrogen bonding networks that occurred between the different chains carbonyl and hydroxyproline hydroxyl groups.[40,43] These reports highlight the important enthalpic stabilization characteristics of both interchain hydrogen bonds as well as the aqueous solvent in contributing to the already entropically stabilized triple helical structure established by stereochemistry of the imino acid rings. It was through these studies that the extra stability of CLP triple helices imparted by hydroxyproline residues was thought to be confirmed due to the observed hydrogen bonding network of water and hydroxyproline's hydroxyl group. But as will be discussed shortly, the role of hydroxyproline as a triple helical stabilizer is less salient than only being an extra hydrogen bonding partner.

It was also through the use of CLPs that insights into triple helical folding mechanisms were found. Folding of collagen and collagen like peptides can be studied with nuclear overhauser effect spectroscopy (NOESY) via nuclear magnetic resonance spectroscopy or by circular dichroism (CD) spectroscopy.[43] The circular dichroism spectra of triple helical collagens and CLPs is extremely unique, with a global maximum molar ellipticity peak found at 225 nm and a global minimum molar ellpticity found at 200nm.[44] The helix to coil transition is typically monitored at 225nm as a function of time, temperature, or other parameters.[43,44] It is by this method

that folding kinetics, thermodynamic parameters, and the melting temperature of CLPs can be calculated, and the underlying folding mechanisms determined.[43,45]

While there are still aspects of the triple helix formation mechanism that need to be more thoroughly investigated, a couple of key features of triple helix folding have been identified.[46] In low concentrations of CLP monomer, the rate of folding is limited by the formation of dimeric or trimeric intermediates prior to a full-fledged triple helical nucleation and folding for which third order reaction kinetics are observed.[46,47] When the concentration of CLP monomer is higher, nucleation readily occurs and the propagation of triple helical folding along the chains becomes the rate limiting step with first order reaction kinetics.[47]

This propagation step is predominantly limited by cis-trans isomerization of the imino acid peptide bonds. The collagen triple helix requires that all peptide bonds be in the trans configuration.[12] In the random coil state, most amide bonds preceding non-imino acids are largely in the trans state.[45] For the imino acids, this is not the case because of the partial double bond character and the planarity of the imino rings and as a result, tend to be in a cis state in higher proportion.[45] Therefore, in order to form the triple helix, these cis isomers must be converted to the trans configuration. The cis-trans isomerization in the propagation step has been confirmed experimentally with observations of unusually high activation energies in CLP folding which are indicative of the isomerization process.[46,47]

This cis-trans isomerization step is probably best exemplified by CLPs that possess trimerization folding domains. These folding domains act as an exogenous nucleation site that inherently increase the local concentration of the individual CLP chains and therefore eliminate the CLP nucleation step altogether.[47] Such trimerized

CLPs are independent of CLP monomer concentration and for certain CLPs, the initial folding step has a reaction order of zero.[47] The typical trimerization domains mimic those seen *in vivo* such as the T-4 phage fibritin foldon protein (see refs 45 & 47) or cysteine residue rich C termini termed cysteine knots, that share resemblance with collagen type III and its cysteine nucleating C-terminus.[38,46,47] In the case of cysteine knots, disulfide bonds form across triple helices and crosslink the CLP monomers so long as they are oxidized.[46] Most CLPs studied are homotrimers and it is a common misconception to think they always fold from C to N terminus (it is likely that nucleation can occur at any site for CLPs).[45,48] However, cysteine knots have been employed as both N and C terminal nucleators and have also been used to make synthetic CLP heterotrimers.[49,50] Other methods of making CLP heterotrimers have been developed and are not reviewed here.[12,39] The studies of CLPs and their folding have provided valuable insight into collagen folding *in vivo*, particularly with respect to the propagation step.[45] The lessons learned from CLP folding studies are also of importance to the growing use of CLPs in the materials science field.

While the kinetics and folding of CLPs are useful for their theoretical insight and to some small degree, their practical purposes; the melting temperature (T_m) of CLPs is possibly of greater importance and interest to many CLP scientists. As mentioned, CLPs have the generalized sequence of $(G\text{-}X_{AA}\text{-}Y_{AA})_n$. Both the number of repeats and the type of residues that fill the X_{AA} and Y_{AA} can dramatically alter the T_m of CLPs.[12,38] The most stable repeat sequence (excluding specialized residues) is $(G\text{-}P\text{-}O)_n$ (O is single letter code for hydroxyproline) and is also the most common repeat sequence found in collagen.[51] As illustrated by this sequence, the lower the repeat number n, the lower the T_m becomes, with n=10 ($T_m \approx 65$ °C) and with n=7 ($T_m = 36$

°C).[12] This is intuitively the result of reduced entropic preorganization and because of a smaller number of hydrogen bonds that shorten the enthalpic barrier needed to unfold the triple helix. What is less intuitive however is the dependence on the T_m of any of the 20 other amino acid residues that are substituted into the X_{AA} and Y_{AA} positions.

Fortunately, in the late 1990s and early 2000s, the Brodsky research group extensively pursued this line of study to assess the propensity of other amino acids for triple helix stability.[15,27,48,51] In their works, a model host-guest CLP peptide with the sequence Ac-$(GPO)_3$-$(G\text{-}X_{AA}\text{-}Y_{AA})$-$(GPO)_4$GG-$NH_2$ was used to test and compare amino acid substitutions for the X_{AA} and Y_{AA} positions and their corresponding melting temperatures.

A small summary of the results by the Brodsky research group can be found in refs. 26 and 45, but the results of ref. 27 will be briefly discussed here. In the study the host guest system substituted one residue at a time with the host tripeptide being either $(G\text{-}X_{AA}\text{-}O)$ or $(G\text{-}P\text{-}Y_{AA})$. The difference in amino acid sidechains could play many roles in triple helical stability such as entropic stabilization of the individual polyproline chains or ethalpic stabilization by guest residue sidechain interactions with solvent and amide groups. From their studies it was confirmed that proline in the X_{AA} position and hydroxyproline in the Y_{AA} position yield the most stable triple helical peptide out of all the other residue combinations studied, most likely because of the entropic contributions gained by the imino rings as well as hydrogen bonding with hydroxyprolines hydroxyl group.[27] Almost any substitution of other amino acids in either position resulted in a less stable triple helix. It should be noted that the X_{AA} and

Y_{AA} positions are not equivalent (GFO $T_m \neq$ GOF T_m) due to differences in the availability of amide groups to interact with the solvent and other chains.[26,27]

The general trends showed that aromatic residues and glycine caused the most significant destabilizing effects when substituted into either position.[27] The destabilization by aromatic residues is most likely explained by steric effects and the potential for bulky sidechains to block solvent availability to the triple helical chain. Glycine is thought to play a destabilizing role due to its ability to adopt numerous φ and ψ torsional angles.[27] Interestingly, arginine showed significant stability when in the Y_{AA} position and this was attributed to its potential for hydrogen bonding with a nearby carbonyl group in the backbone.[27,45] For similar reasons, other charged residues were found to also contribute to triple helical stability. In later studies the use of adjacent oppositely charged residues were used to stabilize the triple helix through electrostatic interactions.[52-54]

The accepted explanation for non-imino acid triple helical stabilization is due to the interaction of amino acid side chains either with each other, amide carbonyl groups, or solvent hydrogen bonding interactions. However, for a time the same explanation had been accepted for the role of hydroxyprolines significant stabilization effect compared to proline containing CLPs alone. For example, the CLP $(GPP)_{10}$ has a $T_m \approx 36°C$, while $(GPO)_{10}$ has a $T_m \approx 65°C$.[12] Through the work of Bella *et al* in obtaining the crystal structure of CLPs, a hydrogen bond network was observed interacting with the hydroxyproline hydroxyls. As a result, the extra stability of hydroxyproline was believed to be rooted through these hydrogen bond interactions.[41]

An alternative hypothesis for this observation was postulated by Raines *et al* that the inductive or electron withdrawing effect of the hydroxyl moiety was the

source of $(GPO)_n$ sequence stability.[12,55] In an effort to test this hypothesis, Holmgren *et al.* created a CLP that contained fluoroprolines in place of hydroxyprolines in the Y_{AA} position.[55] The use of fluoroprolines effectively swapped the hydroxyproline hydroxyls with fluorine atoms. Because fluorine atoms cannot form strong hydrogen bonds, a stabilizing water hydrogen bonding network could not form and the resulting triple helix would be expected to be less stable if these water mediated hydrogen bonds were actually important. Furthermore, the role of the inductive effect could be explored due to fluorine being the most electronegative atom and therefore impart a strong electron withdrawing effect. Instead of observing a destabilized triple helix as a result of the substitution (as expected with a lack of a hydrogen bonding network), a hyperstable CLP was observed with a T_m of 91°C.[55]

In later studies it was found that this hyper stabilization only occurred for CLPs comprised of (2S-4R)-4-fluoroprolines, with CLPs made of the diastereomer (2S-4S)-4-fluoroprolines not forming triple helices at all.[56] Similar observations were made in the past with (2S-4S)-4-hydroxyprolines which were also unable to form triple helices. Therefore the extra stability of these CLPs is the result of a stereoelectonic effect instead of an inductive effect alone.[57]

The underlying effect of this stereo specific triple helix formation was the difference in pyrrolidine ring puckering confirmations imparted by the two epimers. The (2S-4R) diastereomers were found to impart a C^{γ}-*exo* puckering confirmation while the (2S-4S) diastereomers led to a C^{γ}-*endo* puckering.[58] With regard to the Y_{AA} residue position, the C^{γ}-*exo* configuration is more conducive to preorganizing chains into the triple helical confirmation and entropically drives and stabilizes this structure.[58] It is through these influential studies that at last hydroxyprolines role as a

stabilizer was uncovered. While a hydrogen bonding network is present with hydroxyproline's hydroxyl groups, its overall contribution to triple helical stability is insignificant.[12,45] The use of hyperstable triple helices is an interesting prospect for the application of thermally stable CLPs in various material science settings where stiff triple helical rods might be favored such as hydrogels, various supramolecular assemblies, among others.

Another interesting aspect of CLPs is their facile inclusion of unique bioactive sequence motifs that are capable of cellular engagement. A number of bioactive peptide sequences have been discovered that engage a broad range of protein or cellular targets.[59] In 1995, Knight *et al* discovered that the triple helical six residue sequence GFOGER was able to successfully bind to the $\alpha_1\beta_1$ and $\alpha_2\beta_1$ integrins.[60] Since then the sequence has been employed in CLPs broadly ranging in applications from simple cell binding and differentiation studies to macroscopic bone repair.[61,62] Unlike many other bioactive peptide sequences that can be incorporated into various structural states, the GFOGER sequence is restricted to CLPs.[59] This is because its bioactivity is lost if the sequence is not in the triple helical conformation.[60] The Kiick research group has also identified a GFOGER like sequence, namely GEKGER, that was also shown to engage the $\alpha_2\beta_1$ integrins.[63] These bioactive sequences underscore a unique property offered by CLPs and their potential use in biotechnologies that are still being explored today.

1.2.2 Discovery of CLP hybridization with denatured collagen protein

Over the years CLPs have been used for numerous purposes. Their development was initially motivated to better understand the properties of native collagen proteins. In recent years considerable attention has been given to using CLPs

to assemble higher order collagen structures in the hope of finding a synthetic alternative to animal derived collagen.[12] Other CLP applications are still in their early stages of development including their use in hydrogels, bolus substrates for bone regeneration, and even their use as protease resistant materials.[62,64] However, their most promising and recent application is as a diagnostic tool for denatured collagen protein.

In 2005, the Yu research group published an influential paper that demonstrated the ability of collagen like peptides to bind and form triple helical structures with degraded collagen protein.[65] In this pioneering study, CLPs functionalized with a fluorescent dye were loaded onto collagen films at two different temperatures; one below the T_m of the CLP and one above. They found through fluorescence intensity measurements that the loaded CLP that had been heated (and as a result, in the single stranded conformation) was able to bind to the collagen film while the lower temperature (triple helical) CLP did not. This indicated that the single stranded CLPs were likely binding to loose strands of collagen protein. This binding process, sometimes referred to as 'strand invasion', is illustrated in Figure 1.2.[66]

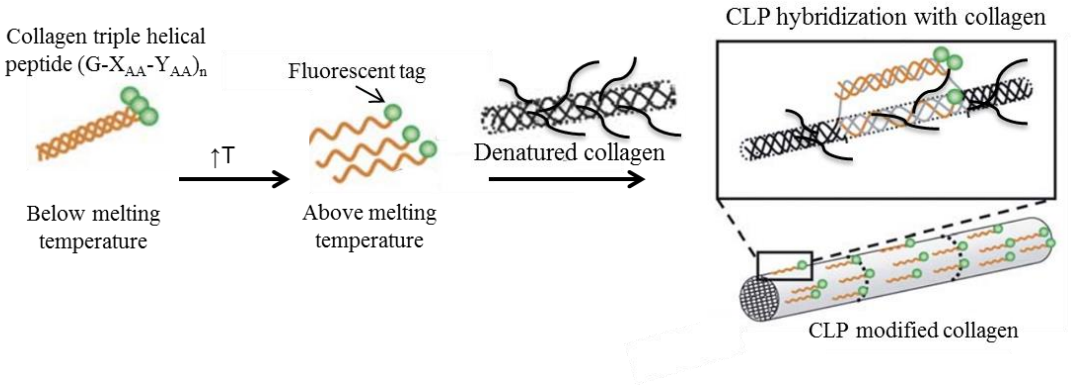

Figure 1.2: Melting of triple helical CLP followed by hybridization of CLP to denatured collagen protein. Adapted from Ref. 66 with permission from The Royal Society of Chemistry.

Furthermore, a scrambled CLP sequence that could not form triple helices at all was also unable to bind to collagen protein at any temperature, further supporting the fact that the CLPs that were binding did so in a conformationally specific manner such as triple helix formation.

A later study by the Yu group further investigated this phenomenon with a multitude of different sequences that were tested at different equilibration temperatures prior to the loading of fluorescent CLPs to collagen.[67] After assessing initial binding affinity, the collagen films were also incubated at various temperatures over the course of two weeks in order to study the release of the bound CLPs. Through these efforts, they found the optimal equilibration temperature for each peptide that corresponded with its highest binding affinity. It was also found that longer CLP sequences with higher melting temperatures had a much higher binding affinity for collagen films then their short sequence counterparts. Furthermore, these higher affinity CLPs released in a slow and continuous manner as opposed to a burst release seen for shorter CLPs. These observations were consistent with the expectation that

longer CLPs could associate with collagen in a ‘stronger’ manner than short CLPs because of extra availability of the CLP chain for forming more hydrogen bonds with the degraded collagen strands.[67]

A major short coming of these works was the need to thermally melt the CLPs prior to collagen binding. The higher T_m CLPs that possessed the best binding affinities had to be heated to physiologically irrelevant temperatures such as greater than 50 °C. Furthermore, their previous works indicated that even if higher temperatures are used, the heated CLP solutions themselves would degrade the collagen protein when loaded.[67] To circumvent this issue, the Yu group designed a CLP that possessed a photo cleavable nitrobenzyl group on a centralized glycine that caused triple helical destabilization until it was cleaved.[68] With this peptide they showed the same binding to denatured collagen protein as before, but without the need for thermal melting, making it physiologically applicable. With a physiologically relevant CLP-collagen hybridizer in hand, the group performed *in vivo* studies with infrared dyes conjugated to the N-terminus of the nitrobenzyl CLP. For these studies, mice with PC-3 prostate tumors were injected with ultraviolet (UV) irradiated CLP (cleavage of nitrobenzyl) solutions. As discussed above, the tumor microenvironment is known to have a significantly degraded ECM. As such, the single stranded CLPs can flow through the blood stream to the tumor site and ultimately bind with the denatured collagen matrix of the tumor.[68] Figure 1.3 below highlights the success of the treatment.

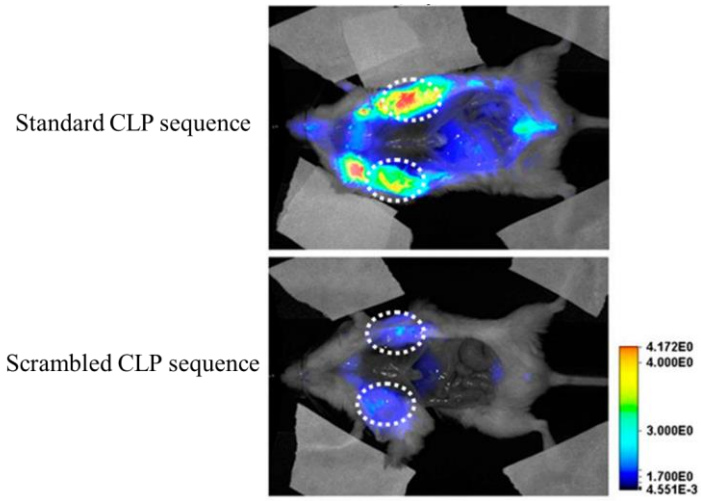

Figure 1.3: PC-3 prostate tumor bearing mice, 96 hours post administration of Uv irradiated CLP peptide solution injection. Mice are open chested for better image resolution. The heat map is fluorescence intensity of infrared dye, and white dashed ovals are the tumor location sites. The two images compare a standard CLP-collagen binding peptide and a scrambled sequence incapable of hybridization. Adapted from ref. 68 with permission.

As can be seen in Figure 1.3, the nitrobenzyl cleaved standard CLP was capable of binding to the tumor microenvironment as is evident by the abundance of infrared fluorescence detection of the conjugated dye. In contrast a scrambled CLP sequence incapable of forming a triple helix only showed minimal fluorescence in the tumor environment indicating that the ability to assemble triple helices was crucial to binding and retention. Given that the images are 96 hours post injection, it is likely that the scrambled peptide was eliminated through the urinary tract system prior to imaging.[68]

In the same article, CLPs were also shown to bind to the ECM of a mouse model for Marfan syndrome. Marfan syndrome is a genetic disorder of ECM where

significant collagen remodeling is implicated.[25] The fluorescence of the bound CLP in the Marfan mouse was at least four times that of the wildtype.[68]

These studies have laid the foundational work for CLPs direct application as a diagnostic tool for degraded collagen protein in the body. The demonstration of their use in these two distinct degraded collagen disease models shows promise for their use in similar collagen disease models, such as osteogenesis imperfect, arthritis, and Ehlers-Danlos syndrome.

1.3 Seeking a Stimuli Responsive and Collagen Hybridizing Drug Delivery Vehicle

There is no doubting the impact of fluorescent CLPs as a diagnostic tool for degraded collagen in the body. Yet so far the CLP hybridization technique has primarily been limited to diagnostics and imaging. From the discussion in section 1.1 there is sound motivation to target drugs specifically to the ECM for the treatment of ECM related diseases. Therefore, there is a significant opportunity to develop collagen targeting drug delivery vehicles using CLPs.

There have been few therapeutic applications of CLPs for denatured collagen protein targeting. Examples include the conjugation of therapeutic peptides to CLPs as well as CLP modified polyplexes for gene delivery.[69.70] While these applications have demonstrated the success of the CLP-collagen hybridizing method, they have so far been limited to topical or subcutaneous administration and rely on collagens natural turnover for eventual cargo delivery.

A CLP based stimuli responsive nanocarrier would therefore be advantageous in multiple respects. Nanocarriers (also nanoparticles) have been shown to increase drug circulation in the blood, ensure the viability of drug cargo, can be modified with

stealth or bioactive motifs, and in some cases carry two therapeutics at once.[8,71] Furthermore, a CLP-collagen hybridizing nanoparticle with a stimuli responsive drug release mechanism would enable the ECM to be used as an active drug reservoir rather than relying on collagen turnover mechanisms for delivery. In the following section another ECM mimetic is introduced that may be important for its stimuli responsiveness.

1.4 Elastin-like Peptides

1.4.1 Characteristics and properties of elastin-like peptides

With a singular name, elastin-like peptides (ELPs) are short synthetic polypeptides that are composed of a repeat sequence of $(V\text{-}P\text{-}G\text{-}X_{AA}\text{-}G)_n$, where X_{AA} can be any residue except proline.[72] This repeat sequence is derived from tropoelastin, a soluble monomeric precursor of elastin protein.[72] Other repeat sequences identified from elastin include $(APGVGV)_n$ and $(VPGG)_n$, yet the pentapeptide repeat has been the primary interest of study for many years.[73] Standard repeat lengths studied range from short ELPs ($n\approx5$) to long polypeptides where n can be in the one to two hundreds.[73]

The principal characteristic of ELPs is their possession of a lower critical solution temperature also known as an inverse temperature transition, or simply transition temperature (T_t), in which ELPs undergo a transition from a soluble to insoluble phase.[72-74] Below the T_t the ELP is soluble in aqueous solutions. Since ELPs are primarily composed of hydrophobic residues the ELP is said to solubilized by hydrophobic hydration in which the ELP chain is in a random coil extended state that is fully hydrated.[73,74] The water molecules surrounding these non-polar residues are

actually more ordered in comparison to bulk water and are conformationally akin to gas clathrate cages such as methane hydrate.[74] Upon heating the solution above the transition temperature of the ELP, the ordered water surrounding the chains transfers to the bulk liquid and the chains become dehydrated and collapse to a folded state.

More specifically, the folded state is a β-spiral that is composed of type II β-turns (different types vary by their backbone torsional angles φ and ψ; see ref 76).[75,76] Every pentamer forms one β-turn and approximately three pentamers make up a single turn of the β-spiral.[73-75] The β-spiral is stabilized by intraturn and intraspiral hydrophobic contacts and additional contacts are made between spirals as well. Additionally, a hydrogen bond is present between the first valine residue and the guest residue ($C{=}O_{(Val)}\cdots H\text{-}N_{(Xaa)}$) of every pentamer.[75] The formation of insoluble coacervates is started by the association and intercalation of three β-spiral chains into a fibrillar structure and the insoluble phase is completed by the growth and aggregation of these filaments into micrometer sized particles.[73] This inverse transition phase separation process is illustrated in Figure 1.4 below.

The transition temperature that the ELP possesses can be tuned and modified based on numerous system parameters and conditions. Such conditions that affect the transition temperature include: concentration of ELP, length or repeat number n of pentamers, added salts (following Hofmeister series), ELP amino acid composition (X_{AA} position), conjugated moieties or chemical modifications, and many others.[74]

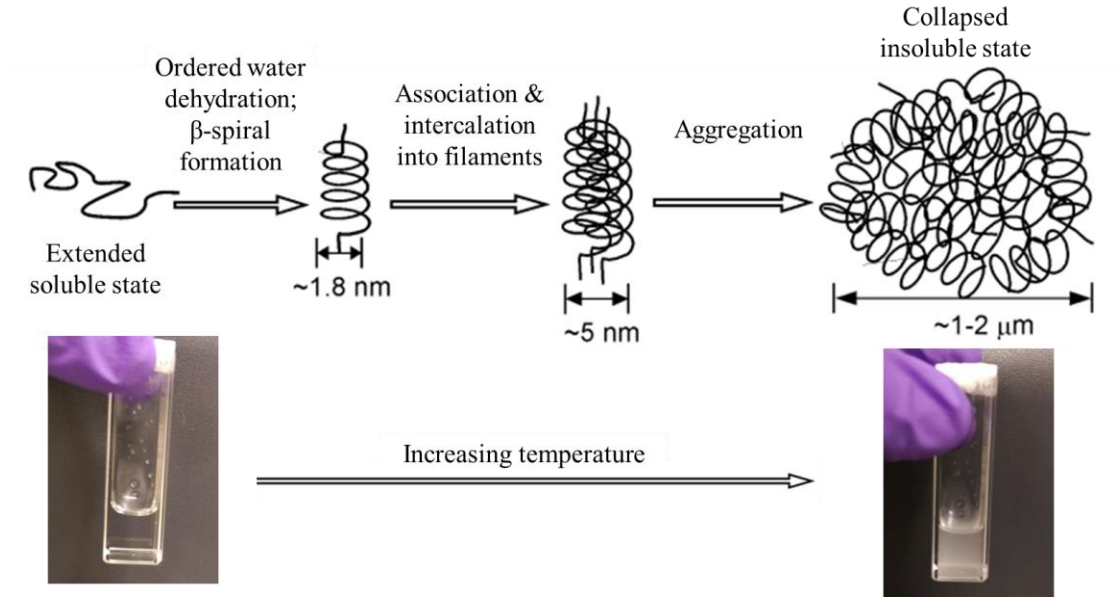

Figure 1.4: Illustration of the ELP inverse transition temperature phase separation mechanism. Solubilized ELP in the extended state becomes insoluble aggregates through β-spiral chain-chain association. Representative experimental images are depicted for the extended and collapsed states. Adapted from Ref. 73 with permission.

If one wanted to lower the transition temperature of an ELP they could increase the repeat length (n) of the chain, increase the peptides concentration, increase the ionic strength of the aqueous medium, or replace the guest residue with more hydrophobic amino acids.[74] In fact the observation of the effect of T_t with regard to amino acid hydrophobicity led to the suggestion that the transition temperature be used as a new amino acid hydrophobicity scale.[72,74] Indeed Urry and coworkers developed such a scale by measuring the transition temperature of an ELP with the sequence (f_v(VPGVG),f_x(VPGXG)) in which f_v and f_x are the mole fractions of each pentamer and X is the guest residue being studied. By varying mole fractions of each pentamer, as well as the X guest residue, a relative hydrophobicity scale was generated

with tryptophan proving to be the most hydrophobic and glutamic acid being the most hydrophilic.[77]

Generally, the transition temperature is decreased as the water of hydrophobic hydration increases. If an ELP is longer or if there is a larger concentration of ELP, then more ordered water molecules will surround the hydrophobic residues simply by virtue of there being more residues to hydrate. The effect on T_t comes when the ordered water is transferred to the bulk fluid by heating. When more ordered water is transferred to the bulk water then the greater the change of entropy and the lower the transition temperature, as evident by $T_t = \Delta H_t/\Delta S_t$ ($\Delta G_t=0$).[74] As an example of the dependence of transition temperature on pentamer number, an ELP of sequence $(VPGVG)_n$ with n=25 will have a $T_t \approx 50°C$ while another ELP of the same sequence with an n=90 will have a $T_t \approx 30°C$.[78] Similar examples can be given for the other parameters mentioned earlier. It is important to note that effects seen by concentration and chain length are mutually exclusive in that their effects are unique and different transition temperatures will be observed even when the solution concentrations are equal on the basis of gravimetric measurements.[79]

Similar to CLPs, ELPs were initially developed to gain a better understanding of the elastic properties of elastin on a molecular level. It had been understood for some time via mechanical experimentation that elastin's elastomeric force was entropically dominated.[75] Yet details into why this was the case on a molecular level drove studies towards characterization of synthetic polymeric ELPs.[75] The research in this endeavor was led by Dan Urry and coworkers and through decades of work, an ordered (non-random) librational entropy mechanism was proposed to explain the elastic processes in proteins such as elastin.[74,75]

Through the works of Urry and others, various methodologies have been employed to characterize the transition temperature and its resulting properties. Such techniques include electron microscopy, circular dichroism, temperature modulated differential scanning calorimetry, light scattering, dielectric relaxation, and nuclear magnetic resonance spectroscopy studies that utilize relaxation and the nuclear overhauser effect.[80,81]

Circular dichroism in particular has been used to confirm the β-turn structure upon folding. The CD spectra of β-turns is known to be difficult to study given the wide array of conformations that the different types of β-turns possess.[76] Furthermore, the magnitude of β-turn CD bands is considerably weaker in comparison to the more periodic secondary structures such as β-sheets, α-helices, and triple helices.[76] Despite these difficulties, CD has been used to study ELPs for some time and has often demonstrated the type II β-turn structure.[75,80] The characteristics of type II β-turns is a weak negative band in the 220-230nm region, a stronger positive band in the 200-210nm/206-212nm region, and a strong negative band between 180-195nm.[76,82] It should be noted however, that even small perturbations to the primary sequence of short ELPs (n<4) have demonstrated equimolar mixtures of random coils and β-turns as well as type I and III β-turns.[82] Moreover, CD spectra of different ELP systems have had significantly different interpretations over the years, as highlighted by Daggett *et al*.[83] Nonetheless, the plethora of data from CD, NMR, and other techniques have established the β-turns as the most accepted structure in ELPs.

While in the past the use of ELPs was predominantly to gain a fundamental understanding of elastomeric proteins, recent years have seen a significant increase in the application of ELPs. Specifically the use of ELPs as a means for recombinant

protein expression purification and as novel drug delivery vehicles have been widely developed in the past two decades.

Through protein synthesis techniques such as recursive directional ligation, specific and predetermined ELP sequences can be easily made.[78] More importantly however, ELPs have been incorporated as fusion proteins as a means for a simple protein purification strategy.[84] This purification makes use of the inverse transition temperature of the ELP which acts as a means to change the physical state of the ELP-protein construct. In practice, the protein cell lysate undergoes a series of heating, centrifugation, cooling, and centrifugation steps (in that order) to first collapse and aggregate the ELP and the protein of interest, collect the aggregates via centrifugation, and cool and centrifuge to isolate and remove insoluble impurities.[85] Depending on the application and the protein carrier, high concentrations of salt can also be added to induce the transition temperature mechanism.[85]

Another significant application for ELPs is their use as carriers for targeted drug delivery.[78] The inverse phase transition process of ELP is completely reversible, making it an ideal candidate for many material and biomedical science applications.[74,78,85] Specifically, the inverse phase transition process can be exploited for the controlled release of drug carrier. The type of ELP drug delivery vehicles range from the simple conjugation of drugs to the N-terminal ELPs in the collapsed state, to 'chimeric' ELP nanoparticles.[78,86] These studies have shown fair success in their endeavors, yet a large variety of possible ELP sequences can yield a diverse population of nanoparticle systems with their own discrete differences with regard to size and morphology. Therefore, it is perhaps advantageous to use ELPs as one component of a multicomponent system rather than relying on ELPs as the entire base

material for nanoparticle systems. The following section discusses the inclusion of ELPs as one half of a nanoparticle system that may show promise for ECM drug delivery.

1.5 The Elastin-like-*block*-Collagen-like Peptide Nanoparticle and its Properties

Recently, the Kiick research group has focused on the development of *de novo* nanoparticles that are comprised of CLPs tethered to LCST domains. An LCST domain of poly(diethylene glycol methyl ether methacrylate) has been previously demonstrated, but more recently a short synthetic ELP was also developed.[87,88] The goal of tying CLPs with LCST domains to make a particle that is capable of hybridizing to denatured collagen protein via the CLP domain and also to exploit the thermoresponsive properties of the LCST domain for on-demand drug delivery.

Similar to rod-coil block copolymer self-assembly systems, it was found that an ELP-CLP conjugate can readily self-assemble into closed bilayers that result in vesicular nanoparticles. The process of the self-assembly begins with a single stranded ELP-CLP conjugate monomer that exists as an extended random coil at high temperatures (≈80°C) due to CLP triple helix being in a melted state and the ELP's transition temperature being greater than 80°C. Upon cooling below the CLP triple helical melting temperature, the triple helix begins to form and subsequently three ELP chains are brought together. There are a couple of ideas regarding the mechanism that comes next (discussed below), but in either case the ELP undergoes a phase transition and collapses to its β-turn/β-spiral structure. In this collapsed state, the CLP triple helix can be viewed as a long hardened rod and the ELP can be thought of as an ordered coil. Furthermore, the ELP is significantly more hydrophobic than the CLP and begins to associate with itself; perhaps to some degree in the same manner as

depicted in Figure 1.4 with β-spiral-β-spiral intercalation. This association eventually results in a bilayer formation with a hydrophobic ELP inner core and hydrophilic interior and exterior. The entire assembly process is illustrated in Figure 1.5 below.

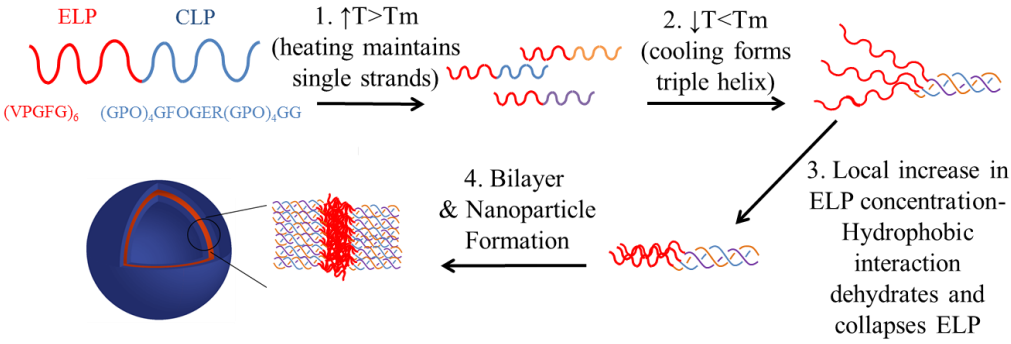

Figure 1.5: Self-assembly process of the ELP-CLP peptide nanoparticle. Nanoparticle image is adapted from Luo, T. Z.; Kiick, K. L., Noncovalent Modulation of the Inverse Temperature Transition and Self-Assembly of Elastin-b-Collagen-like Peptide Bioconjugates. Journal of the American Chemical Society 2015, 137 (49), 15362-15365. Copyright 2017 American Chemical Society.

The ELP collapse is reasoned to be occurring due to the packing considerations of the observed bilayer as well as the thermal characteristics of the resulting particles (discussed below). The exact mechanism of the ELP collapse can be described from two viewpoints that are common to transition temperature analyses. In one viewpoint, the three ELP chains are connected to each other by non-covalent means and behave in a similar fashion to $(VPGX_{AA}G)_{n*3}$. As an example, a single ELP chain of $(VPGX_{AA}G)_6$ would behave as $(VPGX_{AA}G)_{18}$ after triple helix formation, and as a result the T_t would lower and collapse. This viewpoint however, likely does not fit

well with the CLP triple helix formation mechanism as three chains packed laterally together is significantly different in terms of their interactions with both the solvent and each other, then one long ELP chain. The second viewpoint is that the local concentration of the ELP has increased and also as a result the transition temperature has decreased. It was previously reported that the ELP concentration in the trimerized state is 100 fold higher than ELP monomer in a non-trimerized bulk state.[88] However, it may not be appropriate to assign these conventional transition temperature trends to the ELP-CLP conjugate system. When the concentration of free ELP is doubled, the number of water molecules in a low entropy state surrounding the hydrophobic residues also increases in some proportion. Thus when the water molecules of the doubled concentration transfer to the bulk, there is a greater increase in the change of entropy between the two states and the transition temperature is lowered in comparison to the non-doubled ELP concentration system because $T_t = \Delta H_t/\Delta S_t$ ($\Delta G_t=0$).

In the case of the ELP-CLP conjugate in the extended solubilized state, the number of water molecules of hydrophobic hydration is finite even during triple helix formation. In other words, the number of water molecules in the low entropy state surrounding the hydrophobic residues does not change simply because of increased local concentration effect *per se*. I suggest rather, that the increase in order of the ELP chains imparted by the CLP chains is responsible for the decreased order of waters of hydrophobic hydration. In effect, the increase in the change of entropy of the bulk water comes from the change of entropy of the chains from an unordered to an ordered state upon triple helix formation. Furthermore, just as with the non-conjugated ELP chains, the extreme close proximity of the ELP chains elicits a favorable hydrophobic

interaction between the chains that in turn stabilize the transition. The tight packing of the triple helix has a spacing between chains that is at its shortest, on the order of the length of a hydrogen bond (≈2.5 Å).[40] It may then be assumed that similar chain spacing is imparted to the ELP chains. The combined effect of the dehydration followed by favorable hydrophobic interactions in turn instigates hydrophobic folding and collapse of the ELP chains to their β-turn/β-spiral structure. Further considerations of this mechanism will be discussed in Chapter 3.

The ELP sequence used in the pioneering report of the ECM derived nanoparticle was a short sequence of $(VPGFG)_6$. This short sequence has a T_t greater than 80°C, and without any additives, does not go through a phase transition.[88] This ELP sequence was conjugated to the CLP sequence $(GPO)_4GFOGER(GPO)_4GG$, which by itself has a T_m=50°C according to circular dichroism studies. This sequence also contains the integrin binding sequence GFOGER that was initially intended for possible cell adhesion and uptake. However, GFOGERs importance primarily lies in the observed melting temperature rather than its bioactivity properties. This is because the GFOGER residues are buried within the nanoparticle corona and are not accessible in a linear format for $\alpha_2\beta_1$ or $\alpha_1\beta_1$ interaction, as would be naturally found and as was observed via x-ray crystallography studies.[12]

1.5.1 Analysis of particle dependence on temperature by dynamic light scattering

As has already been discussed, the central mechanism of the nanoparticle assembly is the CLP triple helical folding followed by a rapid change of the inverse transition temperature. Due to the packing required for ELP in the inner bilayer, it is reasoned that the transition temperature of the ELP changed from greater than 80°C in

the monomeric state to less than 4°C in the collapsed trimerized state. The 4°C value comes from the fact that the particle is stable at temperatures down to 4°C and so it is reasoned that the transition temperature is less than 4°C, since if the T_t was higher, then a lower temperature would extend the ELP domain and presumably solubilize the particle. Furthermore, the melting temperature of CLP was found to be increased to 57°C (according to circular dichroism), presumably by a hydrophobic stabilization effect imparted by the ELP chains. Table 1.1 summarizes the transition temperature (T_t) and melting temperature (T_m) characteristics of ELP and CLP respectively as well as that of the ELP-CLP conjugate.[88]

Table 1.1: Summary of peptide and particle thermal characteristics and their meaning.

Domain	**T_t**	**T_m**	**Meaning**
CLP	N/A	50°C	Above $T_{m,}$ triple helical unfolding occurs
ELP	> 80°C	N/A	Non-collapsed state; soluble in water
ELP-CLP Conjugate	< 4°C	57°C	Collapsed state; nanoparticle formed; triple helical unfolding begins at T_m

While these parameters are useful for understanding the properties of the ELP-CLP conjugate/particles on a general level, seeing how temperature affects particle size directly is also important. Using dynamic light scattering the ELP-CLP particle size was analyzed as a function of temperature. In this particular study the particles were dispersed in 10 mM phosphate buffered saline (PBS) to approximate *in vitro* cell culture conditions. As stated earlier, the particles were found to be very stable and maintain a consistent size between 4°C and 54°C, indicating that the transition temperature of ELP has changed from being greater that 80°C to being less than 4°C. Once the temperature reaches the 57°C triple helical melting temperature observed by

circular dichroism, the particles CLP exterior begin to unfold and loosen and the particle size dips to a small degree. It is in this region, between 57°C and about 65°C, that ELP-CLP particle may begin to have the ability to hybridize to denatured collagen protein since the particle appears to remain intact, yet triple helical unfolding is occurring according to circular dichroism and the reduced particle size. Heating the particle above 65°C, the particle size apparently increases likely due to decreased diffusion coefficient caused by an increase of particle drag due to the CLP strands being at their most extended/non wound state. This particle size increase does not last for long, however, because at 70°C the particle completely dissociates due to the triple helical strands being completely unfolded and as a result the particle becomes destabilized. It is also likely that the ELP strands denucleate and rehydrate during this process as well. The dynamic light scattering data along with bilayer and conjugate illustrations throughout the heating process is shown in Figure 1.6 below.

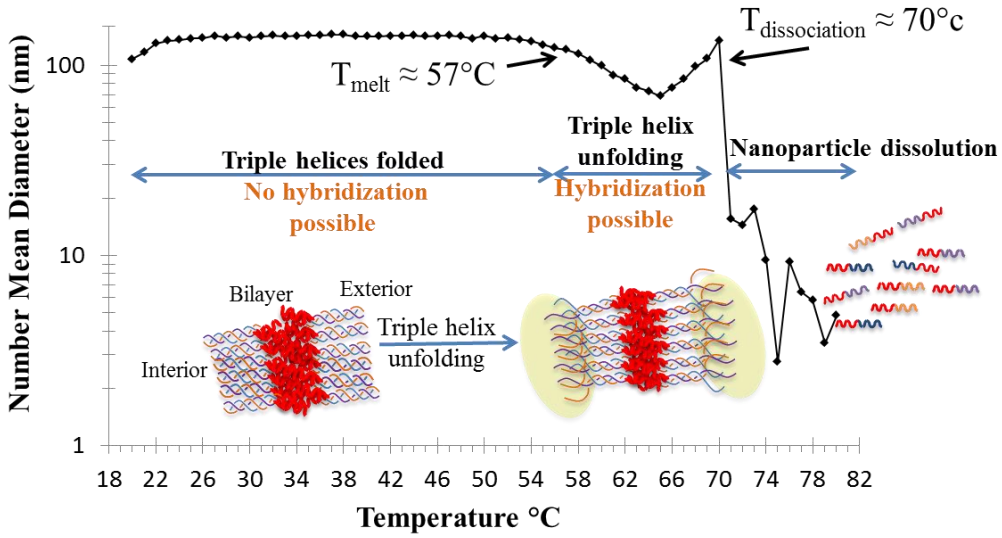

Figure 1.6: Dynamic light scattering of ELP-CLP particles in 10mM PBS; number mean diameter particle size as a function of temperature. Illustrations of the bilayer are shown for stable particles below 57 °C, melted helices between 57 °C and 69 °C, and particle dissociation at 70 °C.

1.5.2 Cell viability and uptake of ELP-CLP nanoparticles

Prior to implementation of particles into *in vivo* systems for drug delivery studies, they must first be evaluated for their delivery and cell viability properties *in vitro*. The viability aspect is especially important for ELP-CLP particles that are synthesized using copper click chemistry as copper has known cytotoxic effects. Furthermore, it is of considerable interest to determine if cells can internalize these particles as this would be of some interest with regard to future use of these particles for drug delivery. The following sections discuss results of cell viability and uptake experiments with the $(VPGFG)_6$-$(GPO)_4GFOGER(GPO)_4GG$ ELP-CLP nanoparticle system.

1.5.2.1 NIH-3T3 fibroblast cell viability results

It is envisioned that ELP-CLP particles can be used to treat ECM related diseases due to the CLPs potential for hybridization with degraded collagen matrices found in these diseases. Because fibroblasts are known ECM modulators having roles as both a maker of collagen and as a secretor of MMPs, the assessment of their viability with ELP-CLP nanoparticles is relevant with regard to future applications. Such applications include the use of these particles in collagen type II degraded joints found in rheumatoid and osteoarthritis or in the heterogeneous degraded ECM associated with tumor microenvironments.

The results of the viability study are shown in Figure 1.7 below, which was reproduced with permission from Luo, T.; David, M.; Dunshee, L.; Scott, R.; Urello, M; Price, C; Kiick, K., Thermoresponsive elastin-*b*-collagen-like peptide bioconjugate nanovesicles for targeted drug delivery to collagen-containing matrices. *Biomacromolecules*. 2017, 18(8), 2539-2551.[89] The procedures for this study are detailed in section 2.4.1. The calcein AM stain is known as a live stain because the dye is only functional in metabolically active cells. The propidium iodide is a red fluorescent dye that intercalates with the nuclear DNA of membrane compromised cells which is typically indicative of dead cells.

From Figure 1.7, both the untreated cells as well as the 1000 μg/mL nanoparticle treated cells (top and bottom rows respectively) only show the presence of the live stain with little to no trace of the dead stain. Furthermore, the cell spreading of the fibroblasts, as evidenced by the phase images, is indicative of healthy cells. Similar viability is shown for lower nanoparticle concentrations in reference 89. The viability may also be an indicator that Cu removal post conjugate synthesis was in large part successful. In contrast, the cells treated with Cu(I) acetate were readily

killed most likely due to Cu ion cytotoxicity. This is evident by the majority of cells being removed by the DPBS washing step, as indicated by the low cell count in the middle row phase image, and what cells do remain only show the propidium iodide stain indicative of dead cells.

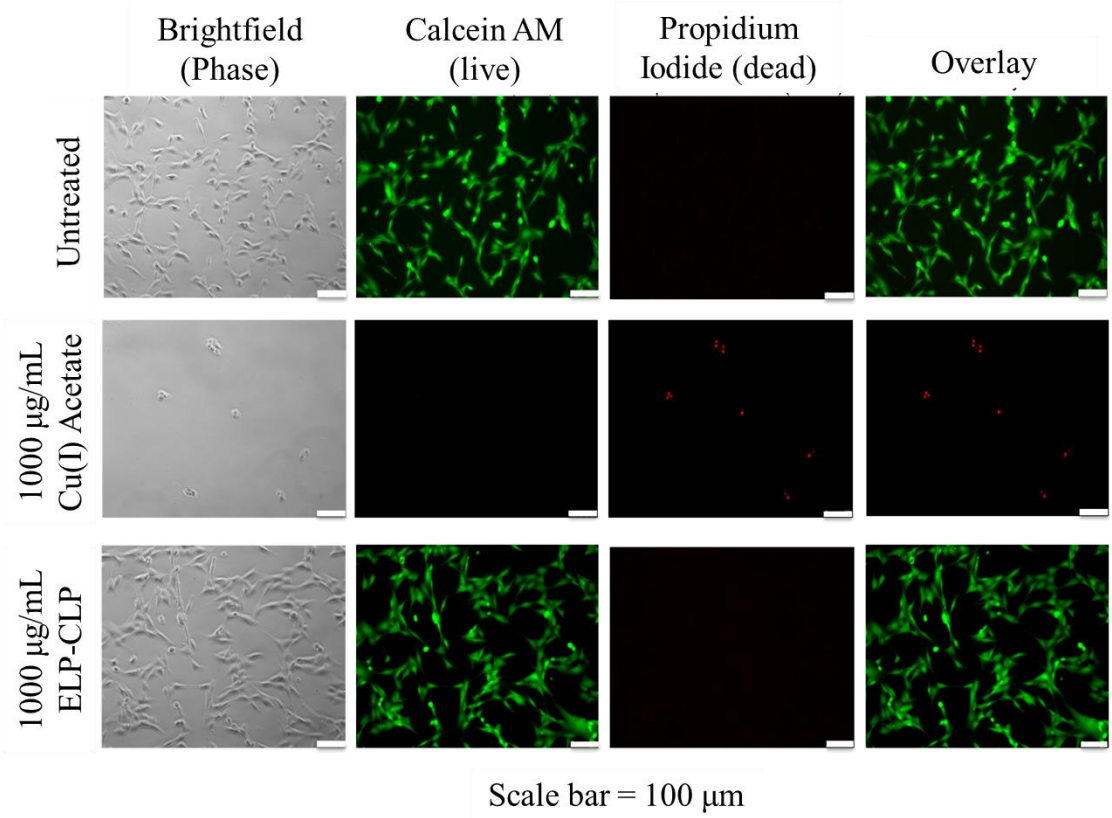

Figure 1.7: Cell viability results after 24 hour incubation of NIH-3T3 fibroblasts with no treatment, 1mg/mL Cu(I) acetate, and 1mg/mL ELP-CLP nanoparticles. All images were taken with a 10x objective. The overlay column is a merge of the calcien AM and propidium iodide images. Adapted with permission from Luo, T. Z.; David, M. A.; Dunshee, L. C.; Scott, R. A.; Urello, M. A.; Price, C.; Kiick, K. L., Thermoresponsive Elastin-b-Collagen-Like Peptide Bioconjugate Nanovesicles for Targeted Drug Delivery to Collagen-Containing Matrices. Biomacromolecules 2017, 18 (8), 2539-2551. Copyright 2017 American Chemical Society.

The healthy viability of the fibroblasts cells with these ELP-CLP nanoparticles is in good accord with literature regarding cell viability with other peptide nanoparticle systems. Such other cases in the literature that have demonstrated the biocompatibility of peptide nanoparticles with fibroblasts include metal coordinated dipeptide particles as well as ELP formulated nanoparticles.[89]

1.5.2.2 NIH-3T3 cell uptake of fluorescent ELP-CLP nanoparticles

Given that these cells are viable when incubated with ELP-CLP particles, it was desired to investigate whether the cells are internalizing the nanoparticles, as this would be important for future drug delivery studies. In order to visualize the nanoparticles, an ELP was made that was functionalized with 5-(6)-carboxyfluorescein ((λ_{ex}/ λ_{ex}) ≈ 492/517nm) on the N-terminus, which would allow for easy detection by fluorescence microscopy or flow cytometry. The procedure used for cellular internalization is highlighted in section 2.4.2. The next two sections highlight the results of fluorescent elastin-*block*-collagen like (FELP-CLP) peptide nanoparticle uptake into fibroblasts.

1.5.2.2.1 Fluorescence microscopy

The results of the fluorescence microscopy imaging of internalized uptaken nanoparticles in NIH-3T3 fibroblasts is shown in Figure 1.8 below. The images represented in Figure 1.8 are identical but were taken at the 20x (left) and 40x (right) objective magnifications respectively. In these images, the Hoechst stain is shown in blue and successfully functioned to highlight the nucleus. Staining the nucleus allows the identification of cell location without staining the entirety of the cell which could perhaps prevent the identification of uptaken fluorescent nanoparticles. From the

images it is evident that fluorescent nanoparticles (green) have the appearance of being within the cell cystol. The cytosol of the cell is distinguishable from the background by having a faint blue hue from leftover non-nuclear bound Hoechst stain. Given the proximity of the nanoparticles to the cell nucleus as well as the location of the particles being within the blue hue of the dim cytosol, it is likely that the particles were indeed internalized into the cells during the four hour incubation period and remained internalized during the 16 hour recovery period as well. Furthermore, it is also likely that the particles were internalized by some endosomal pathway given the large clusters of fluorescence that are detected next to the cell.

Individual particles cannot be detected with standard fluorescence microscopy, so instead it is likely that the images are indicative of particles that are trapped in endosomes. The internalization mechanism and retention time of the particles is subject to future study. However, with regard to the internalization mechanism, I hypothesize that a clathrin-mediated pathway is likely based on the similarity of the size of these particles (≈160nm) and the reported size requirement of the clathrin endosomal pathway (≈120nm).[90] In this study, the total time for nanoparticle and cell interactions to take place is less than 24 hours. It is very likely that in the hours after this time period that the particles will be readily exocytosed. Future studies will have to assess retention over the course of many days to determine the fate of delivered nanoparticles.

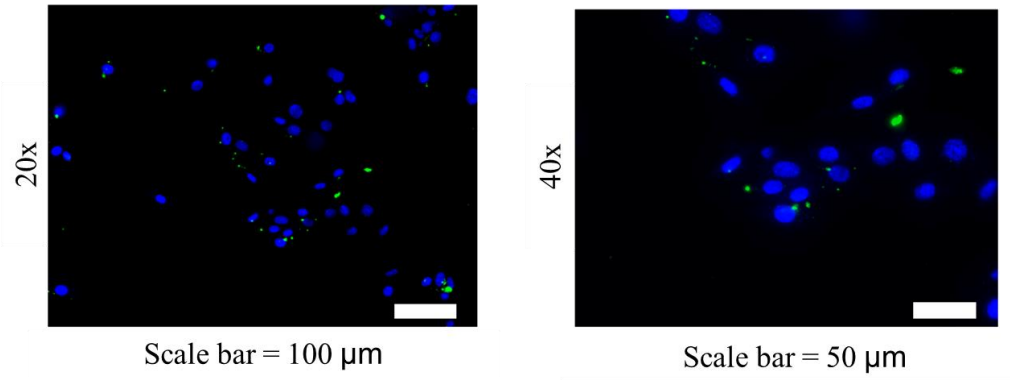

Figure 1.8: FELP-CLP uptake into NIH-3T3 fibroblast cells after 4 hours of serum starved incubation and a 16 hour recovery. The images are identical with the left image being at a 20x objective magnification and the right image being at a 40x objective magnification. Hoechst 33258 nuclear stain is shown in blue and FELP-CLP nanoparticle clusters are shown in green.

1.5.2.2.2 Flow cytometry

Despite the qualitative success of the cellular uptake of the FELP-CLP nanoparticles as shown in Figure 1.8, a more quantitative assessment is desired to verify the results. Furthermore, there is also the possibility that the particles in Figure 1.8 are not necessarily internalized, but could be residing on top of the cell instead. If this were the case then the particles would have the appearance of being within the cytosol even though they are not.

Flow cytometry is a technique in which non-adhered cells are sent as a stream of fluid to multiple optical systems that detect the forward and back scattering of cellular particles as well as any fluorescent moieties that the cell may possess. Using this technique the number of cells that contain internalized fluorescent nanoparticles can be precisely detected. The procedure used for flow cytometry is shown in section 2.4.3.

Two distinct populations of cells were analyzed, one set of cells that were not treated with nanoparticles and another set of cells that were. The cells that were not treated can still be detected by fluorescence spectroscopy in the (λ_{ex}/ λ_{ex}) ≈ 492/517nm region due to the autofluorescence found naturally in the cells from compounds such as NADPH, flavins, and aromatic amino acids such as tyrosine, tryptophan, and phenylalanine.[91] However, the intensity of this autofluorescence should be dramatically lower than cells that are treated with fluorescent nanoparticles. The data collected for these two tested cell populations is shown in Figure 1.9 below.

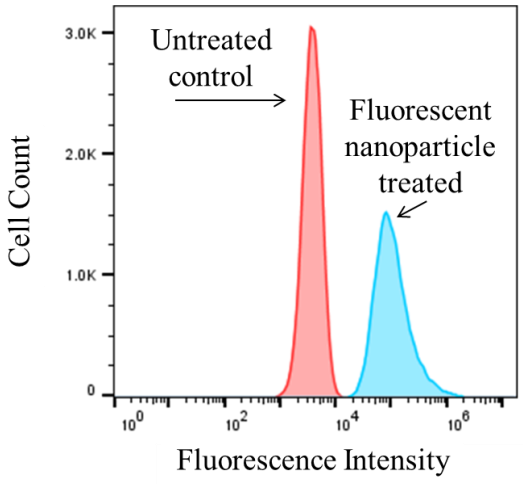

Figure 1.9: Flow cytometry analysis of untreated cells (red) and FELP-CLP treated cells (blue). The untreated fluorescence intensity is due to autofluorescence while uptaken nanoparticles are likely responsible for the increased fluorescence of the nanoparticle treated population.

The frequency curves in Figure 1.9 illustrate the significant difference in fluorescence intensity of the FELP-CLP treated cells and the untreated cells. From the curves it is easily seen that nearly all of the fluorescent nanoparticle treated cells have

a fluorescence intensity that is greater than the autofluorescence intensity of untreated cells. This fluorescence intensity increase of the nanoparticle treated cells ranges from nearly 2 to 100 times greater than the maximal fluorescence intensity seen in the untreated cell population. Furthermore, the average fluorescence intensity of the FELP-CLP nanoparticles is approximately 12.5 times greater than the average fluorescence intensity of the untreated cell population. These results corroborate the fluorescence microscopy data and suggest that nanoparticles were successfully internalized into the fibroblast cells within the 4 hour incubation and 16 hour recovery period. Similar to the microscopy data, future work should determine how long particles are retained in the cells by analyzing the fluorescence intensity difference between the treated and untreated cells decreases over time, since nanoparticles may be exocytosed.

1.5.2.3 Summary of cell viability for other cell lines

The cell interactions of ELP-CLP nanoparticles with other cell lines were studied by Luo, T.; David, M.; Dunshee, L.; Scott, R.; Urello, M; Price, C; Kiick, K.[89] In particular the cell viability and proliferation of ATDC chondrocyte cells was studied for an array of concentrations over the course of 72 hours. It was found that the percentage of live chondrocyte cells never reached below 90% for concentrations ranging from 0, 50, 150, 500, and 1000μg/mL for both the 24 and 72 hour time points. Furthermore, cell proliferation of these cells was not hindered in comparison to untreated cells over the course of the three day study. The findings are important as chondrocytes play a key role in matrix maintenance (collagen and proteoglycans) in cartilage.

To further understand ELP-CLP nanoparticle biocompatibility, the inflammatory potential and cell viability of Raw 264.7 macrophage-like cells was also analyzed in the study.[89] It was found that after eight hours of incubation, relative to lipopolysaccharide induced stimulation, 1000μg/mL ELP-CLP nanoparticles did not elicit the production of significant amounts of the inflammatory cytokine TNF-α, which is responsible for downstream MMP production and ECM degradation. This is important as it shows that the nanoparticles themselves do not further induce an inflammatory state that they may eventually be used to treat. Moreover, the ELP-CLP nanoparticle did not alter macrophage metabolic activity over time which gave some indication that the particles were not toxic to the cells. These studies firmly illustrate the biocompatibility of the ELP-CLP particles and pave the way for their future drug delivery application *in vitro* and *in vivo*.

1.5.3 Modification of the ELP-CLP nanoparticle for improved drug delivery properties

The biocompatibility of these particles *in vitro*, show the promise of their future application. However, it is clearly seen in Table 1.1 and Figure 1.6 that the current ELP-CLP nanoparticle (sequences $(VPGFGP)_6$-$(GPO)_4GFOGER(GPO)_4GG$) respectively) does not yet possess any useful attributes that we desire for its application in drug delivery. Specifically the ELP domain does not possess an observable lower critical solution temperature that can be used for rapid particle dissolution and on-demand drug release. In a similar fashion the CLP domain does not have a physiologically relevant hybridization region that can be exploited for CLP targeting/hybridization with denatured collagen protein in the body (see Figure 1.6). The particles would have to be heated to excessively high temperatures and maintain

those temperatures (≈65°C) within the body for hybridization to occur. The specific drug delivery applications that are sought for these particles are illustrated in Figure 1.10 below.

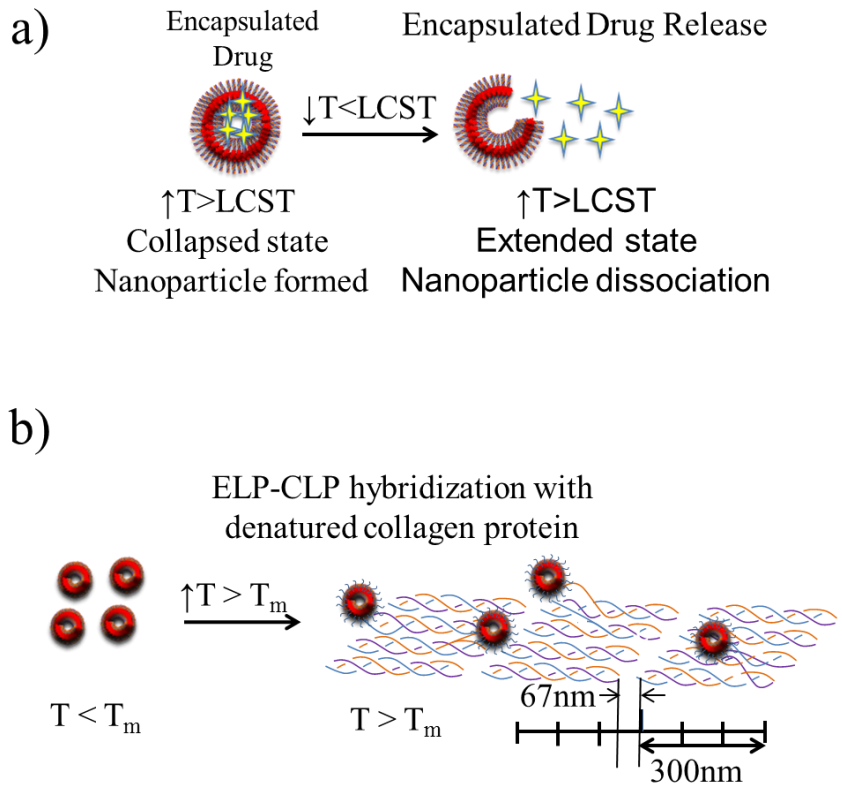

Figure 1.10: Desired properties for the ELP-CLP nanoparticle. a) An ELP domain that possesses a LCST that can be used for on-demand drug delivery by decreasing the system below the T_t. b) A CLP domain that can hybridize to denature collagen protein at physiologically relevant temperatures (particles, band gap, and collagen protein molecules are to scale).

In order to achieve these properties for the ELP-CLP nanoparticle system, the T_t and T_m of the ELP and CLP domains respectively will have to be fine-tuned

through alterations to either the volume fraction of each domain or the primary sequence. The design of peptides will be discussed in Chapter 3, but desired temperature regions for each domain can be briefly discussed.

Since the physiological temperature of humans is 37°C, the particle cannot have an upper dissociation temperature that is below this value. More specifically the complete dissociation temperature should be 45°C or greater so as to ensure that the particle remains intact during the hybridization process. The desired hybridization region should be within the physiological temperature (34°C to 43°C) so that the triple helix of the particle can be in a partially unfolded state for collagen protein hybridization.

The transition temperature mechanism is a rapid process that takes place over a narrow temperature region (within a 5°C). However, there is a limit to how far the human body can be cooled without adversely affecting the patient. However, at least one study has shown that the deep tissue of the human body can be successfully cooled to 25°C without any significant damage or side-effects to the patient.[92] With this in mind, the ideal transition temperature region should be between 25°C and 30°C so that drug release can be carried out efficiently without significant adverse effects from the hypothermic treatment. A summary of these idealized temperature parameters is presented in Table 1.2 below.

Table 1.2: Desired thermal hybridization and dissociation regions for drug delivery.

	Lower dissociation region (LCST)	Hybridization region	Upper dissociation region (triple helical melt)
Initial nanoparticle system	< 4°C	57°C - 70°C	> 70°C
Desired nanoparticle system	25°C - 30°C	34°C - 45°C	> 45°C

REFERENCES

1. Bonnans, C.; Chou, J.; Werb, Z., Remodelling the extracellular matrix in development and disease. Nature Reviews Molecular Cell Biology. 2014, 15(12), 786-801.

2. Lu, P. F.; Takai, K.; Weaver, V. M.; Werb, Z., Extracellular Matrix Degradation and Remodeling in Development and Disease. Cold Spring Harbor Perspectives in Biology. 2011, 3 (12), 1-24.

3. Theocharis, A. D.; Skandalis, S. S.; Gialeli, C.; Karamanos, N. K., Extracellular matrix structure. Advanced Drug Delivery Reviews 2016, 97, 4-27.

4. Wight, T. N.; Potter-Perigo, S., The extracellular matrix: an active or passive player in fibrosis? American Journal of Physiology-Gastrointestinal and Liver Physiology 2011, 301 (6), G950-G955.

5. Rozario, T.; DeSimone, D. W., The extracellular matrix in development and morphogenesis: A dynamic view. Developmental Biology 2010, 341 (1), 126-140.

6. Kucharz, E.J., *The collagens: Biochemistry and pathophysiology*; Springer-Verlag: Berlin Heidelberg, 1992.

7. Harisi, R.; Jeney, A., Extracellular matrix as target for antitumor therapy. Oncotargets and Therapy 2015, 8, 1387-1398.

8. Allen, T. M.; Cullis, P. R., Drug delivery systems: Entering the mainstream. Science 2004, 303 (5665), 1818-1822.

9. Smirnov, V. N.; Domogatsky, S. P.; Dolgov, V. V.; Hvatov, V. B.; Klibanov, A. L.; Koteliansky, V. E.; Muzykantov, V. R.; Repin, V. S.; Samokhin, G. P.; Shekhonin, B. V.; Smirnov, M. D.; Sviridov, D. D.; Torchilin, V. P.; Chazov, E. I., CARRIER-DIRECTED TARGETING OF LIPOSOMES AND ERYTHROCYTES TO DENUDED AREAS OF VESSEL WALL. Proceedings of the National Academy of Sciences of the United States of America 1986, 83 (17), 6603-6607.

10. An, B.; Lin, Y. S.; Brodsky, B., Collagen interactions: Drug design and delivery. Advanced Drug Delivery Reviews 2016, 97, 69-84.

11. Gelse, K.; Poschl, E.; Aigner, T., Collagens - structure, function, and biosynthesis. Advanced Drug Delivery Reviews 2003, 55 (12), 1531-1546.

12. Shoulders, M. D.; Raines, R. T., Collagen Structure and Stability. In Annual Review of Biochemistry, Annual Reviews: Palo Alto, 2009; Vol. 78, pp 929-958.

13. Persikov, A. V.; Xu, Y. J.; Brodsky, B., Equilibrium thermal transitions of collagen model peptides. Protein Science 2004, 13 (4), 893-902.

14. Kakinoki, S.; Hirano, Y.; Oka, M., On the stability of polyproline-I and II structures of proline oligopeptides. Polymer Bulletin 2005, 53 (2), 109-115.

15. Persikov, A. V.; Ramshaw, J. A. M.; Brodsky, B., Collagen model peptides: Sequence dependence of triple-helix stability. Biopolymers 2000, 55 (6), 436-450.

16. Gadalla, S.M.; Widemann, B.C., Editorial: US cancer statistics of survival: achievements, challenges, and future directions. Journal of the National Cancer Institute 2017, 109(9).

17. Danhier, F.; Feron, O.; Preat, V., To exploit the tumor microenvironment: Passive and active tumor targeting of nanocarriers for anti-cancer drug delivery. Journal of Controlled Release 2010, 148 (2), 135-146.

18. Seo, B. R.; DelNero, P.; Fischbach, C., In vitro models of tumor vessels and matrix: Engineering approaches to investigate transport limitations and drug delivery in cancer. Advanced Drug Delivery Reviews 2014, 69, 205-216.

19. Egeblad, M.; Rasch, M. G.; Weaver, V. M., Dynamic interplay between the collagen scaffold and tumor evolution. Current Opinion in Cell Biology 2010, 22 (5), 697-706.

20. Gialeli, C.; Theocharis, A. D.; Karamanos, N. K., Roles of matrix metalloproteinases in cancer progression and their pharmacological targeting. Febs Journal 2011, 278 (1), 16-27.

21. Kessenbrock, K.; Plaks, V.; Werb, Z., Matrix Metalloproteinases: Regulators of the Tumor Microenvironment. Cell 2010, 141 (1), 52-67.

22. Visse, R.; Nagase, H., Matrix metalloproteinases and tissue inhibitors of metalloproteinases - Structure, function, and biochemistry. Circulation Research 2003, 92 (8), 827-839.

23. Rao, J. S., Molecular mechanisms of glioma invasiveness: The role of proteases. Nature Reviews Cancer 2003, 3 (7), 489-501.

24. Myllyharju, J.; Kivirikko, K. I., Collagens and collagen-related diseases. Annals of Medicine 2001, 33 (1), 7-21.

25. Järveläinen, H.; Sainio, A.; Koulu, M.; Wight, T. N.; Penttinen, R., Extracellular Matrix Molecules: Potential Targets in Pharmacotherapy. Pharmacological Reviews 2009, 61 (2), 198-223.

26. Brodsky, B.; Persikov, A. V., Molecular structure of the collagen triple helix. Fibrous Proteins: Coiled-Coils, Collagen and Elastomers 2005, 70, 301-339.

27. Persikov, A. V.; Ramshaw, J. A. M.; Kirkpatrick, A.; Brodsky, B., Amino acid propensities for the collagen triple-helix. Biochemistry 2000, 39 (48), 14960-14967.

28. Richards, A. J.; Martin, S.; Nicholls, A. C.; Harrison, J. B.; Pope, F. M.; Burrows, N. P., A single base mutation in COL5A2 causes Ehlers-Danlos syndrome type II. Journal of Medical Genetics 1998, 35 (10), 846-848

29. Nagase, H.; Visse, R.; Murphy, G., Structure and function of matrix metalloproteinases and TIMPs. Cardiovascular Research 2006, 69 (3), 562-573.

30. Akhavani, M. A.; Madden, L.; Buysschaert, I.; Sivakumar, B.; Kang, N.; Paleolog, E. M., Hypoxia upregulates angiogenesis and synovial cell migration in rheumatoid arthritis. Arthritis Research & Therapy 2009, 11 (3), 11.

31. Gibson, M.; Li, H. W.; Coburn, J.; Moroni, L.; Nahas, Z.; Bingham, C.; Yarema, K.; Elisseeff, J., Intra-Articular Delivery of Glucosamine for Treatment of Experimental Osteoarthritis Created by a Medial Meniscectomy in a Rat Model. Journal of Orthopaedic Research 2014, 32 (2), 302-309.

32. Vasanthi, P.; Nalini, G.; Rajasekhar, G., Role of tumor necrosis factor-alpha in rheumatoid arthritis: a review. APLAR Journal of Rheumatology 2007, 10, 270-274.

33. Majka, S.; McGuire, P. G.; Das, A., Regulation of matrix metalloproteinase expression by tumor necrosis factor in a murine model of retinal neovascularization. Investigative Ophthalmology & Visual Science 2002, 43 (1), 260-266.

34. Singh, J. A.; Wells, G. A.; Christensen, R.; Ghogomu, E. T.; Maxwell, L.; MacDonald, J. K.; Filippini, G.; Skoetz, N.; Francis, D.; Lopes, L. C.; Guyatt, G. H.; Schmitt, J.; La Mantia, L.; Weberschock, T.; Roos, J. F.; Siebert, H.; Hershan, S.; Lunn, M. P. T.; Tugwell, P.; Buchbinder, R., Adverse effects of biologics: a network meta-analysis and Cochrane overview. Cochrane Database of Systematic Reviews 2011, (2), 60.

35. Hu, K.; Xu, L.; Cao, L.; Flahiff, C. M.; Brussiau, J.; Ho, K.; Setton, L. A.; Youn, I.; Guilak, F.; Olsen, B. R.; Li, Y., Pathogenesis of osteoarthritis-like changes in the joints of mice deficient in type IX collagen. Arthritis and Rheumatism 2006, 54 (9), 2891-2900.

36. Sandell, L. J.; Aigner, T., Articular cartilage and changes in arthritis - An introduction: Cell biology of osteoarthritis. Arthritis Research 2001, 3 (2), 107-113.

37. Wahyudi, H.; Reynolds, A. A.; Li, Y.; Owen, S. C.; Yu, S. M., Targeting collagen for diagnostic imaging and therapeutic delivery. Journal of Controlled Release 2016, 240, 323-331.

38. Luo, T. Z.; Kiick, K. L., Collagen-like peptides and peptide-polymer conjugates in the design of assembled materials. European Polymer Journal 2013, 49 (10), 2998-3009.

39. Li, Y.; Mo, X. A.; Kim, D.; Yu, S. M., Template-Tethered Collagen Mimetic Peptides for Studying Heterotrimeric Triple-Helical Interactions. Biopolymers 2011, 95 (2), 94-104.

40. Brodsky, B.; Ramshaw, J. A. M., The collagen triple-helix structure. Matrix Biology 1997, 15 (8-9), 545-554.

41. Bella, J.; Eaton, M.; Brodsky, B.; Berman, H. M., CRYSTAL-STRUCTURE AND MOLECULAR-STRUCTURE OF A COLLAGEN-LIKE PEPTIDE AT 1.9-ANGSTROM RESOLUTION. Science 1994, 266 (5182), 75-81.

42. Bella, J.; Berman, H. M., Crystallographic evidence for C-alpha-H center dot center dot center dot O=C hydrogen bonds in a collagen triple helix. Journal of Molecular Biology 1996, 264 (4), 734-742.

43. Xu, Y. J.; Hyde, T.; Wang, X.; Bhate, M.; Brodsky, B.; Baum, J., NMR and CD spectroscopy show that imino acid restriction of the unfolded state leads to efficient folding. Biochemistry 2003, 42 (29), 8696-8703.

44. Bhatnagar, R.S.; Gough, C.A. CD of Collagen and Related Polypeptides. In *Circular Dichroism and the Conformational Analysis of Biomolecules;* Fasman, G.D., Ed.; Plenum Press: New York, 1996. p 183-199.

45. Engel, J.; Bachinger, H. P., Structure, stability and folding of the collagen triple helix. In Collagen: Primer in Structure, Processing and Assembly, Brinckmann, J.; Notbohm, H.; Muller, P. K., Eds. Springer-Verlag Berlin: Berlin, 2005; Vol. 247, pp 7-33.

46. Mizuno, K.; Boudko, S. P.; Engel, J.; Bachinger, H. P., Kinetic Hysteresis in Collagen Folding. Biophysical Journal 2010, 98 (12), 3004-3014.

47. Boudko, S.; Frank, S.; Kammerer, R. A.; Stetefeld, J.; Schulthess, T.; Landwehr, R.; Lustig, A.; Bachinger, H. P.; Engel, J., Nucleation and propagation of the collagen triple helix in single-chain and trimerized peptides: Transition from third to first order kinetics. Journal of Molecular Biology 2002, 317 (3), 459-470.

48. Ackerman, M. S.; Bhate, M.; Shenoy, N.; Beck, K.; Ramshaw, J. A. M.; Brodsky, B., Sequence dependence of the folding of collagen-like peptides - Single amino acids affect the rate of triple-helix nucleation. Journal of Biological Chemistry 1999, 274 (12), 7668-7673.

49. Frank, S.; Boudko, S.; Mizuno, K.; Schulthess, T.; Engel, J.; Bachinger, H. P., Collagen triple helix formation can be nucleated at either end. Journal of Biological Chemistry 2003, 278 (10), 7747-7750.

50. Ottl, J.; Battistuta, R.; Pieper, M.; Tschesche, H.; Bode, W.; Kuhn, K.; Moroder, L., Design and synthesis of heterotrimeric collagen peptides with a built-in cystine-knot - Models for collagen catabolism by matrix-metalloproteases. Febs Letters 1996, 398 (1), 31-36.

51. Shah, N. K.; Ramshaw, J. A. M.; Kirkpatrick, A.; Shah, C.; Brodsky, B., A host-guest set of triple-helical peptides: Stability of Gly-X-Y triplets containing common nonpolar residues. Biochemistry 1996, 35 (32), 10262-10268.

52. Persikov, A. V.; Ramshaw, J. A. M.; Kirkpatrick, A.; Brodsky, B., Peptide investigations of pairwise interactions in the collagen triple-helix. Journal of Molecular Biology 2002, 316 (2), 385-394.

53. Persikov, A. V.; Ramshaw, J. A. M.; Kirkpatrick, A.; Brodsky, B., Electrostatic interactions involving lysine make major contributions to collagen triple-helix stability. Biochemistry 2005, 44 (5), 1414-1422.

54. Krishna, O. D.; Kiick, K. L., Supramolecular Assembly of Electrostatically Stabilized, Hydroxyproline-Lacking Collagen-Mimetic Peptides. Biomacromolecules 2009, 10 (9), 2626-2631.

55. Holmgren, S. K.; Taylor, K. M.; Bretscher, L. E.; Raines, R. T., Code for collagen's stability deciphered. Nature 1998, 392 (6677), 666-667.

56. Bretscher, L. E.; Jenkins, C. L.; Taylor, K. M.; DeRider, M. L.; Raines, R. T., Conformational stability of collagen relies on a stereoelectronic effect. Journal of the American Chemical Society 2001, 123 (4), 777-778.

57. Inouye, K.; Sakakibara, S.; Prockop, D. J., EFFECTS OF STEREO-CONFIGURATION OF HYDROXYL GROUP IN 4-HYDROXYPROLINE ON TRIPLE-HELICAL STRUCTURES FORMED BY HOMOGENEOUS PEPTIDES RESEMBLING COLLAGEN. Biochimica Et Biophysica Acta 1976, 420 (1), 133-141.

58. DeRider, M. L.; Wilkens, S. J.; Waddell, M. J.; Bretscher, L. E.; Weinhold, F.; Raines, R. T.; Markley, J. L., Collagen stability: Insights from NMR spectroscopic and hybrid density functional computational investigations of the effect of electronegative substituents on prolyl ring conformations. Journal of the American Chemical Society 2002, 124 (11), 2497-2505.

59. Pugliese, R.; Gelain, F., Peptidic Biomaterials: From Self-Assembling to Regenerative Medicine. Trends in Biotechnology 2017, 35 (2), 145-158.

60. Knight, C. G.; Morton, L. F.; Peachey, A. R.; Tuckwell, D. S.; Farndale, R. W.; Barnes, M. J., The collagen-binding A-domains of integrins alpha(1)beta(1) and alpha(2)beta(1) recognize the same specific amino acid sequence, GFOGER, in native (triple-helical) collagens. Journal of Biological Chemistry 2000, 275 (1), 35-40.

61. Mhanna, R.; Ozturk, E.; Vallmajo-Martin, Q.; Millan, C.; Muller, M.; Zenobi-Wong, M., GFOGER-Modified MMP-Sensitive Polyethylene Glycol Hydrogels Induce Chondrogenic Differentiation of Human Mesenchymal Stem Cells. Tissue Engineering Part A 2014, 20 (7-8), 1165-1174.

62. Wojtowicz, A. M.; Shekaran, A.; Oest, M. E.; Dupont, K. M.; Templeman, K. L.; Hutmacher, D. W.; Guldberg, R. E.; Garcia, A. J., Coating of biomaterial scaffolds with the collagen-mimetic peptide GFOGER for bone defect repair. Biomaterials 2010, 31 (9), 2574-2582.

63. Krishna, O. D.; Jha, A. K.; Jia, X. Q.; Kiick, K. L., Integrin-mediated adhesion and proliferation of human MSCs elicited by a hydroxyproline-lacking, collagen-like peptide. Biomaterials 2011, 32 (27), 6412-6424.

64. Shinde, A.; Feher, K. M.; Hu, C.; Slowinska, K., Peptide internalization enabled by folding: triple helical cell-penetrating peptides. Journal of Peptide Science 2015, 21 (2), 77-84.

65. Wang, A. Y.; Mo, X.; Chen, C. S.; Yu, S. M., Facile modification of collagen directed by collagen mimetic peptides. Journal of the American Chemical Society 2005, 127 (12), 4130-4131.

66. Yu, S. M.; Li, Y.; Kim, D., Collagen mimetic peptides: progress towards functional applications. Soft Matter 2011, 7 (18), 7927-7938.

67. Wang, A. Y.; Foss, C. A.; Leong, S.; Mo, X.; Pomper, M. G.; Yu, S. M., Spatio-temporal modification of collagen scaffolds mediated by triple helical propensity. Biomacromolecules 2008, 9 (7), 1755-1763.

68. Li, Y.; Foss, C. A.; Summerfield, D. D.; Doyle, J. J.; Torok, C. M.; Dietz, H. C.; Pomper, M. G.; Yu, S. M., Targeting collagen strands by photo-triggered triple-helix hybridization. Proceedings of the National Academy of Sciences of the United States of America 2012, 109 (37), 14767-14772.

69. Chattopadhyay, S.; Guthrie, K. M.; Teixeira, L.; Murphy, C. J.; Dubielzig, R. R.; McAnulty, J. F.; Raines, R. T., Anchoring a cytoactive factor in a wound bed promotes healing. Journal of Tissue Engineering and Regenerative Medicine 2016, 10 (12), 1012-1020.

70. Urello, M. A.; Kiick, K. L.; Sullivan, M. O., A CMP-based method for tunable, cell-mediated gene delivery from collagen scaffolds. Journal of Materials Chemistry B 2014, 2 (46), 8174-8185.

71. Sigg, S. J.; Postupalenko, V.; Duskey, J. T.; Palivan, C. G.; Meier, W., Stimuli-Responsive Codelivery of Oligonucleotides and Drugs by Self-Assembled Peptide Nanoparticles. Biomacromolecules 2016, 17 (3), 935-945.

72. Despanie, J.; Dhandhukia, J. P.; Hamm-Alvarez, S. F.; MacKay, J. A., Elastin-like polypeptides: Therapeutic applications for an emerging class of nanomedicines. Journal of Controlled Release 2016, 240, 93-108.

73. Rodriguez-Cabello, J. C.; Prieto, S.; Reguera, J.; Arias, F. J.; Ribeiro, A., Biofunctional design of elastin-like polymers for advanced applications in nanobiotechnology. Journal of Biomaterials Science-Polymer Edition 2007, 18 (3), 269-286.

74. Urry, D. W., Physical chemistry of biological free energy transduction as demonstrated by elastic protein-based polymers. Journal of Physical Chemistry B 1997, 101 (51), 11007-11028.

75. Urry, D. W., PROTEIN ELASTICITY BASED ON CONFORMATIONS OF SEQUENTIAL POLYPEPTIDES - THE BIOLOGICAL ELASTIC FIBER. Journal of Protein Chemistry 1984, 3 (5-6), 403-436.

76. Perczel, A.; Hollósi, M,. Turns. In Circular Dichroism and the Conformational Analysis of Biomolecules; Fasman, G.D., Ed.; Plenum Press: New York, 1996. p 285-381.

77. Urry, D. W.; Gowda, D. C.; Parker, T. M.; Luan, C. H.; Reid, M. C.; Harris, C. M.; Pattanaik, A.; Harris, R. D., HYDROPHOBICITY SCALE FOR PROTEINS BASED ON INVERSE TEMPERATURE TRANSITIONS. Biopolymers 1992, 32 (9), 1243-1250.

78. Chilkoti, A.; Dreher, M. R.; Meyer, D. E., Design of thermally responsive, recombinant polypeptide carriers for targeted drug delivery. Advanced Drug Delivery Reviews 2002, 54 (8), 1093-1111.

79. Meyer, D. E.; Chilkoti, A., Quantification of the effects of chain length and concentration on the thermal behavior of elastin-like polypeptides. Biomacromolecules 2004, 5 (3), 846-851.

80. Urry, D. W., ENTROPIC ELASTIC PROCESSES IN PROTEIN MECHANISMS .1. ELASTIC STRUCTURE DUE TO AN INVERSE TEMPERATURE TRANSITION AND ELASTICITY DUE TO INTERNAL CHAIN DYNAMICS. Journal of Protein Chemistry 1988, 7 (1), 1-34.

81. Reguera, J.; Urry, D. W.; Parker, T. M.; McPherson, D. T.; Rodriguez-Cabello, J. C., Effect of NaCl on the exothermic and endothermic components of the inverse temperature transition of a model elastin-like polymer. *Biomacromolecules* **2007,** *8* (2), 354-358.

82. Reiersen, H.; Clarke, A. R.; Rees, A. R., Short elastin-like peptides exhibit the same temperature-induced structural transitions as elastin polymers: Implications for protein engineering. *Journal of Molecular Biology* **1998,** *283* (1), 255-264.

83. Li, B.; Alonso, D. O. V.; Daggett, V., The molecular basis for the inverse temperature transition of elastin. *Journal of Molecular Biology* **2001,** *305* (3), 581-592.

84. Meyer, D. E.; Chilkoti, A., Purification of recombinant proteins by fusion with thermally-responsive polypeptides. *Nature Biotechnology* **1999,** *17* (11), 1112-1115.

85. MacEwan, S. R.; Chilkoti, A., Elastin-Like Polypeptides: Biomedical Applications of Tunable Biopolymers. Biopolymers 2010, 94 (1), 60-77.

86. MacKay, J. A.; Chen, M. N.; McDaniel, J. R.; Liu, W. G.; Simnick, A. J.; Chilkoti, A., Self-assembling chimeric polypeptide-doxorubicin conjugate nanoparticles that abolish tumours after a single injection. Nature Materials 2009, 8 (12), 993-999.

87. Luo, T. Z.; He, L. R.; Theato, P.; Kiick, K. L., Thermoresponsive Self-Assembly of Nanostructures from a Collagen-Like Peptide-Containing Diblock Copolymer. Macromolecular Bioscience 2015, 15 (1), 111-123.

88. Luo, T. Z.; Kiick, K. L., Noncovalent Modulation of the Inverse Temperature Transition and Self-Assembly of Elastin-b-Collagen-like Peptide Bioconjugates. Journal of the American Chemical Society 2015, 137 (49), 15362-15365.

89. Luo, T. Z.; David, M. A.; Dunshee, L. C.; Scott, R. A.; Urello, M. A.; Price, C.; Kiick, K. L., Thermoresponsive Elastin-b-Collagen-Like Peptide Bioconjugate Nanovesicles for Targeted Drug Delivery to Collagen-Containing Matrices. Biomacromolecules 2017, 18 (8), 2539-2551.

90. Petros, R. A.; DeSimone, J. M., Strategies in the design of nanoparticles for therapeutic applications. Nature Reviews Drug Discovery 2010, 9 (8), 615-627.

91. Monici, M., Cell and tissue autofluorescence research and diagnostic applications. Biotechnology Annual Review, Vol 11 2005, 11, 227-256.

92. Yanagisawa, O.; Homma, T.; Okuwaki, T.; Shimao, D.; Takahashi, H., Effects of cooling on human skin and skeletal muscle. European Journal of Applied Physiology 2007, 100 (6), 737-745.

Chapter 2

MATERIALS AND METHODS

This chapter details the methods and procedures used for peptide synthesis and purification, conjugate synthesis and purification, as well as the characterization techniques used to study these products. Section 2.1 discusses peptide synthesis and purification including: background, procedures, synthesis issues, and corrective measures. ELP-CLP conjugate synthesis is highlighted in section 2.2 and purification techniques are examined. Lastly, section 2.3 explains the background and procedures of the characterization methods employed in the analysis of peptides and conjugates.

2.1 Peptide Synthesis and Purification

A brief summary of solid phase peptide synthesis background, motivation, and procedures is first reviewed followed by an explanation of the techniques used for purification of these peptides. Lastly, synthesis problems and solutions are discussed.

2.1.1 Solid phase peptide synthesis

2.1.1.1 Background and motivation

The chemical synthesis of peptides on a solid polymer support matrix has become the method of choice for peptide construction ever since it was first introduced by Bruce Merrifield nearly 55 years ago.[1] This is primarily because of the ease in removing reagents and solvent by simple washing, allowing for the method's implementation with automated equipment.[2,3] The method, now known as solid phase

peptide synthesis (SPPS), begins with the coupling of an N-protected α-amino acid carboxyl group to a polymer matrix bound chemical linker. The chemical linker possesses either an amino or hydroxyl (also chloro) functionality for which an activated form of the C-terminal carboxyl (typically reactive ester) of the N-protected α-amino acid can react via amidation or esterification respectively.[1] Similar to the N-terminus, any sidechains located on the α-carbon will also possess a 'permanent' protecting group, leaving the first residue on the solid support to have all functionalities totally protected. The SPPS process continues by removal of the N-terminal temporary protecting group using a specific chemistry that does not affect the 'permanent' sidechain protecting group on the α-carbon or the peptide itself.[2]

With the N-terminus of the first residue deprotected, the subsequent amino acid can be reacted in the same manner as the first via amide coupling. The deprotection and coupling steps are continuously repeated and the peptide sequence is generated linearly from the C to N termini.[2,3] The SPPS process concludes by the cleavage of the peptide from the solid support using either a harsh or mild acid.[2] The cleavage process usually simultaneously removes all 'permanent' α-carbon sidechain protecting groups at the same time; though this does not necessarily have to be the case.[4] The removed protecting groups are then sequestered by scavenger reagents included in the cleavage cocktail and the peptide can then be precipitated from the cleavage solution and later purified.[2,3,4] The entire SPPS process is detailed in Figure 2.1.

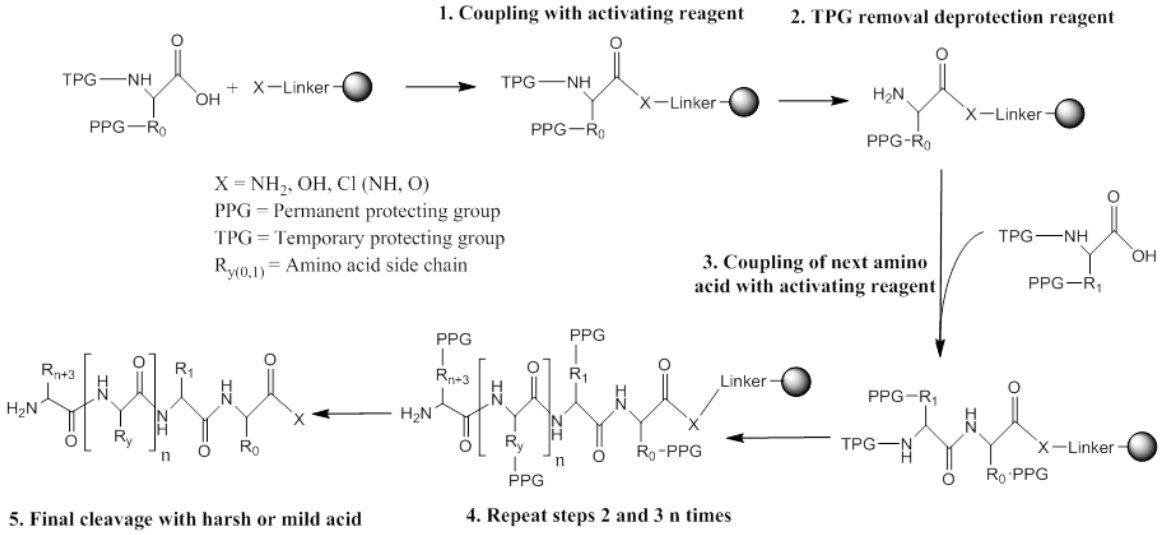

Figure 2.1: Generalized procedure of SPPS.

The coupling reaction of the first residue to the chemical linker and all subsequent residue couplings are typically done in an amide solvent such as N,N-Dimethylformamide (DMF) and involve the conversion of the N-protected α-amino acid carboxyl functionality to an activated ester. This is usually done by first generating the carboxylate of the N-protected α-amino acid using a tertiary amine such as N,N-Diisopropylethylamine (DIPEA) or N-methylmorpholine, followed by ester activation with either a uronium or phosphonium based coupling reagents such as 2-(1H-benzotriazol-1-yl)-1,1,3,3-tetramethyluronium hexafluorophosphate (HBTU) or (Bezotriazol-1-yloxy)tripyrrolidinophosphonium hexafluorophosphate (PyBOP), respectively.[2] There exists a plethora of activating reagents used in amide bond formation and have been extensively reviewed elsewhere.[5,6]

Historically there are two standard deprotection schemes employed in SPPS: the fluorenylmethyloxycarbonyl/tert-butyl (Fmoc/tBu) and tert-

butyloxycarbonyl/benzyl (Boc/Bzl) methods.[2] The former uses the base-labile Fmoc group for N-α-amino protection, acid-labile resin linker (for cleavage), as well acid-labile α-carbon sidechain protection groups such as trityl, tert-butyl, etc.[2,4] For this strategy, the Fmoc group is almost always removed by 20% v/v piperidine in DMF and cleavage/side-chain deprotection is typically performed with some variation of a 95% v/v trifluoracetic acid (TFA)-based cleavage cocktail, with the other 5% v/v being comprised of scavenger reagents (water, triisopropylsilane) that quench the reactive cationic species generated by the cleaved sidechain protecting groups.[4]

The latter strategy employs a mild acid-labile Boc group for N-α-amino protection, a harsh acid-labile benzyl group on the resin linker, as well as on the α-carbon side chain protecting groups.[2] The Boc group is typically removed by the addition of pure TFA and the Bzl linker/protecting groups are removed by hydrofluoric acid (HF).[2,4]

Modern synthesis laboratories chiefly use the Fmoc/tBu strategy due to the possibility of the Boc/Bzl strategy compromising the peptide's integrity from HF treatment, and also because it is the safer alternative for researchers.[2] Fmoc/tBu preprotected amino acids, solid support resins, and coupling reagents are commercially available from a number of different vendors (CEM, AAPPTec, Protein Technologies, etc) and most of these vendors also sell automated peptide synthesizers. These synthesizers can carry out couplings, deprotections, and even cleavages with minimal labor required by the user.

There are several advantages and disadvantages to using SPPS to produce synthetic peptides as compared to recombinant expression techniques. The advantages include: facile inclusion of bioorthogonal chemical functionalities, fine tunability of

sequences (no truncations), and the potential for fast synthesis times.[7,8] With the right synthesizer, a 30 residue peptide that contains chemical orthogonal functionalities (azides, alkynes, hydrazine) and/or fluorescent probes (e.g. fluorescein) can be made in a single day. The primary disadvantages of SPPS are that only sequences of approximately 50 residues or less can be made successfully and large scale quantities of peptide cannot be generated cheaply or easily.[2,7]

Ultimately, the sequence length and composition dictate which method should be used. With respect to this work, ELPs and CLPs of 30 residues or less were desired. ELPs have been shown to have great success in being produced with recombinant methods; so much so, that ELPs are commonly incorporated as fusion constructs for LCST purification purposes.[9] On the other hand, CLPs containing hydroxyproline (such as those in this work) cannot so easily be made with recombinant strategies due to the fact that some prokaryotic systems, like *Escherichia coli* (*E. Coli*), do not contain prolyl hydroxylase enzymes required for proline post-translational modification to hydroxyproline.[10] However, developments in recent years have shown that coexpression of mimivirus prolyl and lysyl hydroxylases with human collagen type III constructs have been able to produce hydroxylated collagen in *E. Coli*.[10,11] Unfortunately, low yields and insufficient post-translational modifications remain significant problems for these methods, with one report claiming a yield of 90mg of hydroxylated collagen per liter of culture; approximately half of what would be yielded by a 0.2 mmol SPPS synthesis scale.[11,12]

With these facts in mind, the simplest method of synthesizing hydroxyproline containing CLPs would be SPPS. Furthermore, the incorporation of the azide and alkyne functionalities into CLPs and ELPs respectively for their subsequent

conjugation, is extremely facile through the use of SPPS to easily generate these materials. Still, SPPS can have its own difficulties, as will be discussed in section 2.1.3.

2.1.1.2 Procedures

All peptides were synthesized following the Fmoc/tBu SPPS strategy. Fmoc L-amino acids (Fmoc-L-valine-OH, Fmoc-L-glycine-OH, Fmoc-L-proline-OH, Fmoc-L-phenylalanine-OH, Fmoc-L-hydroxyproline(tBu)-OH) were purchased from AAPPTec, LLC (Louisville, Kentucky, United States). Special amino acids (Fmoc-L-propargylglycine, 4-azidobutyric acid) and activator HBTU were purchased from ChemPep Inc. (Wellington, Florida, United States). Ethyl (hydroxyimino)cyanoacetate (Oxyma) and polyethylene glycol-polystyrene based Rink Amide resin (Rink Amide ProTide® resin) was purchased from CEM Corporation (Matthews, North Carolina, United States). Piperidine, N,N'-Diisopropylcarbodiimide (DIC), trifluoroacetic acid, triisopropylsilane (TIS), and tertiary amines, DIPEA and N-methylmorpholine, were purchased from Sigma-Aldrich, Inc. (St. Louis, Missouri, United States). DMF and dichloromethane (DCM) solvent were purchased from Thermo Fisher Scientific (Waltham, Massachusetts, United States).

Two peptide synthesizers were used for the production of peptides discussed in this work. A Liberty Blue® (LB) microwave peptide synthesizer by CEM Corporation (Matthews, North Carolina, United States) was used for all ELP peptide synthesis and some CLP synthesis. All syntheses on the LB synthesizer (both ELP and CLP) were conducted with the same number of washes, coupling and deprotection concentrations/volumes/times, and microwave power settings. Bulk solutions of 0.2 M Fmoc amino acid in DMF were made for each amino acid and connected to the

instrument. Likewise, a 1M solution of DIC and a 1M Oxyma solution with 0.1 M added DIPEA were also prepared in DMF and connected to the instrument. Lastly, a bulk DMF bottle and a bottle containing 20% v/v piperidine in DMF were also attached to the LB. All syntheses were performed with a 0.18 mmol/g loading Rink Amide (ProTide®) resin with a 0.1mmol resin basis. In general, a single coupling of an amino acid entailed the following: two deprotection steps with a wash in between, five wash steps after the second deprotection, and two coupling steps followed by two more washes. For coupling, the instrument was programed to dispense 1 mL of DIC solution, 0.5mL of basic Oxyma solution, and 2.5 mL of amino acid solution yielding 5 fold molar excess of base and amino acid over the resin and a 10 fold excess of activator over the resin. Four minute coupling times were performed at 90°C for each coupling step. Deprotection steps dispensed 4 mL of deprotection reagent and took place for two minutes at 90°C.

At the 0.1 mmol scale the Liberty Blue® peptide synthesizer produces C-terminal alkynlated ELPs in fairly high purity and with yields ≥ 140mg. As will be discussed in more detail in section 2.1.3, syntheses of CLPs with the Liberty Blue consistently yield proline and hydroxyproline amino acid deletions (hereafter termed PO deletions) in significant abundance. These PO deletions seem to be ubiquitous to the synthesizer itself, as other groups that own a LB synthesizer have reported the exact same PO deletions with CLP syntheses. Numerous modifications to the microwave synthesis protocol have been attempted and an exhaustive list of parameters and yields is beyond the bounds of this document, but no method has yet managed to obtain high yield and high purity of CLP. Furthermore, the PO deletions are not easily separable by standard methods and equipment. Fortunately, I report in

section 2.1.3 a special method of purification that produces exceptionally pure CLPs, albeit in small but useable quantities.

In order to obtain pure CLPs in high quantities a new protocol was developed for CLP synthesis on a Protein Technologies Tribute® peptide synthesizer (Tucson, Arizona, United States). Previous reports in our group and others (unpublished) have suggested that hydroxyproline deletions are common with the Tribute® synthesizer. I hypothesized that such deletions were caused by insufficient hydroxyproline dissolution as opposed to being instrument related. Fmoc-L-hydroxyproline(tBu)-OH is typically sold as hard crystalline material that is significantly difficult to break up and dissolve. In order to circumvent this problem, a coffee grinder was used to pulverize the hydroxyproline, thereby increasing the surface area to volume ratio of the amino acid; kinetically aiding dissolution of the material. With the hydroxyproline prepared, 1.2 mmol of amino acid (Gly, Pro, or Hyp) and activator HBTU were weighed into vials (one vial per coupling step) and inserted into the synthesizer in order from C to N terminus. Bottles of pure DMF, 20% v/v piperidine in DMF, dichloromethane, and 0.4 M N-methylmorpholine in DMF were prepared and attached to the Tribute® instrument.

All CLPs synthesized on the Tribute® were synthesized in the same manner with a 0.18 mmol/g loading Rink Amide (ProTide®) resin at a 0.2mmol synthesis scale with every residue being double coupled. The overall programing for each amino acid coupling involved 12 quick resin washes (DMF and DCM), deprotection cycles, 8 more solvent washes, a coupling step, and 5 more washes. Deprotection cycles were run until no dibenzofulvene bioproduct UV absorbance was detected at 304nm. Double and single coupling steps involved nitrogen bubbling dissolution of 1.2 mmol

amino acid and HBTU with 6 mL of DMF. This preactivated mixture was then dispensed to the resin and the coupling reaction was allowed to proceed for 1.5 hours with continuous vortex and nitrogen bubbling stirring.

For all CLPs, 4-azidobutyric acid was coupled to the N-terminus for subsequent click chemistry reactions with ELP. Because azides are known to be heat and light sensitive, 4-azidobutyric acid was coupled manually to the resin. Briefly, 0.2 mmol of resin containing already synthesized CLP was transferred to a 25 mL peptide synthesis reaction vessel and washed with DMF three times. For preparation of the azide coupling solution, 3 mmol (15 fold excess over resin) of 4-azidobutanoic acid were weighed into a 10 mL scintillation vial. Two milliliters of DMF were added to the vial followed by 3.2 mmol (557 μL) of DIPEA. The contents of the scintillation vial were briefly mixed and left to stand for about 5 minutes. After that time, 2.85 mmol (about 1 gram) of HBTU was weighed and added to the vial along with 3mL of DMF. A small stir bar was added and the scintillation vial contents were allowed to mix on a stir plate for approximately 20 minutes. This process allows for full preactivation of the 4-azidobutyric acid to a reactive ester. After twenty minutes the contents of the vial were transferred to the wet CLP resin in the 25mL peptide synthesis vessel along with ten more milliliters of DMF. The final concentration of the amino acid was 0.2mmol/mL. The coupling reaction vessel was then placed onto a mechanical shaker and was shaken for 2.5 hours. After completion of the reaction the resin was washed three times with free DMF and filtered out using nitrogen gas. This entire process was repeated once more as a double coupling step.

Given that nearly every amino acid (both ELPs and CLP with the exception of hydroxyproline) had no protecting groups present, the cleavage of all peptides

followed identical protocols. The process begins by transferring peptide functionalized resin to a clean 25mL peptide synthesis reaction vessel. The resin is typically washed with DMF three times and blown dry with nitrogen gas for five minutes. The cleavage cocktail used for all peptides consisted of 15mL of 95% v/v TFA, 5%v/v water, and 5% v/v TIS. The cleavage cocktail was premixed and then poured into the peptide synthesis reaction vessel with the resin. The vessel was capped and sealed and put onto the shaker with a shaking time of three hours being used for all peptides. Once the reaction was complete, the peptide now in solution was dispensed into a 50mL conical tube using nitrogen gas to pass the fluid through the sintered glass filter on the peptide synthesis vessel. The resin was subsequently washed with 10mL of neat TFA and dispensed into the same 50mL conical tube to collect the peptide remaining in the wet resin.

Nitrogen gas was then blown directly into the TFA/peptide solution in order to facilitate evaporation of the TFA, concentrating the peptide solution. After about 40 minutes of evaporation the volume in the 50mL conical tube was typically about 5mL. This remaining volume was the added into cold anhydrous ethyl ether giving rise to peptide precipitate. The ethyl ether/peptide precipitate was then centrifuged at 4000 RPM for 7 minutes at 4°C in order to form a peptide pellet, with the ethyl ether supernatant being poured off afterward. The ethyl ether process was repeated once more to further remove any lingering scavenger molecules. The subsequent pellet was air dried for one hour at ambient conditions and then dissolved in water and acetonitrile and lyophilized for 60 hours, ultimately yielding a dry crude product.

2.1.2 Purification

2.1.2.1 Reverse phase high performance liquid chromatography (RP-HPLC) background

The international union of pure and applied chemistry defines chromatography as the following:[13]

> A physical method of separation in which the components to be separated are distributed between two phases, one of which is stationary (stationary phase) while the other (the mobile phase) moves in a definite direction.

This broad definition encompasses many different types of chromatography that vary in many different ways, including: the physical state of one or more of the phases (liquid or gas chromatography), the separation mechanism (affinity columns, ion-exchange, size exclusion, adsorption), or the shape (thin layer or column chromatography).[14] For peptide scientists, a particular type of chromatography called Reverse Phase High Performance Liquid Chromatography (RP-HPLC) is typically used for peptide purification.[2] The discussion here is intended as a conceptual overview of RP-HPLC and a more thorough review of the subject is given by several texts.[14-16]

As the name states, RP-HPLC is a liquid based column chromatography method where the mobile phase is polar (typically water) and the stationary phase is non-polar. The reason for the 'reverse phase' name is because it was developed second (chronologically) to the 'normal phase' method in which the mobile phase is non-polar and the stationary phase is polar.[17] In RP-HPLC a set of compounds to be separated is dissolved and injected into the mobile phase. The mobile phase is then pumped to a column that is packed with alkyl chain functionalized silica particles that are stationary and hydrophobic relative to the polar mobile phase.[15,16] The separation of

the analyte compounds is based on the relative affinity/adsorption of the compounds with both the solvent (mobile phase) and the alkyl chain silica particles (stationary phase) due to hydrophobic interactions.[15] In general, more hydrophobic compounds will have a greater 'likeness' for the hydrophobic alkyl silica particles relative to the polar mobile phase and therefore be retained longer in or around the porous silica bead stationary phase. Compounds that are more hydrophilic will still interact with the alkyl silica particles, but will preferentially spend more time in the polar mobile phase and ultimately elute out of the column faster than more hydrophobic compounds.[16] The overall retention of the compound analyte can be altered by either changing the alkyl chain length on the stationary phase (more or less hydrophobic) or by modifying the polarity of the mobile phase.[17] For peptide RP-HPLC purification, a C-18 column is commonly used, and because this parameter is difficult to change, the polarity is almost always modified via the mobile phase.[4]

It is a common misconception that hydrophobic compounds loaded onto a column will be 'irreversibly' bound to the column until a more non-polar mobile phase is passed through the column (similar to affinity chromatography). A hydrophobic compound loaded onto a RP-HPLC column with a constant (isocratic) polar mobile phase will eventually elute, however it may do so at impractically long time scales (several hours).[17] Because of the unreasonably long retention time of hydrophobic compounds, RP-HPLC is typically done with a gradient change to the mobile phase polarity. This is accomplished by gradually increasing the amount of organic non-polar solvent in the mobile phase over time. By adding a water miscible non-polar solvent to the mobile phase, hydrophobic compounds will have a weaker affinity or 'likeness' for the hydrophobic silica particles and consequently spend more time in the

mobile phase and elute out of the column sooner.[17] Furthermore, the added organic solvent gradient can allow a researcher more precise control over the retention and resolution of eluted peaks by being able to control the rate (or steepness) of addition of organic solvent to the mobile phase. The net result of the gradient elution HPLC is faster purification times and better control of elution properties relative to isocratic methods that maintain a constant polarity over time.

The choice of the non-polar organic solvent added to the mobile phase over time can be important. Many properties of the solvent such as water miscibility, viscosity, boiling point, UV absorbance (discussed later), and toxicity must be considered.[14,17] However the most important characteristic of the non-polar solvent to be considered is its polarity relative to water. The polarity of the organic solvent can greatly impact the retention and resolution of analyte compounds being eluted from the column. Organic non-polar solvents commonly added to the aqueous mobile phase from most polar to least polar include: methanol, acetonitrile, isopropanol, and tetrahydrofuran.[18] The choice of organic solvent is largely based on the type of analyte being purified. For peptide purification acetonitrile is the most common non-polar solvent used for gradient elution.[4]

Another important parameter of RP-HPLC is the pH of the mobile phase which should be controlled based on the pKa of the analyte. A mobile phase that has a pH approximately close to a compounds pKa will result in a compound elution with tailing peaks due to the compound being in equilibrium with its ionized and unionized form.[16,17] Ionized species will be slightly more hydrophilic than their corresponding unionized species and will therefore elute out slightly faster. It is usually best to choose the pH that will make the analyte as hydrophobic as possible in order to

improve retention time and separation. Though care must be taken to ensure that the pH used will not damage the column being used as some column silica packings possess silanol groups that can be damaged by high pH's.[15,16]

The last important parameter to be considered is the temperature of the column. In general increasing the temperature of a column and subsequently its mobile and stationary phases, decreases retention times and allows for RP-HPLC systems to be run at higher flow rates due to the decreased viscosity of the mobile phase.[17] The temperature to be used is highly dependent on the characteristics of the analyte as column selectivity or analyte stability can both depend on the temperature used.

After an analyte column is eluted it must be detected to actually determine when it was eluted. The most common eluent detector for standard RP-HPLC is ultra violet (UV) light absorption, though refractive index detectors can also be used.[17] The use of UV detection requires some prior knowledge of the analyte so that a relevant absorbing wavelength for the analyte can be input into the system for detection. For peptides a wavelength of 214 nm is almost always chosen as this is the absorption wavelength for amide bonds in the peptide backbone.[4] Alternatively, 254nm and 284nm can be used for phenylalanine and tyrosine (respectively) detection as well.

As the peptide product is eluted and subsequently detected a chromatogram of the absorbance over time is displayed informing the operator to begin collection of the mobile phase/product stream. Some RP-HPLC systems are equipped with automatic fraction collectors that can collect the different products/impurities as they are eluted. The collected product is then either evaporated using a rotary evaporator or lyophilized to obtain pure peptide product.[4]

2.1.2.2 Procedures

2.1.2.2.1 RP-HPLC purification of peptides

All peptides were purified in nearly the same manner with small differences in parameters being applied between CLPs and ELPs. Both ELPs and CLPs were purified using a Waters Xbridge BEH130 Prep C-18 column (Waters Inc., Milford, MA, United States). Prior to purification, 8L of water containing 0.1%v/v TFA and 4L of acetonitrile containing 0.1%v/v TFA were sparged with helium for five minutes, connected to the HPLC tubing and primed. After the initial cleavage of peptide from the resin, roughly 200mg of crude CLP was dissolved in 5mL of 95% v/v water and 5%v/v acetonitrile solution and was passed through a 0.2μm PVDF 13 mm diameter filter. The 95%v/v water and 5%v/v acetonitrile solution composition was used as the starting conditions for the column which was equilibrated for 10 minutes at a flow rate of 24mL/min. A gradient increase of 1%acetonitile v/v per minute was programmed to start from 5% to 75% v/v acetonitrile in 70 minutes at a flow rate of 24 mL/min. To reduce the number of collected fractions, a single injection of the 5mL CLP solution was injected into a mobile phase that led to a 55°C column.

In contrast to the CLP, approximately 200mg of crude ELP was dissolved in 5ml of 73%v/v water and 27% v/v acetonitrile and passed through a 0.2μm PVDF 13 mm diameter filter. The composition of water and acetonitrile for this solution was used as the starting conditions of the method and the column was equilibrated at these conditions for 10 minutes at a flow of 24mL/min. Again, a 1% acetonitrile per minute gradient increase was used for the gradient elution that took place over 68 minutes and ended with a 95% v/v acetonitrile composition. The method began with a 5mL injection of the ELP solution directly to mobile phase that led to a 40°C column. For

both ELP and CLP methods, 100%v/v acetonitrile was flushed through the column to ensure no peptide was retained.

For both ELP and CLP the UV absorbance was monitored at 214 nm and fractions were collected into 50mL conical tubes. Liquid chromatography mass spectrometry (LC-MS) analysis was done of the fractions directly post purification. After analysis, the fractions were subsequently frozen in liquid nitrogen and lyophilized for 60 hours to obtain pure dry peptide product.

It should be noted that azide modified CLPs were protected from light as much as possible throughout cleavage and purification, as azide decomposition has previously been observed. This seemed to be especially important during the lyophilization process.

2.1.2.2.2 Mass directed RP-HPLC of PO deleted peptides

Prior to mass directed purification, all peptides containing PO deletions were first purified using the prep scale purification methods detailed above. This was necessary to remove failed azide conjugations, possible large peptide truncations, as well as the small molecule impurities typically found in the crude sample post peptide cleavage.

A Waters AutoPurification™ system (Milford, MA, United States) equipped with a single quadrupole SQD2 electrospray ionization mass spectrometer, a 2998 photodiode array detector, and two 515 makeup pumps was used for mass directed separation of PO deleted sequences from bulk CLP peptides. Bottle setup of the system entailed the following: the two main pump lines were connected to 4L of 0.1%v/v formic acid in acetonitrile and 4L of 0.1%v/v formic acid in water, one makeup pump composed of methanol was used to feed sample to the SQD2 ESI mass

spectrophotometer, and another makeup pump composed of acetonitrile was used to feed the autosampler valve, the primary acetonitrile pump line. Prior to purification all bottles were purged of air bubbles in the following manner: one minute at 75mL/min for primary lines and three minutes at 5mL/min for makeup pump lines. Lastly, cell culture tubes were placed in racks for fraction collection and the collection bed was reset through the software.

Two primary methods were developed for the system, one method was used for $(GPO)_8GG$ and azide-$(GPO)_8GG$ purification in smaller quantities, and a second method was used for azide-$(GPO)_6GG$ and azide-$(GPO)_3GFOGER(GPO)_3GG$ purification in larger quantities; though due to their similarity, either method can probably be used for any CLP PO deletion separation. No method was used for azide-$(GPO)_7GG$ because enough pure peptide was managed to be collected in the first prepscale purification round.

For the first method, azide-$(GPO)_8GG$ was dissolved in 95% v/v water and 5% v/v acetonitrile to a concentration of 5mg/mL and filtered through 0.2um, 13 mm diameter PVDF filter into an HPLC autosampler vial. This composition was used as the starting and equilibration conditions for the column, with equilibration time being 5 minutes at 20 mL/min. The method was run at 20mL/min using a 1.25 % acetonitrile per minute gradient that lasted four minutes, increasing from 5% v/v acetonitrile to 10% v/v acetonitrile in that time. After four minutes, the 10% v/v acetonitrile composition was maintained for another three minutes, after which the composition returned to starting conditions in less than one minute. The entire method lasted approximately 8 minutes per injection. Injection volumes ranging from 100µL to 250 µL of 5 mg/mL concentration were run and multiple injections allowed for the

collection of useable quantities of material. The fraction collector was programmed to automatically collect fractions matching those of the desired expected product (without PO deletions) as well as the PO deletions (if collection of the impurity was desired). As an example for the purification of $(GPO)_8GG$, the fraction collector was programmed to start collecting when it detected the 687.37 m/z adduct (PO deletion) in high enough quantity or when it detected the 757.4 m/z adduct (no PO deletion) in high enough quantity. The $(M+3H)^{3+}$ adducts were chosen because these are the adducts that ionized in highest quantity as detected by the Xevo-qTOF mass spectrophotometer (see Figure 2.3).

In the second method, peptides were dissolved in 90% v/v water and 10% v/v acetonitrile to final concentrations ranging from 40 mg/mL to 10 mg/mL. These solutions were filtered through a 0.2 μm pore size, 13 mm diameter PVDF filter into autosampler vials. The dissolution conditions of the peptides were used as the starting conditions of the method as well as the equilibration of the column, which was done for 5 minutes at 20mL/min. The method was run at 20mL/min using a 0.5% acetonitrile per minute gradient that lasted for ten minutes, increasing from 10% v/v acetonitrile to 15% v/v acetonitrile in that time. After the first ten minutes the 15%v/v acetonitrile composition was maintained for three minutes with a total elution period of 13 minutes. At 13.10 minutes, the acetonitrile composition was increased to 90%v/v acetonitrile for four minutes, after which the column was returned to the starting conditions and equilibrated for 5 minutes. The total run time of the method was twenty two minutes and as just detailed, includes a column cleanout protocol (90% v/v acetonitrile) as well as re-equilibration at starting conditions so that the method can be

repeated without needing to manually flush and equilibrate the column after every injection.

Injections for this method ranged from 500 µL to 1000 µL with sample concentrations ranging from 10 mg/mL to 40 mg/mL. After every injection, the peptide sample solution was diluted two fold so that the next injection could be performed. The m/z [$(M+3H)^{3+}$] adducts monitored for both azide-$(GPO)_3$GFOGER$(GPO)_3$GG and azide-$(GPO)_6$GG were 766.26 and 819.01respectively for the PO deleted ions, and 836.44 and 924.16 respectively for the desired product ions.

For both methods, fractions were collected in glass cell culture tubes and combined/transferred to 50mL conical tubes. The glass cell culture tubes were washed with deionized water and the washes were collected to ensure no remaining dissolved peptide remained. Combined fractions were lyophilized, reconstituted, and lyophilized again until enough useable product was generated.

2.1.2.2.3 RP-HPLC of ELP-CLP conjugates

Purification of ELP-CLP conjugates was necessary to remove any unreacted peptide as well as excess copper (I) acetate molecules. Purification of all conjugates was performed on a Prominence chromatography instrument (Shimadzu, Inc., Columbia, MD, United States) that was equipped with a C18 Viva® column (Restek, Lancaster, PA, United States). Prior to purification, 0.1%v/v TFA in water and acetonitrile solutions were made and sparged with helium for 10 minutes. The prominence instrument was then allowed to autopurge for 30 minutes.

All conjugates were dissolved in 1 to 1.5mL of approximately 70%v/v water and 30% v/v acetonitrile. Due to the abundance of copper byproducts the resulting

solution is fairly transparent but significantly colored (either a golden brown hue or dark green depending on the copper oxidation state).

Since there was the possibility of particle self-assembly, the conjugate solution, a 70% water and 30% acetonitrile solution, a 13mm diameter 0.2μm pore size filter, syringes, and needles were all incubated at approximately 60°C for twenty minutes using a forced convection oven. The heat ensured that the CLP triple helix was not formed and particle assembly did not occur. After twenty minutes, the filter was preflushed with the water/acetonitrile solution, followed by filtration of conjugate solution into an HPLC autosampler vial (Thermo Fisher Scientific, Waltham, Massachusetts, United States).

The instrument purification method utilized the same starting conditions as the respective conjugate solution that was being purified. All conjugate purifications were performed with a 8mL/min flowrate and 1% acetonitrile/min gradient that lasted for approximately 65 minutes and ended with a final acetonitrile composition of 95%v/v. The column temperature used for all conjugate purifications was 60°C and at this temperature the column was allowed to equilibrate at starting conditions for 10 minutes at a flow rate of 8mL/min. Just before injection, the filtered conjugate solution was incubated in a 60°C water bath for 15 minutes to again ensure triple helix melting and the highest solubility of the conjugate. After 15 minutes the sample was quickly moved to the HPLC autosampler rack and an automated injection of 1mL of the conjugate solution was initiated using the HPLC software.

UV absorbance was monitored at 214 nm and elution fractions were collected manually into 50mL conical tubes. The samples were then analyzed via LC-MS, frozen with liquid nitrogen, lyophilized and allowed to dry for 60 hours.

2.1.3 Problems and solutions with peptide synthesis

2.1.3.1 Amino acid deletions in microwave peptide synthesis

As was briefly discussed in section 2.1.1.2, the beginnings of this project dealt with problematic PO deletions whenever CLPs were synthesized on the Liberty Blue peptide synthesizer. At the time, protocols previously developed for the Tribute® synthesizer were not conducive to hydroxyproline sequences, and the apparent speed and efficiency offered by the Liberty Blue® synthesizer was a most enticing prospect. Since an ideal synthetic protocol had not been (nor is presently) made, I developed a protocol using a unique purification strategy to instead remove the problematic PO deletions.

As an example of the issue at hand, Figure 2.2 below demonstrates a typical RP-HPLC chromatogram (UV-absorbance at 214nm over time) of a cleaved CLP peptide synthesized on the LB peptide synthesizer, in this case $(GPO)_8GG$.

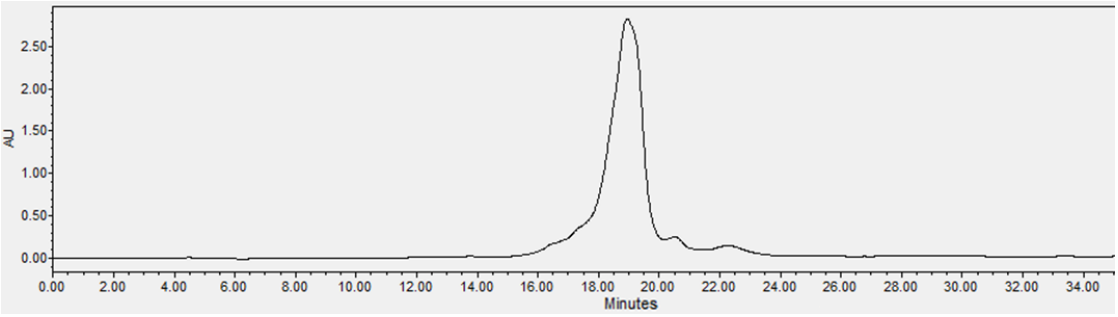

Figure 2.2: Preparation scale, RP-HPLC chromatogram of $(GPO)_8GG$. Y-axis is relative absorbance units of UV-214nm wavelength and X-axis is retention time.

As can be seen in Figure 2.2, only a single eluted peak of peptide was observed. This would normally indicate that a very pure peptide has been synthesized given that no major truncated peptides were eluted earlier. However, electrospray ionization mass spectrometry (ESI-MS) indicates that this is not the case as shown in Figure 2.3.

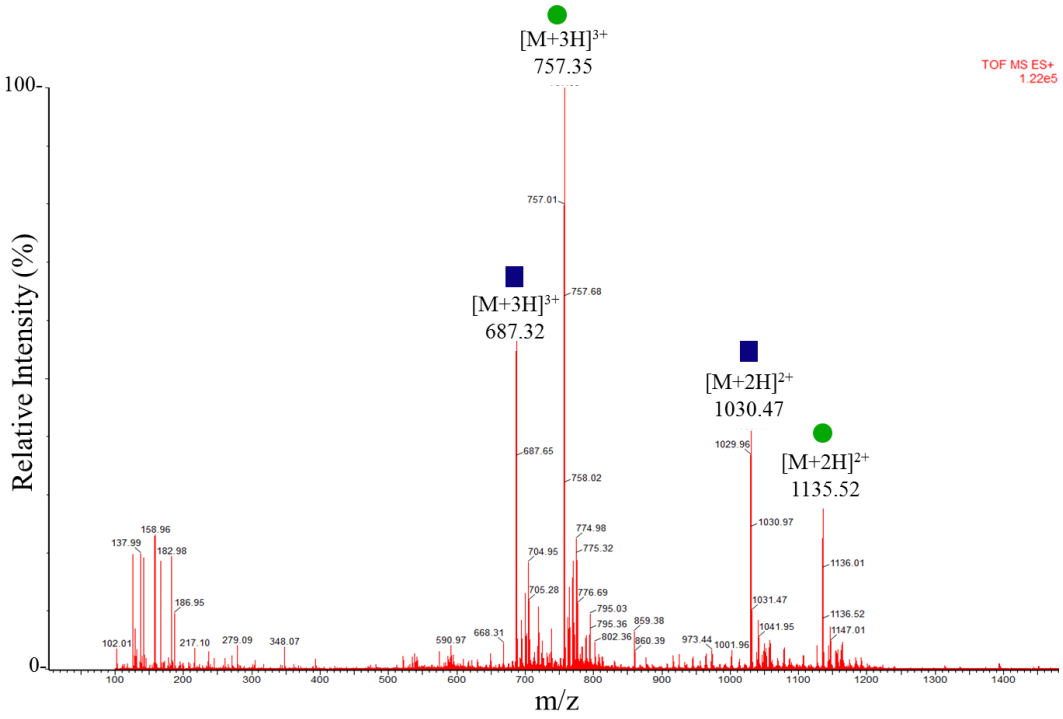

Figure 2.3: Electrospray ionization mass spectroscopy result of eluted $(GPO)_8GG$ peptide from Figure 2.2. Green circles are the expected product $(GPO)_8GG$ and blue squares are the expected product but with a PO deletion.

The mass spectra in Figure 2.3 illustrate the PO deletion problem with LB syntheses of CLPs. The exact mass of the $(GPO)_8GG$ peptide is 2268.04 Da which corresponds to the following verified adducts: m/z = 1135.52 $[(M+2H)^{2+}$, calcd =

1135.02] and m/z = 757.35 [$(M+3H)^{3+}$, calcd = 757.02]. The exact mass of $(GPO)_8GG$ peptide with a P and O deletion is 2057.94 Da and corresponds to the following verified adducts: m/z = 1030.47 [$(M+2H)^{2+}$, calcd = 1029.27] and m/z = 687.32 [$(M+3H)^{3+}$, calcd = 686.98]. From Figure 2.3 alone the exact quantity of the PO deletions cannot be determined, but it can be said that PO deleted peptide is ionizing with significant enough abundance relative to the desired product that it is very likely that the deletion impurities make up a significant portion of the eluted peptide product.

Given that a 1% acetonitrile v/v increase per minute gradient was resulting in incomplete separation of the impurity, a different separation approach was needed. The University of Delaware Mass Spectrometry Facility has a Waters AutoPurification™ system that can separate materials on the basis of their mass spectra as opposed to the standard UV-absorbance spectra that is typically used in RP-HPLC. This system is not only capable of visualizing the real time mass spectra of elution products, but can precisely collect fractions based on the relative abundance of mass spectra ions that are detected.

The real benefit of the mass directed purification was being able to visualize the separate peptide components by their mass. This greatly aided the trial and error process of method development. Eventually a fast method with low acetonitrile gradient and a terminal isocratic step resulted in sufficient separation, as detailed in section 2.1.2.2.2. Typical chromatograms outputted by the method are shown in Figure 2.4 and include ion specific chromatograms as well as photodiode array detection at the 214nm wavelength.

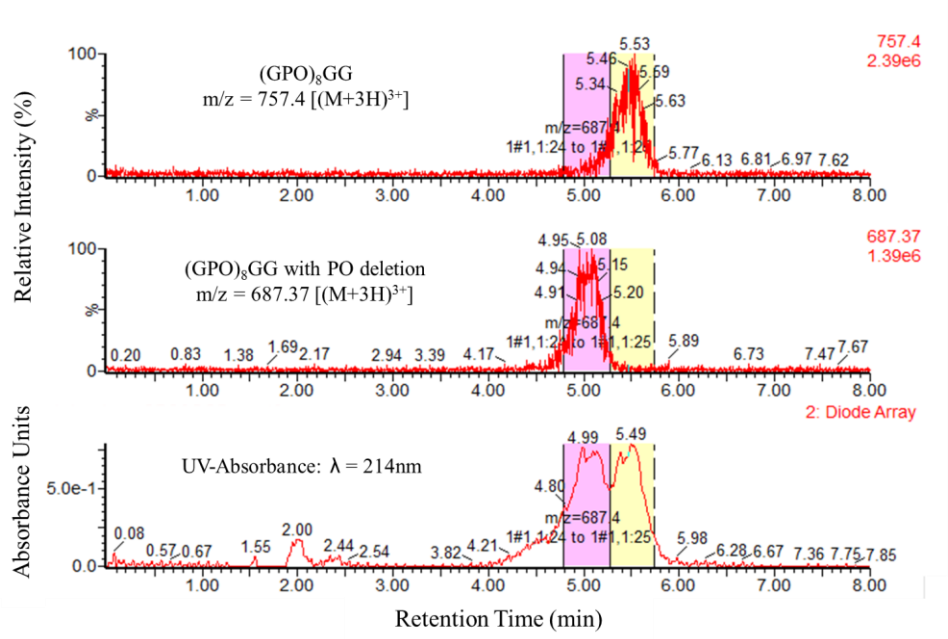

Figure 2.4: AutoPurification output of $(GPO)_8GG$, illustrating the separation of the expected product and PO deletion products via their respective ion chromatograms. The photo diode array detection at a wavelength of 214nm is included as well.

In Figure 2.4 the respective ion chromatograms of $(GPO)_8GG$ peptide and $(GPO)_8GG$ peptide with a PO deletion are shown. The purple and yellow boxes highlighting the peaks represent different collected fractions. Since the PO deleted peptide was collected in a vial represented by the purple box, and the desired peptide was collected in a separate vial represented by the yellow box, the two products were effectively separated on the basis of their mass. Even though the UV absorbance detection appears to show the separation as well, developing a method on the basis of UV alone would have been difficult. Furthermore, the mass detection method is more precise and the collection managed by the computer can begin promptly after mass detection of the product.

To further demonstrate the success of the purification, fractions of $(GPO)_8GG$ PO deletion impurity and expected product $(GPO)_8GG$ were collected, lyophilized, and analyzed using the Xevo ESI-qTOF liquid chromatographic mass spectrometer. The resulting mass spectra of the two separated fractions are shown in Figure 2.5. By comparison of Figure 2.5 to Figure 2.3, the separated products now each have their own corresponding spectra, very clearly indicating that they have been separated from one another. Similar results to those of Figures 2.4 and Figure 2.5 were obtained for Azide-$(GPO)_6GG$ and Azide-$(GPO)_3GFOGER(GPO)_3GG$ using similar chromatographic methods detailed in section 2.1.2.2.2.

With working protocols for purification, the LB synthesizer can now be used to make reliable CLPs. This is especially important for groups new to CLP synthesis that may not have access to different types of synthesizers. Since syntheses on the LB typically take no more than a day, multiple peptides can be made in a very short time period and subsequently purified to achieve highly pure analytical quantities of CLP that can be further characterized downstream with instruments such as circular dichroism (CD), differential scanning calorimetry, or Fourier transform infrared spectroscopy (FT-IR). If multiple CLPs of the same sequence are made repeatedly over the course of a few days, then useable quantities of CLP for downstream reactions such as ELP-CLP conjugation can be obtained.

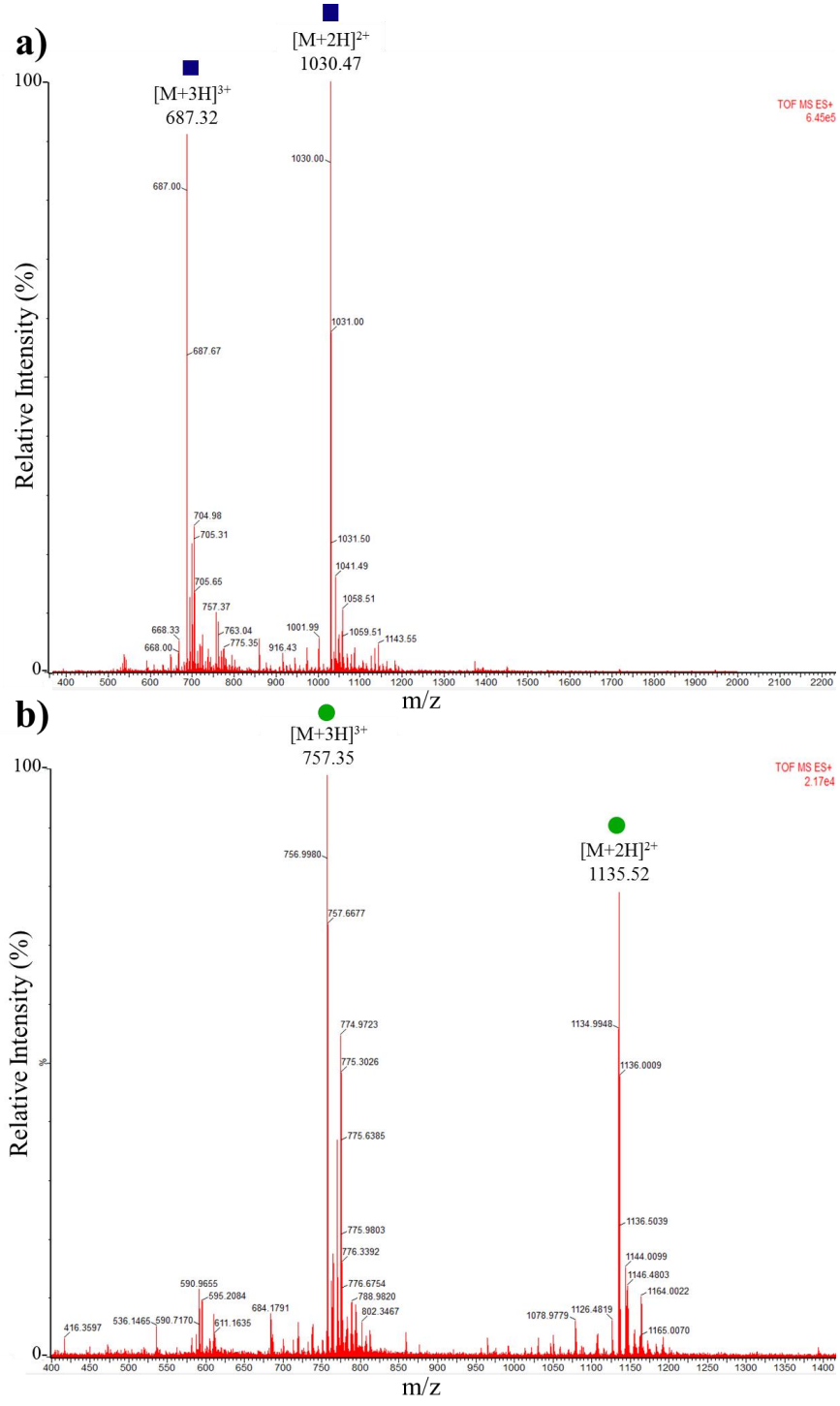

Figure 2.5: ESI-MS result of separated fractions a) $(GPO)_8GG$ with PO deletions (blue squares), and b) $(GPO)_8GG$ without PO deletions (green circles).

2.1.3.2 Apparent azide degradation on N-termini of CLPs

Another common problem observed with syntheses is the apparent degradation of a significant fraction of azide conjugated CLPs. A typical chromatogram of a non-azide conjugated peptide (free amine N-terminus) is shown in Figure 2.2 above. However, a chromatogram such as that seen in Figure 2.6 below is observed for cleaved azide conjugated CLPs.

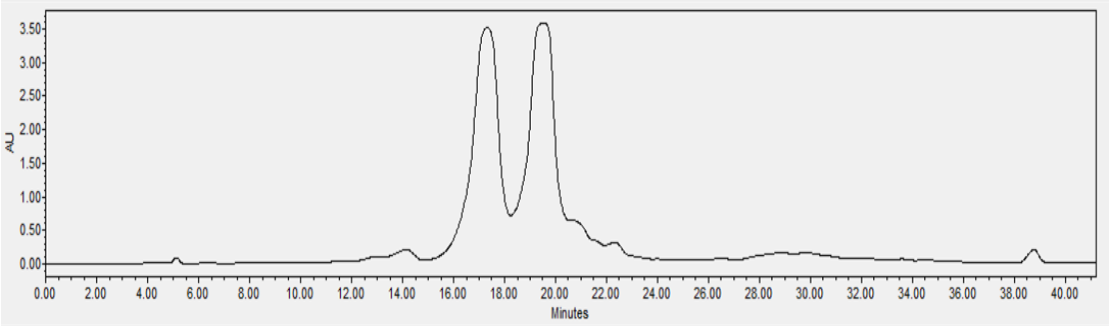

Figure 2.6: Typical HPLC chromatogram (214nm absorbance) of azide conjugated CLP. This chromatogram corresponds to azide$(GPO)_3$GFOGER $(GPO)_3$GG. Two distinct peaks are observed indicating significant impurities present.

As can be seen in Figure 2.6 above and by comparison to Figure 2.2, significant impurities are imparted onto CLP peptide after conjugation with 4-azidobutanoic acid. Upon analysis with mass spectrometry (data not shown), the left peak corresponds to $(GPO)_3$GFOGER$(GPO)_3$GG with a mass that is only 11 Da different than what would be expected from azide conjugated product (m/z = 1247.55 $[(M+2H)^{2+}$, calcd = 1246.54] and m/z = 832.03 $[(M+3H)^{3+}$, calcd = 831.02]). The right peak fortunately is the expected product, though with PO deletions possibly being present depending on the choice of synthesizer (m/z = 1253.53 $[(M+2H)^{2+}$,

calcd = 1253.08] and m/z = 836.02 [$(M+3H)^{3+}$, calcd = 835.7]). While expected product is being made, Figure 2.6 highlights the less than ideal yield that is approximately 50% in value. Furthermore, this reduced yield occurs for all CLP azide systems. The low yield inevitably results in the need for additional syntheses in order to acquire enough material for downstream ELP conjugations.

Azide conjugation to CLPs is carried out manually following the protocols discussed above. Double couplings are usually performed and the success of the conjugation is typically verified using a Kaiser ninhydrin test kit (Anaspec, Fremont, CA, United States) which is a colormetric test for detecting the presence of free-amines of peptide resin.[4] In the case of azide conjugated CLPs, a negative result (no observed color change) indicates that the N-terminal amine was indeed modified with azide compound, and this is the typically what is indeed observed compared to free-amine resin controls (data not shown).

The source or cause of the added 11 Da mass impurity remains unknown. However, it is known that it apparently does not consist of a free amine (according to Kaiser test) and its polarity is different enough (apparently more polar) from the expected product and that its elution characteristics are different from the expected product. It was initially hypothesized that azide sold by the vendor was perhaps innately impure and that this was the source of the resulting impure CLP conjugations. However, upon analysis of both ^{1}H-nuclear magnetic resonance spectroscopy (NMR) and ^{13}C-NMR of the 4-azido butanoic acid compound (Figure A.1 and A.2 respectively; see appendix A), no aberrant chemical shifts were observed for the carbon and proton atoms adjacent to the electron withdrawing azide group, and the observed chemical shifts correlated well with literature. However, ^{13}C analysis of the

degraded azide-CLP (left peak in Figure 2.6) did indicate the absence of the azide chemical shift (^{13}C data of degraded azide-CLP not shown).

Since the azide-CLP on resin showed to be fully conjugated (no free amines by Kaiser test), and attempts to use different coupling reagents did not seem to alter the resulting 11 Da observed mass (data not shown), it was hypothesized that the cleavage conditions were the root cause of the azide degradation.

In order to test this hypothesis, azide was conjugated to previously cleaved and purified NH_2-$(GPO)_8GG$ in the liquid phase (off-resin). Standard coupling procedures were followed and unreacted reagents were removed via HPLC purification. The resulting chromatogram of the liquid phase azide conjugation is shown in Figure 2.7 below.

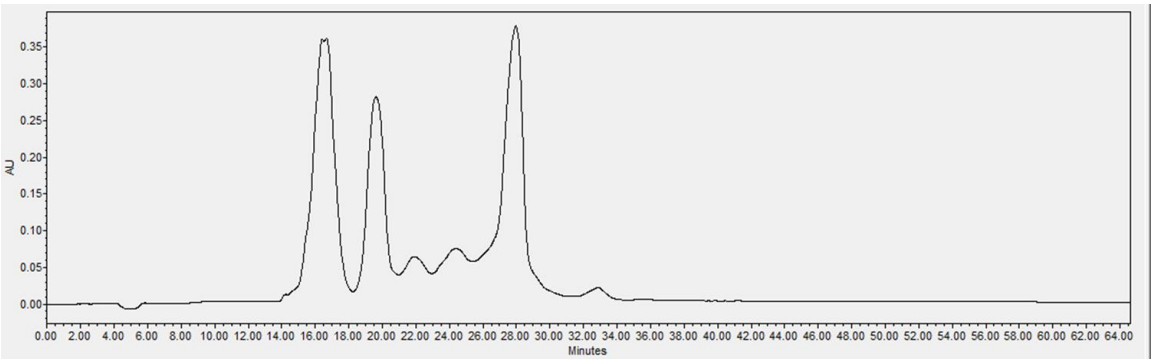

Figure 2.7: HPLC chromatogram (214nm absorbance) of liquid phase conjugation of 4-azido butanoic acid to NH_2-$(GPO)_8GG$.

The three most prominent peaks in Figure 2.7 correspond to the following products as detected by mass spectrometry from left to right: peak 1 is apparently peptide truncations and/or unreacted coupling reagents (not verified), peak 2

corresponds to expected product with a tert-butyl protection group still present (m/z = 1219.64 [$(M+2H)^{2+}$, calcd = 1218.58] and m/z = 813.43 [$(M+3H)^{3+}$, calcd = 812.72]), and peak 3 is pure expected product (m/z = 1191.13 [$(M+2H)^{2+}$, calcd = 1190.54] and m/z = 794.42 [$(M+3H)^{3+}$, calcd = 794.03] (data not shown)). The yields for these peaks were approximately 30% peak 1, 22% peak 2, 42% peak 3. Had the tert-butyl CLP been cleaved then the apparent yield would be approximately 64%. We can possibly say the real yield would be larger if we assume that all of peak 1 is unreacted conjugation reagents.

Out of all the mass spectra collected from the liquid phase conjugation reaction, there was no detection of CLP consisting of an added 11 Da mass. This confirms the hypothesis that the cleavage reaction is responsible for azide degradation. However, it still remains unclear as to what the 11 Da added mass corresponds to. The Schmidt reaction, Curtius rearrangement, and other isocyanate based reaction mechanisms have been considered, but no plausible products have yet to be identified through these mechanisms. Future studies should confirm increased yields via the liquid phase reaction method, and more in depth analysis of azide degraded NMR spectra should be able to provide the structure for the degraded product. This may be useful for identifying new cleavage methods that would leave a significant fraction of the azide intact.

2.2 ELP-CLP Conjugate Synthesis and Purification

2.2.1 Synthesis with azide-alkyne copper catalyzed click chemistry

There are a number of different reactions that have been developed over the years that fit the requirements and criterion needed to be deemed a ‘click’ reaction, as

the term was originally defined by Kolb *et al*.[19] Of these reactions, the copper-catalyzed azide-alkyne cycloaddition (CuAAC) is perhaps the most widely used click reaction around the globe due to its rapid and reliable conjugation of azides and alkynes to 1,4-disubstituted triazoles.[20] The reaction is characterized by being completely bio-orthogonal to native biochemical moieties and largely insensitive to pH changes, coulombic and hydrophobic interactions, π- π stacking, and hydrogen bonding.[20] It is for these reasons that it has been routinely used in biological systems such as protein engineering, drug discovery, and biomaterials design.[21]

The CuAAC reaction method was employed for the conjugation of the C-terminal alkyne ELPs to N-terminal azide CLPs. Due to the high concentrations required and the limited solubility of ELP in water with CLPs, the reaction was performed in anhydrous DMF (Thermo Fisher Scientific Waltham, Massachusetts, United States) with 0.25 equivalents of Cu(I) acetate (Sigma-Aldrich, Inc. St. Louis, Missouri, United States) in the presence of Cu(0) metal wire (Thermo Fisher Scientific Waltham, Massachusetts, United States) at 80°C for 24 hours, following protocols previously established by the Kiick lab.[22,23] More specifically, 6μmol of CLP and ELP were weighed and transferred to a 10mL scintillation vial. Approximately 7-10, 0.5 cm long copper strips were also added to the vessel as reductant for dissolved oxygen/reactive oxygen species so that the Cu(I) acetate does not oxidize to its Cu(II) state. To the vessel about 816μL of anhydrous DMF was added and the peptides were allowed to dissolve. Lastly, a stock solution of 1mg/mL Cu(I) acetate in DMF was prepared. Cu(I) acetate does not readily dissolve in DMF, so the solution was sonicated in a sonicator water bath for 10 min prior to transfer to the main reaction vessel. From this Cu(I) acetate stock, 184μL was added to the reaction vessel yielding

a final concentration of 1.5μmol in 1mL total volume (1.5mM). A stir bar was then added and the reaction vessel's head space was purged with nitrogen gas for thirty seconds and subsequently sealed. The reaction was allowed to proceed for approximately 24 hours while being stirred in an oil bath at 80°C.

When the reaction was complete, the reaction solution was allowed to cool to room temperature and was subsequently precipitated into cold (≈-20°C) anhydrous diethyl ether (Thermo Fisher Scientific Waltham, Massachusetts, United States) in a 50mL conical centrifuge tube. The precipitate was then spun down at 4000 rpm for seven minutes using a Beckman Coulter Allegra X-22R centrifuge. The ethyl ether was poured off and the precipitate was allowed to air dry at room temperature for half an hour. The precipitate was then dissolved in 95%v/v water and 5%v/v acetonitrile, frozen with liquid nitrogen, and lyophilized for 60 hours. Further work-up of the conjugate will be discussed in the following section.

The success of the reaction can be verified by a number of means including ^{1}H-NMR spectroscopy, Fourier transform infrared spectroscopy, and trifluoroethanol gel permeation chromatography.[22] However, reported here for the first time is the successful analysis of these ELP-CLP conjugate products using standard RP-HPLC and liquid chromatography mass spectrometry. It was previously thought that these methods could not be used due to the possibility of insoluble particle formation concerns, but as has been discussed in section 2.1.2.2.3, adaptations to standard protocols enable the use of these methods. More will be discussed regarding the RP-HPLC and mass spectrometry results in the following section.

As will be seen shortly, the CuAAC reaction method utilized by our group works fairly well though with some byproducts and unreacted peptide. Indeed there

are aspects of the reaction conditions that could possibly be optimized to obtain ELP-CLPs in higher yields. Solubility is a notable concern even with DMF as a solvent. This is because of consistent observations of cloudy reaction mixtures both before and after the designated reaction time. The solubility is most likely related to the Cu(I)acetate due to its apparent initial insolubility in DMF by itself. At least one report has recommended significantly lower Cu(I) concentrations (approximately 30 times less then quantities previously reported by our group) for preparative scale organic solvent CuAAC reactions.[22-24] Furthermore, choosing a different Cu(I) source may also be of benefit to solubility. In a 2008 review by Meldal and Tornøe, out of over 200 CuAAC reaction conditions reviewed, none utilized Cu(I) acetate as a Cu(I) source. Alternatively, lowing the reaction scale (peptides and Cu(I)acetate) or utilizing a different solvent such as DMSO or considering a co-solvent system may be beneficial for improving the CuAAC reactants solubility.

Another issue could be the oxidation of Cu(I) acetate species to unreactive Cu(II)acetate or Cu(II)oxide. Cu(I) acetate has a dark green/brown color. As the reaction proceeds, the color of the reaction solution usually shifts from green to brown to golden yellow. These changes however, seem to be fairly inconsistent from batch to batch. It is speculated that the color is loosely indicative of the oxidation state, as the color transition seems to correlate with the oxidative layer present on the Cu(0) wire present in the reaction. The amount of Cu(0) added for every reaction on the basis of exposed surface area to solvent is likely quite variable from batch to batch and other variables such as the dissolved oxygen content could also be significantly different between batches. Both of these parameters would affect the oxidation state of the copper species and would explain changes to the Cu(0) oxidative layer and in turn the

color variations as well. In at least one instance when additional copper wire was added to the reaction mixture 6 hours after the reaction was begun, the dark green color (indicative of Cu(I)acetate) was retained and a proportion of the Cu(0) strips did not possess an oxidative layer. It should be noted that the effects of Cu(I) oxidation can go beyond simply quenching the CuAAC reaction. Cu(II) salts have the ability to mediate alkyne-alkyne coupling (Glaser coupling).[20] Furthermore, reactive oxygen species are known to be able to damage biomolecules and contribute to other undesired sidereactions.[26] The possible undesired oxidation of the Cu(I) species as well as the generation of reactive oxygen species may be remedied by studying the effects of the number of copper strips that are added to the reaction vessel in more detail or by degassing the solvent.

Another consideration for future reaction schemes is the inclusion of copper chelating ligands. Copper chelating ligands have been shown to stabilize the Cu(I) oxidation state and as a result, the number of reactive oxygen species and aberrant side-products is lowered.[26] Moreover, the ligands have also been shown to significantly accelerate the CuAAC reaction even without the need for heat.[20,26] A number of these chelating ligands have been reported for both aqueous and organic reaction conditions, and could most likely be employed in the present system.[24]

2.2.2 Methods of purification

After the crude ELP-CLP product is freeze dried, unreacted peptides as well as excess Cu ions need to be removed from the conjugate product. The removal of unreacted peptides is important given that unconjugated CLPs could potentially form triple helices with conjugated ELP-CLPs and therefore limit particle formation if enough CLP is present. Similarly, if Glaser coupling is occurring then ELPs with

double their length will be formed and possibly be in the collapsed state (due to their lower T_t) and form nanoparticle aggregates that can create false positive detection of true ELP-CLP particles. Copper removal is important, not just because of its potential for cell cytotoxicity, but also because of its unwanted spectral properties that could potentially impede conjugate characterization techniques such as CD, DLS, and UV-vis. Indeed, when the crude copper containing ELP-CLP product is dissolved in water an opaque green/brown/gold solution is generated (see Figure A.3 in appendix A). Given that ELP-CLP conjugates should not possess any chromophores in the visible wavelength region, it is highly probable that the observed colored solution is a variation of copper coordinated species. Using this crude conjugate product for characterization resulted in noisy and artefactual data in DLS and CD analyses (data not shown). Therefore, the removal of copper is essential for characterization of ELP-CLP conjugate and resulting nanoparticles.

It was originally reported that dialyzing the crude product against pure water using 1 kDa molecular weight cutoff dialysis tubing successfully removed free copper ions and only trace amounts of unreacted CLP were detected via gel permeation chromatography.[22] While this protocol may indeed output purified product, yields after four days of dialysis approximate around 15% (roughly 5mg out of the 34 mg expected). In an effort to improve the yield, 500 Da molecular weight cutoff tubing was used to attempt to remove copper ions but retain larger amounts of ELP-CLP conjugate product. Surprisingly, copper was found to apparently be retained even after seven days of dialysis. The presence of copper was detected both by visual observation and by UV-Vis absorbance (data not shown). Given the observation that the copper containing solution was brown/gold in color, it was hypothesized that

absorption of light by the transition metal molecules was occurring in the blue region of the visible light spectrum. This was indeed observed and a comparison of visible light absorption at the 400 nm wavelength of copper containing solutions, both before and after dialysis, showed that no significant change in absorbance was observed relative to an equimolar ELP and CLP mixture that does not absorb light in the blue region (data not shown). While the yield for the 500 Da tubing was improved to approximately 80%, the presence of copper remained problematic.

The retention of copper species in the 500 Da dialysis tubing was surprising given that the original Cu(I)acetate species has a molecular weight of 122.5 Da. On the basis of this observation it was hypothesized that copper was coordinating in some manner to either the peptide conjugate or some other unknown moiety.

Given the lack of success with the dialysis removal strategy, other methods were employed to attempt copper removal. The first method attempted was the mixing of the water solubilized crude copper containing ELP-CLP conjugate with Cuprisorb® (Seachem, Madison, GA, United States) resin. This resin is a proprietary chelating matrix designed for copper ion removal in aquatic systems. After 56 hours of gentle mixing of the copper conjugate solution with Cuprisorb® resin beads, the presence of copper was analyzed again by visible light absorbance at 400nm. Similar to the dialysis tubing result, comparison of a sample before and after treatment with the resin showed little change in copper mediated absorption at the 400nm wavelength (data not shown). This result is again indicative of copper being tightly coordinated to some moiety, as the Cuprisorb® resin was designed for chelation with discrete ionized copper species.

Another method attempted was that of RP-HPLC purification. It has been demonstrated in the literature that Cu salts resulting from the CuAAC reaction can be removed on the basis of polarity via an activated basic alumina column.[27] Given that RP-HPLC also separates components on the basis of polarity; it was reasoned that the copper salts could be removed in this manner. Furthermore, the use of HPLC would allow for the facile determination of reaction purity and yields with regard to other peptidic species. With these motivations in mind, RP-HPLC purification of the copper containing ELP-CLP conjugate was performed using the methods described in section 2.1.2.2.3. Figure 2.8 below is the 214nm UV absorbance chromatogram of the purification of $(VPGFG)_6$-$(GPO)_7GG$ conjugate.

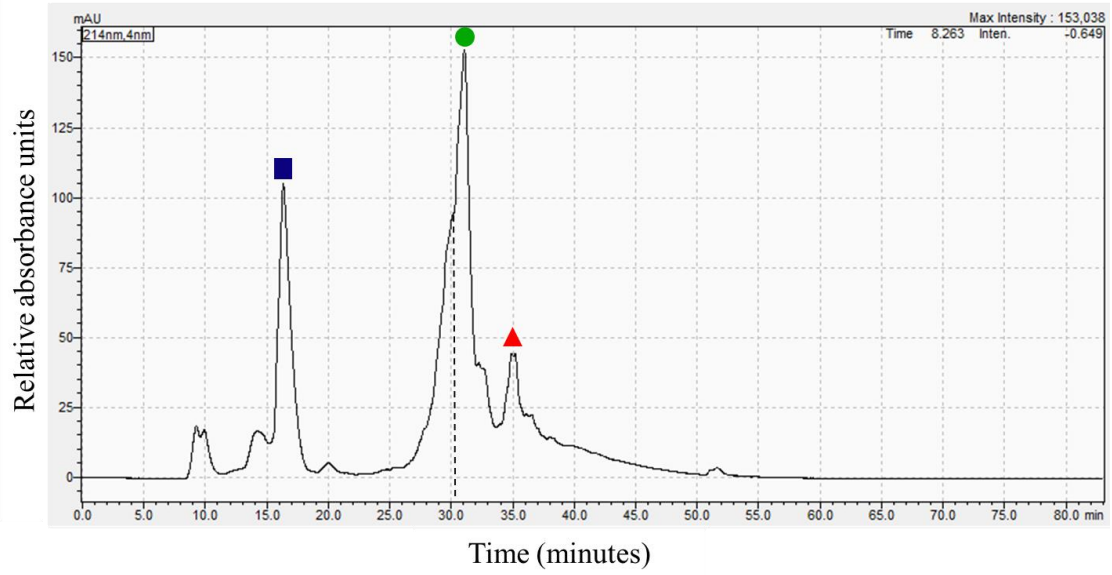

Figure 2.8: RP-HPLC chromatogram of the purification of $(VPGFG)_6$-$(GPO)_7GG$ conjugate. Absorbance was measured at 214nm. The peaks indicated were determined to be the following: blue square- unreacted CLP, green circle- pure ELP-CLP, red triangle- Glaser coupled ELP-ELP. The dashed line distinguishes a change in elution collection due to the change in peak morphology.

The number of peaks eluted in Figure 2.8 indicates the presence of bulk peptide impurities in the crude ELP-CLP product. While no information can be gained from Figure 2.8 regarding the Cu salt removal, the separation of bulk unreacted peptides was still critical for ELP-CLP conjugate purification. Figures 2.9 and 2.10 below illustrate the mass spectra of the three main peaks marked in Figure 2.8. From Figure 2.9a, the peak marked by the blue square corresponds to unreacted azide-$(GPO)_7GG$ peptide. The exact mass of the azide-$(GPO)_7GG$ is 2111.9 Da which corresponds to the following verified adducts: m/z = 1057.45 [(M+2H)2+, calcd = 1056.98] and m/z = 705.3 [(M+3H)3+, calcd = 704.99]). From Figure 2.9b, the peak marked by the green circle corresponds to pure $(VPGFG)_6$-$(GPO)_7GG$ conjugate. The exact mass of $(VPGFG)_6$-$(GPO)_7GG$ is 4967.42 Da which corresponds to the verified mass adducts: m/z = 1243.56 [$(M+4H)^{4+}$, calcd = 1242.86], m/z = 994.64 [$(M+5H)^{5+}$, calcd = 994.49], and m/z = 1657.94 [$(M+3H)^{3+}$, calcd = 1656.8]. Lastly, Glaser coupling was indeed observed and was found in the peak marked by the red triangle in Figure 2.8. The exact mass of alkyne coupled ELP-ELP is 5708.9 Da and corresponds to the observed adducts shown in Figure 2.10: m/z = 1143.47 [$(M+5H)^{5+}$, calcd = 1142.78], m/z = 1429.1 [$(M+4H)^{4+}$, calcd = 1428.23], and m/z = 1905.12 [$(M+4H)^{3+}$, calcd = 1903.97] .

Other smaller peaks shown in Figure 2.8 correspond to traces of impurities typically found in both CLP and ELP purification chromatograms. After performing peak integration, the percentages of the CLP, ELP-CLP, and ELP-ELP were found to be 22%, 30%, and 12% respectively.

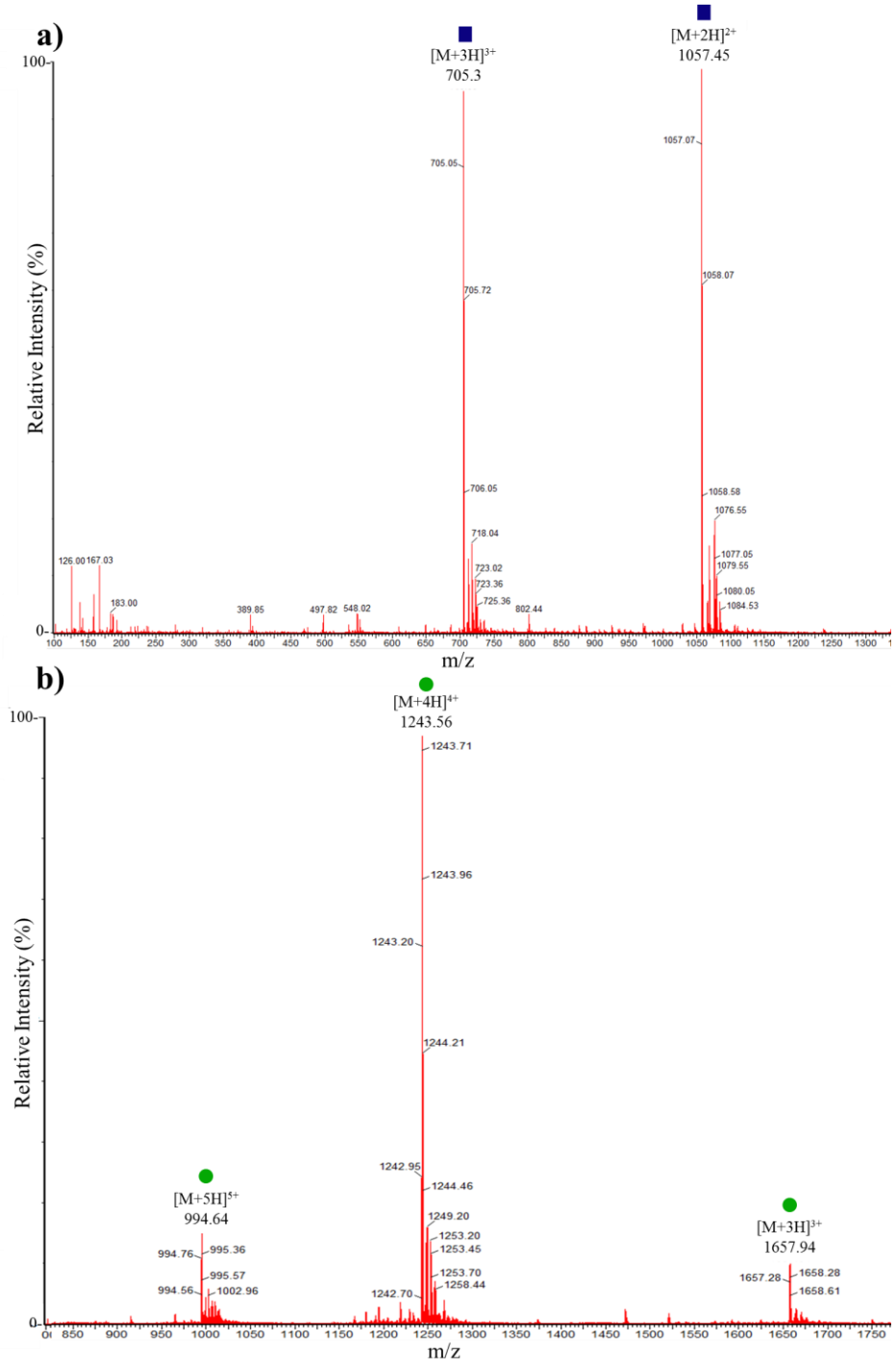

Figure 2.9: Mass spectra of a) unreacted azide-$(GPO)_7GG$ peptide (represented by blue square in Figure 2.8) and b) pure $(VPGFG)_6$-$(GPO)_7GG$ conjugate (represented by green circle in Figure 2.8).

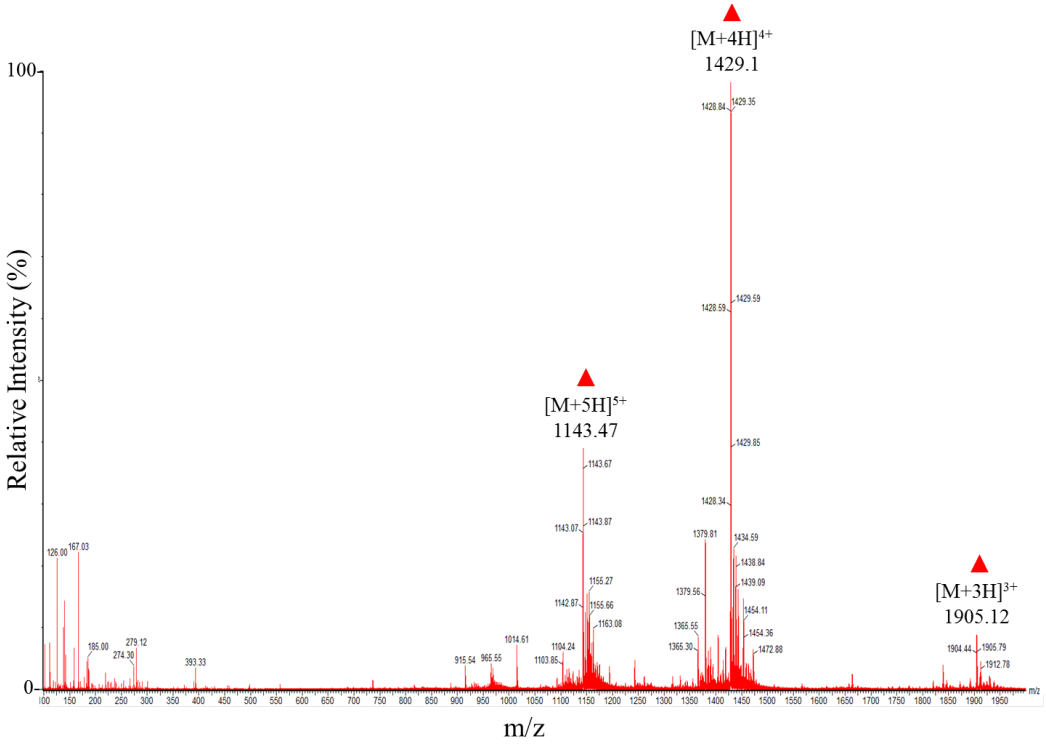

Figure 2.10: Mass spectra of Glaser coupled $(VPGFG)_6$-$(VPGFG)_6$ (represented by red triangle in Figure 2.8).

The relative abundancies of the CLP and the ELP-ELP product correlate well as the ELP-ELP conjugate corresponds to approximately half of the CLP value as would be expected for an equimolar reaction of ELP and CLP for the attempted CuAAC reaction. From the data shown in Figures 2.8 through 2.10 it is evident that the Glaser coupling side reaction is leading to a significant reduction in yield. This is likely occurring due to the previously noted changes in oxidation state of the copper species from Cu(I) to Cu(II), as observed by solution color changes as well as the relative amount of oxide layer formed on the copper wire. At the beginning of the reaction it is likely that the CuAAC reaction does occur. However, overtime the Cu(0) metal

becomes completely oxidized and can no longer carry out the reduction of dissolved oxygen species. The dissolved oxygen then begin to oxidize the Cu(I) to Cu(II) which in turn quenches the CuAAC reaction and mediates Glaser coupling. A recent report has highlighted methodologies to prevent Glaser coupling in ATRP and CuAAC reaction conditions.[28] In that study it was found that the addition of reducing reagents such as tin(II) 2-ethylhexanoate or (+)-sodium-L-ascorbate were capable of eliminating dissolved oxygen and maintaining the presence of Cu(I) species.[28] It is on the basis these observations and suggestions from literature, that the current amount of Cu(0) wire that is added to the reaction is not sufficient for complete reduction of dissolved oxygen. Furthermore, the inclusion of dissolved reducing reagents such as (+)-sodium-L-ascorbate may also be advantageous over solid substrates due to their access to the entire volume of solvent.

With regard to the Cu ion removal, the presence of copper is not readily observed upon dissolution of dried collected HPLC fractions. However, this is only a qualitative measure, and alternative methods such as UV-Vis absorbance or elemental analysis need to carried out to determine the remaining relative abundance of copper species in the purified conjugate products. However, it should be noted that significant quantities are likely separated given the lack of noise and artefactual spectral data from conjugate characterization via DLS and CD.

2.3 Peptide and Conjugate Characterization Methods

2.3.1 Ultraviolet and visible light (UV-Vis) spectroscopy

2.3.1.1 Background

UV-Vis spectroscopy is the most common form of electronic absorption spectroscopy that researchers employ to study and characterize organic chemical compounds. More specifically it is used to study the intensity and energy of light adsorption due to interactions with chemical compounds.[29] All organic compounds are capable of absorbing ultraviolet light and depending on the molecular functional groups present, some compounds may also absorb in the visible spectrum as well.[29] The absorption of light by a chemical compound takes place when energy of incident light is equal to an electronic transition possessed by a sample molecule. This absorption and electronic transition is characterized by an electron that moves from an occupied orbital to a previously unoccupied orbital of the molecule.[29] This electronic transition is usually associated with certain chemical functionalities where valence electrons are found and such chemical moieties that undergo these electronic transitions are termed chromophores. Examples of chromophores include carbonyls, unsaturated bonds (alkenes and alkynes), phenyls, carboxyls, esters, and more.[29]

According to Planck's equation, the energy of light is inversely proportional to its wavelength, and so too is the absorption of light by a chemical compound dependent on wavelength.[29,30]

$$\Delta E = \frac{hc}{\lambda} \tag{2.1}$$

In this equation, h is Plank's constant, c is the speed of light in a vacuum, and λ is the wavelength of light. Utilizing the relation between wavelength, energy, and a

compounds absorption, a UV-Vis spectrum of a chemical compound can be generated by detecting the intensity of light (i.e. its absorption) as a function of wavelength. The spectrum for a particular compound is thus created by plotting light intensity vs. wavelength.

The intensity of light in such a spectrum is related to absorbance and sample concentration through the Beer-Lambert law given by equation 2.2.[29,30]

$$A = \log\left(\frac{I_0}{I}\right) = \epsilon c l \tag{2.2}$$

In this equation, I_0 is the intensity of incident light to a sample system, I is the intensity of transmitted light, ϵ is the molar extinction coefficient (also molar absorptivity) with units liter mole^{-1} cm^{-1}, c is the concentration in mole liter^{-1}, and l is the path length of the system in cm, which is usually the size of the cuvette being used. Absorbance is the parameter that is typically directly measured via the light intensities and related directly to the sample's concentration through the use of a spectrophotometer.

In practice, I_0 is the intensity of light transmitted by a reference cell containing the identical bulk solution that is used for the sample and is termed as a 'blank' and I is the intensity of light that is transmitted after being sent through the sample solution.[29] By doing this, solution/solvent effects are negated and the absorption detected is that solely by the solute chemical compound of interest. The Beer-Lambert law is commonly used for determination of compounds concentration and by monitoring concentration over time, it can be used to calculate reaction kinetics.[29]

Other uses of UV-Vis spectrophotometers do not necessarily rely on the absorption of light by a chemical compound. Spectrophotometers can also be used to measure the difference in light intensities for samples that scatter light rather than

absorb it. These kind of measurements are termed turbidity measurements where the intensity of light measured is a measure of the degree of a sample's ability to scatter, reflect, or prevent light from reaching the detector, usually by scattering the light in directions other than the detector.[31] Typical examples of turbidity measurements include measuring the optical density (OD) of a bacterial cell culture sample or measuring the level of contaminants found in drinking water. [32,33]

In this work turbidity measurements are used for measuring the transition temperature of ELPs going through a phase transition. In this context the transition temperature of an ELP is defined as the temperature at which turbidity reaches 50% of maximal turbidity (or maximal scattering).[31] For these measurements, only the intensity of light I for a sample going through a phase transition is measured relative to the intensity of light I_0 for a 'blank' cuvette that contains only water. The intensity of light I, is then measured as a function of temperature and transition temperature turbidity profiles are generated.

2.3.1.2 Procedures

An Agilent Cary 60 UV-Vis spectrophotometer (Agilent, Santa Clara, CA, United States) equipped with a Versa 20 cuvette holder, TC1 temperature controller, and BATH 10 water batch circulator (Quantum Northwest, Liberty Lake, WA, United States) was used for the determination of transition temperatures of ELPs.

For every temperature transition curve measured, the following procedure was followed. First, approximately 1mg of ELP was weighed into a 3 mL scintillation vial and were subsequently dissolved in approximately 1.5 mL of pure water. Due to the significant insolubility of ELPs in water, the ELP solution was incubated at 4°C for 2 hours. During this time the vial was occasionally rotated to ensure sufficient water

coverage of all remaining undissolved solutes. While the ELP was solubilizing, a Malvern PCAS115 10mmx10mm cuvette (Malvern Instruments, Worcestershire, United Kingdom) was filled with 1mL of pure water and was measured on the UV-Vis spectrophotometer as a blank. Additionally, a stock solution of 1M sodium chloride in water was prepared. After 2 hours, the ELP was completely dissolved and was quickly removed from incubation. A specific volume of the sodium chloride stock was removed and added to the cold dissolved ELP solution so that the final concentration of sodium chloride ranged between 0.05M and 0.75M so that the final concentration of ELP was 0.57mg/mL. This concentration of ELP corresponds to the concentration of ELP molecules in a 1mg/mL solution of $(VPGFG)_6$-$(GPO)_7GG$ conjugate that was used for dynamic light scattering studies.

Immediately after addition of the salt solution to the ELP stock solution, a white cloud was typically observed at the bottom of the cuvette indicating an initial phase separation/temperature transition event. Vortexing the sample gently typically solubilizes the phase separated ELP by dispersing the added salt solution. After initial dissolution, 1mL of the sodium chloride ELP solution was then added to the Malvern cuvette, capped, and then inserted into the UV-Vis cuvette holder. The temperature controller was then immediately set to 5°C or 10°C (depending on salt concentration) and was allowed to incubate in the cuvette holder for 15 minutes. During this time, a Cary 60 Kinetics program was created that monitored 'absorbance' (light intensity) continuously at 600nm for the desired duration of time typically about 12 minutes. During the incubation period the temperature controller was also programmed to increase temperature of the holder by 5°C per minute. When the incubation time was complete both the temperature controller and the kinetics program were started

simultaneously so that temperature increase could be related to the time measured by the instrument. As the temperature increased a phase transition was easily detected due to the scattering of light from the formation of ELP aggregates.

2.3.2 Circular dichroism spectroscopy

2.3.2.1 CD background

Similar to UV-Vis spectroscopy, circular dichroism spectroscopy is a type of electronic absorption spectroscopy. Both UV-Vis and CD operate by the same electron transition principle in which an electron in some ground state orbital is excited to higher energy orbital through the absorption of light.[29] However, there are two notable differences between the spectroscopy methods. First CD utilizes circularly polarized light while UV-Vis uses ordinary non-polarized light.[29] Secondly, CD spectrums are a measure of the difference in left and right circularly polarized light absorptions, while the absorbance in UV-Vis is simply the absorbance.[29.34]

Light is polarized when its electric field vectors vibrate in a single plane as the light propagates in an orthogonal direction.[29] In contrast, ordinary light, like that used for UV-Vis spectroscopy, possess electric field vectors that point in many directions. Circularly polarized light is perhaps best thought of as two orthogonal linearly polarized light waves that are out of phase with one another due to one of the light waves being 'slowed' down by being passed through a birefringence plate.[29,34] The electric field vector components can be summed and the resulting electric field vector is one that rotates about the axis of propagation. This rotation about the axis can be visualized as a spiral or helix that propagates and rotates in the direction of the wave. Depending on which electric field vector is slowed, the resulting circularly polarized

light or 'light helices' can possess either left or right handedness.[34] It is perhaps easiest to visualize this motion of helical propagation as the second hand on a clock that is on a train.[35] If you could trace the exact point of the tip of the second hand over time while both the clock and the train are moving then a helical trace would be observed. The handedness of the helix would then be determined by which direction the second hand of the clock moves (clockwise or counter clockwise).

In circular dichroism spectroscopy, both left and right handed circularly polarized light is sent through a sample and the absorption of each is measured.[34] In ordinary non-chiral or symmetric molecules absorption of both right and left handed light should be equal.[29] However, in chiral or optically active molecules (such as those frequently seen in biology) a difference in absorption between left and right handed circularly polarized light arises.[29] We can think of this in terms of Beer's law (equation 2.2) as specific absorption, where the equation can be rewritten as being specific to left handed light.

$$A_l = \log\left(\frac{I_{0l}}{I_l}\right) = \epsilon_l c l \tag{2.3}$$

Here, equation 2.2 has been rewritten with the subscript (l) to designate the absorption, light intensities, and molar absorptivity as being specific to left hand circularly polarized light.[34] A similar equation and be written with (r) subscripts denoting right handed circularly polarized light absorption. We can then come to the definition of circular dichroism as the difference observed between left and right handed polarized light.[34]

$$\Delta A = A_l - A_r = \epsilon_l c l - \epsilon_r c l = \Delta\epsilon c l \tag{2.4}$$

In practice the ΔA value that is measured is quite small but still distinguishable.[29,34] Since either left or right handed circularly polarized light can be absorbed more than

the other, the ΔA reported in CD can either be positive or negative (in contrast to standard absorbance which is always positive).[29] In achiral or racemic mixtures the value of ΔA is zero.[29]

While these concepts are fairly straightforward, the history of circular dichroism spectroscopy is rooted in optical rotation measurements in which the optical rotation of compounds are studied as opposed to their absorbance.[34] Let us return to the concept of the interpretation of circularly polarized light being the summation of orthogonally polarized linear light beams. In this interpretation, the two linearly polarized beams are equal in magnitude, but remain out of phase with one another.[29] Because the magnitudes of amplitudes of the electric field vectors are equal, a circle helical light path is observed. This is equivalent to the second hand of the clock on the train maintaining its length as it rotates about its origin.

Now consider what occurs when these two orthogonal linearly polarized light beams are sent through a chiral sample that preferentially absorbs one of these linear beams over the other. The result of the transmitted light as it comes out of the sample is that not only are the two linear polarized beams out of sync, but they are also of unequal magnitude.[34] Going back to the clock example where the second hand is the vector summation of each linearly polarized electric field components, we would observe a second hand that changed in size as it moves about its origin. If one could trace the pathway of the tip of the seconds hand in this scenario, then an elliptical helical shape would be observed as opposed to circular helical shape.

This elliptical shape resulting from the difference left and right component absorptions is how circular dichroism is classically utilized.[34] More specifically, the CD instruments polarimeter measures the ratio of the semimajor and semiminor axes

of this elliptical shape.[34] Without going into full detail, this ratio can be related to a measurement angle θ (usually referred to as ellipticity), which in turn can be related to the familiar ΔA previously described by the following equation (see ref 34).[34]

$$\theta = 32.98 * \Delta A \tag{2.5}$$

The units in equation (2.5) are in degrees, but the output of CD spectra is usually that of millidegrees. By combining equation (2.5) and equation (2.4) we get equation (2.6).

$$\theta = 32.98 * \Delta \epsilon c l \tag{2.6}$$

For proteins and peptides this equation is usually converted to a parameter termed the mean residue molar ellipticity (MRE), which is essentially the raw ellipticity normalized by the concentration, path length, and residue content of the protein or peptide in question.[29] The MRE is given by equation (2.7) below.

$$[\theta]_{MRE} = \frac{100*\theta}{N*C*l} \tag{2.7}$$

In equation (2.7), N is the number of residues in the peptide, and the factor of 100 is included as a conversion factor.

Following the discussion, the difference in absorption between left and right handed circularly polarized light is classically reported as ellipticity. The differences in absorption of left and right handed light are not limited to simple small molecule chiral molecules. As discussed, many biological molecules are asymmetric in nature. As a result, proteins and peptides in complex secondary structures create highly unique circular dichroic spectra.[36] Much work has been done in the past to correlate secondary structures of proteins such as alpha helices, beta sheets, and triple helices with specific circular dichroic spectra and have been verified by numerous other techniques.[36] For a complete review of circular dichroism spectra and secondary structures see references 34 and 36.

2.3.2.2 Procedures

A single set of CD data (wavelength and temperature scans) can usually be completed in a 36 hour period. Prior to analysis, approximately 1mg of each CLP peptide and ELP-CLP conjugate was weighed into a 3mL scintillation vial and dissolved in approximately 1.5mL of 10mM Dulbecco's phosphate buffered saline (DPBS) to a final concentration of 0.35mM. The volume of this solution was ensured to be greater than 1mL to guarantee enough solution for CD analysis. The dissolved CLPs were then stored in a 4°C fridge overnight (at least twelve hours) to ensure that the triple helix had ample time to form.

The following day a Hellma 0.2cm cuvette (Hellma analytics, Plainview, New York, United States) was filled with 800μL of 0.2μm filtered 10mM DPBS and inserted into a Jasco 810 circular dichroism spectropolarimeter (Jasco Inc, Easton, MD, USA) to be analyzed as a blank measurement for wavelength scan background subtraction. The parameters used for this blank measurement are identical to those described below for measurement of either the peptide or conjugate sample. The contents of the cuvette were then replaced with the previously dissolved and 0.2μm filtered peptide or conjugate solution. Prior to insertion into the CD instrument, all sides of the cuvette were thoroughly wiped down with ethanol. Upon insertion of the cuvette into the instrument, the temperature setting of the cuvette well was immediately set to 4°C and incubated at this temperature for 1.5 hours to return the CLP solution back to full triple helical formation as a precaution due to the sample briefly being exposed to ambient conditions.

After the 4°C incubation period a wavelength scan analysis was then performed. The wavelength scan range was typically between 250nm and 190nm. All scans were performed with the following parameters: a 1nm band width, a 4 second

response, 1nm data pitch, a scan rate of 10nm/min, with an accumulation of 3, and a measurement sensitivity set to standard mode. Subtraction of the background DPBS blank was automatically performed by the instrument software.

After the 4°C wavelength scan of the samples, a variable temperature analysis was typically performed as described in the following section. The variable temperature analysis is typically programmed to hold the final 80°C temperature after the variable temperature experiment is completed. This is done so that a wavelength scan can immediately be performed at the 80°C temperature following the exact same parameters as those described for the 4°C wavelength scan. All wavelength scan data is outputted as a text file and the millidegree ellipticity data is manually converted to mean residue ellipticity in Microsoft excel.

2.3.2.3 CLP melting temperature determination

After the 4°C wavelength scan is completed a variable temperature analysis can be performed in order to determine the melting temperature of CLPs and ELP-CLP conjugates. The method monitors a certain circular dichroic wavelength (in this case 225nm for the CLP triple helix) as the temperature of the cuvette and sample is slowly heated. For all of the experiments described here, the analysis temperature range was from 4°C to 80°C. Additionally, the following specific parameters were utilized for the variable temperature analysis of peptides and conjugates: a band width of 1nm, a response of 2 seconds, data pitch of 0.5°C (for peptides and ELP-$(GPO)_7$GG) and 0.2°C (for ELP-$(GPO)_6$GG), and a heating rate of 10°C/hour was utilized with the sensitivity mode set to standard.

The output of the variable temperature analysis is a text file of millideg ellipticity data as a function of temperature. This data is imported into Microsoft Excel

(Microsoft corporation, Redmond, WA, United States) and converted to mean residue ellipticity. For CLPs and certain ELP-CLPs, the shape of the melting curve follows a sigmoidal path. It should be noted that for the subtraction of the ELP melting curves from the ELP-CLP melting curves, that the raw millidegree data where first subtracted and then converted to mean residue ellipticity for the conjugate. The mean residue ellipticity data as a function of temperature is then imported into Origin graphing and analysis software (Originlab, Northhampton, MA, United States). Using the Origin software, the melting curves for the CLPs and ELP-CLPs were fitted with the Boltzmann sigmoidal function (except for the ELP-$(GPO)_6$GG conjugate which was fitted with a three parameters exponential function (Exp3P2)). Using the Origin software, the first derivative was taken of the Boltzmann data fits. The fitted functions and their corresponding derivatives were then imported into Microsoft excel and overlaid with the mean residue ellipticity data. The temperature where negative slope of the fitted Boltzmann function is greatest (also the point where the first derivative is a minimum) was defined as the melting temperature for the CLP or ELP-CLP system.

2.3.3 Dynamic light scattering (DLS)

2.3.3.1 DLS background

Dynamic light scattering (DLS), also known as photon correlation spectroscopy, or quasi elastic light scattering, is a non-invasive technique utilized for determining the size of particles with nanometer length scales.[37] In simple terms, the technique relies on the scattering intensity of photons from particulate nanostructures to provide information regarding the movement of these nanoparticles in a solvent system caused by Brownian motion.[37] Brownian motion is the movement of small

particles through a solution where the motion of the particle is the result of rapid bombardment of the particle from surrounding solvent molecules such as water.[38]

In DLS, monochromatic light is sent to a suspension of particles in solution. For particles that do not absorb at the wavelength in question, the light will scatter (technically an absorption event followed by emission) off of the particles into multiple directions.[39] Some of the scattered light from the particles then hits a photosensitive detector, where the light is detected and translated to a digital signal. Because the suspended particles are continuously undergoing Brownian motion and moving in and out of the beam path (fluctuating movements), so too does the relative intensity of the detected scattering light fluctuate.[40] It is in this way that information regarding the particles movement through a solution can be obtained. But how can the movement of particles be related to their size? The answer is through the fundamental works of Einstein in which the diffusion coefficient of a particle was first related to stokes law (relation of flow and drag forces of spherical particles) and as a result also related to the diameter of the sphere or particle.[41] Today this relation is known as the Stokes-Einstein equation and is given below.[40]

$$d(h) = \frac{kT}{3\pi\eta D} \tag{2.8}$$

In this equation, d(h) designates the hydrodynamic diameter (distinguished as the diameter in solution rather than dried geometric diameter), k is Boltzmann's constant, T is temperature, η is the viscosity of the fluid, and D is the diffusion coefficient of the particle.[40] Therefore, DLS collects information regarding the diffusion coefficient of a particle and the Stokes-Einstein equation allows us to associate that diffusion coefficient with a particle size. The relation between the diffusion coefficient and the diameter in the Stokes-Einstein equation can easily be thought of in terms of the

effects of Brownian motion. Clearly, smaller particles will experience a greater effect of solvent molecule-particle bombardments than larger particles, and as a result larger particles will move more slowly through the solvent medium than smaller particles.

It is important to note that knowledge of the solutions viscosity and temperature are explicitly required for an accurate determination of the hydrodynamic diameter. Additionally, it should be mentioned that equation (2.8) applies specifically to spheres. So regardless of the true morphology of a particle being analyzed, it is said that the determined diffusion coefficient of the particle in question is the same as that of a sphere with that specific diameter.[40] There are other light scattering methods that can be used to determine a particles radius of gyration and morphology, but these methods are not discussed here.[39,40]

As mentioned, fluctuations in the intensity of scattered light from particles in motion provide information on the particles rate of movement. More specifically, modern DLS instruments utilize a correlator which generates the time autocorrelation function from comparisons of scattered light intensity over certain time scales, as shown in equation (2.9) below.[40]

$$G^{(2)}(\tau) =< I(t) * I(t+\tau) > \tag{2.9}$$

In this equation, $G^{(2)}$ is defined as the time autocorrelation function and is equal to the average product of scattered light intensity (I) at some arbitrary time (t) and the scattered light intensity at some later delay time τ.[40] For non-interacting homogenous spherical particles the Siegert relation can be applied and the autocorrelation function can be related to the normalized first order scattered electric field time autocorrelation function $g_1^2(\tau)$ by equation (2.z).[39,40]

$$G^{(2)}(\tau) = A + Bg_1^2(\tau) \tag{2.10}$$

The constant A is proportional to the square of the time-averaged intensity and the constant B is specific to the instrument and is generally referred to as the intercept of the correlation function.[42] In most cases non-interacting monodisperse spherical particles will possess a field autocorrelation function that can be expressed as an exponentially decaying function, as shown below.[40,42]

$$g_1(\tau) = e^{-\Gamma\tau} \tag{2.11}$$

Here again τ is the correlation delay time and Γ is defined as the decay rate and has been shown to be directly related to the translational diffusion coefficient in the following manner. [39,40,42]

$$\Gamma = D * q^2 \tag{2.12}$$

Again, D is the translational diffusion coefficient and q is known as the scattering wave vector (the difference between the incident and scattered wave vectors) and is defined by instrumental setup parameters in the following manner.[39,40,42]

$$q = \frac{4\pi n}{\lambda}\sin(\frac{\theta}{2}) \tag{2.13}$$

In this equation, n is the refractive index of the suspension fluid, λ is the wavelength of the monochromatic laser, and θ is the scattering angle of the detector.[42]

By combining equations (2.9) through (2.12) the translational diffusion coefficient can be directly related to the time autocorrelation function.

$$G^{(2)}(\tau) = A + Be^{-(2*D*q^2\tau)} \tag{2.14}$$

Through this equation, the outputted autocorrelation function value (derived from the scattering light intensity autocorrelation) can then be related to the diameter through the Stokes-Einstein equation.

The equation described in equation 2.14 is for non-interacting monodisperse systems. In practice, most systems are actually somewhat polydisperse with a

distribution of sizes that are a result of natural conformational variations of assembly processes or imperfections in synthesis procedures.[43] Therefore in polydisperse particle solutions we can view a set of particles of type i as having corresponding diffusion coefficient D_i, and therefore a corresponding decay rate Γ_i, as given by equation 2.12.[40] Each diffusion coefficient and decay rate of particle type i contributes its own exponential to the first order autocorrelation function such that equation 2.11 becomes a summation of exponentials as seen in equation 2.15 below.[40]

$$g_1(\tau) = \sum_i A_i e^{-\Gamma_i \tau} \tag{2.15}$$

From equation 2.15 a number of different algorithms can be applied to determine various distributions of size diameters. Probably the most recognized method is that of the method of Cumulants.[40,42] In this method the exponentials in equation 2.15 are expanded into a polynomial in delay time in which the expansion is usually truncated at the second order term as shown in equation 2.16 below.[40]

$$\ln(g_1(\tau)) = -K_1\tau + (\tfrac{1}{2})K_2\tau^2 \tag{2.16}$$

The K terms in equation 2.16 are known as cumulants, with $K_1 = \langle(\Gamma)\rangle$ and the second cumulant K_2 being equal to the reciprocal relaxation time around and average value.[40] The cumulants analysis is a common enough method that most DLS instrumentation perform the analysis automatically. The average diameter outputted by the method is commonly referred to as the harmonic average of the z-average diameter.[43]

Other algorithms exist to output other types of distributions such as the intensity, volume, and number average distributions.[43] It is important to note that every average diameter and every distribution is technically valid, but can be said to be different interpretations of the data.[43] For instance, the number average provides

size averages on the basis of the number of particles, whereas the intensity average provides averages based on the scattering ability of particles. In general d(intensity) > d(volume) > d(number). This is because the Rayleigh approximation tells us that the intensity of scattered light is proportional to diameter of the particle to the sixth power ($I \propto d^6$).[43] Furthermore, because of this relationship, the conversion of intensity averages to number averages is highly subject to error.[43] This does not necessarily preclude the use of the number averages because high quality intensity will be less subject to such errors. Lastly, the number average can be important because of its comparison to electron microscopy sizing distributions since these distributions are also number average distributions.[44]

2.3.3.2 DLS procedures

A Malvern Zetasizer Nano ZS instrument (Malvern Instruments, Worcestershire, United Kingdom) was utilized for all dynamic light scattering measurements. Sample preparation proceeds in the following manner. Approximately 1 mg of ELP-CLP conjugate is weighed into a 3 mL scintillation vial. A single milliliter of HPLC grade water is also added to the vial, but does not necessarily dissolve the ELP-CLP sample. No mixing is applied to the sample because dissolution will occur through heating. The now 1mg/mL ELP-CLP conjugate in water is then capped, parafilmed, and placed inside an 80°C forced convection oven. One milliliter syringes, needles, and 0.2μm PVDF (13 mm diameter) filters, and 3mL scintillation vial filled with HPLC grade water were also placed in the oven at this time. The sample and the items listed are allowed to incubate in the oven for approximately two or two and half hours.

During this time, a Malvern PCAS115 10mmx10mm cuvette (Malvern Instruments, Worcestershire, United Kingdom) was rinsed, and filled with 1mL of 0.2 μm filtered water and tested for cleanliness by performing DLS analysis of the 'blank' water solution. Cleanliness is verified by the extremely low count rates reported by the instrument. Prior to the completion of the 2 hour incubation period, this water filled cuvette is heated up to 80°C within the instrument. After the two hour incubation has passed, the hot cuvette is removed, its contents are discarded, and the cuvette is placed in the oven where the ELP-CLP sample has been incubating.

Performing all work within the oven itself, a syringe and needle is filled with the hot 'blank' water that had previously been incubated, and the water is used to flush the hot 0.2μm filter that had been incubating. The same syringe and needle is then used to aspirate the now fully dissolved ELP-CLP 1mg/mL solution and filtered (using the previously flushed filter) directly into the warm DLS cuvette. The cuvette is immediately capped, parafilmed, and the edges are wiped down with ethanol. The cuvette is then transferred to DLS instrument cuvette holder which is still set to the 80°C temperature setting.

The particles are formed within this cuvette as the DLS cooling experiment proceeds. The optical parameters for this cooling experiment are as follows. The instrument utilizes a He-Ne red laser with a wavelength of 633nm. The instrument was allowed to automatically adjust attenuation but a fixed measurement position of 4.65mm was utilized. The scattering angle for all experiments was 173°. The viscosity of water was pre-programmed into the instrument and was adjusted with temperatures accordingly. Every temperature change that was conducted by the instrument was followed with a five minute equilibration time. Three separate size measurements

were performed at every temperature and every one of those measurements utilized twenty sub runs that had a total duration of 10 seconds for each sub run.

The continuous size analysis measurements were performed with the same optical parameters as those described above. The temperature for these experiments was always maintained at 25°C. For the continuous analysis experiment, the number of measurements performed were between 100 and 200 measurements at a time with 20 sub runs for each measurement and 10 second durations were used for each sub run. In this way each measurement correspond to approximately 200 seconds of time which allowed for the diameter to be determined over time. The attenuation and measurement position remained fixed for these experiments at 6 and 4.65mm, respectively.

The analysis of diameter and count rate as the sample was heated over time was performed using the same optical parameters as those described in the cooling experiment and each measurement was performed three times with 20 sub runs with each measurement for a ten second duration. In this heating experiment, the instrument was programmed to automatically increase the temperature of the sample by 5°C after the three measurements were performed at the previous temperature. After changing the temperature, the instrument was programmed to equilibrate the sample for five minutes before proceeding with further measurements. Throughout the heating experiment both the attenuation and the measurement position were allowed to automatically be adjusted by the instrument to obtain an idealized count rate within the 200-500 kcps range.

2.3.4 Transmission electron microscopy (TEM)

2.3.4.1 Brief background

A large body of work has been developed over the past century regarding first the discovery and now the application of electrons for various purposes. In the early 1920s it was observed that electrons could form diffraction patterns.[45] Since that time electrostatic or magnetic lenses have been used to focus electron beams with high voltages.[45] In transmission electron microscopy (TEM) such a beam is used to transmit through a specimen sample and create an image on a fluorescent screen or camera.[45] The image that is created is a result of the varying density or opacity of a sample and can depend on the samples ability to transmit electrons.[45] Materials with larger atomic masses such as tungsten and uranium are typically more optically opaque for electron transmission and therefore these elements and their salts are useful for their staining properties.[46] The use of electron microscopy methods such as TEM provide significantly enhanced small scale resolution in comparison to photons due to small de Broglie wavelength of electrons.[45] The use of electron microscopy for nanoparticle morphological characterization is commonplace in many scientific fields.[43]

2.3.4.2 Procedures

Prior to grid spotting nanoparticles were first verified by DLS characterization. All TEM analyses were performed on a Zeiss Libra 120 transmission electron microscope (Zeiss, Oberkochen, Germany). 300 mesh size standard carbon coated copper grids were purchased from Electron Microscopy Sciences (Electron Microscopy Sciences, Hatfield, PA, United States). Prior to grid spotting, all grids were ionized using a PELCO easiGlow™ glow discharge unit (Ted Pella Inc. Redding, CA, United States).

For room temperature analyses, two wells of a micro well plate were filled with 17μL of a 1mg/mL nanoparticle solution and either a 17μL 1wt% phosphotungstic acid solution in water (pH 7) or a 17μL 2wt% uranyl acetate solution in water (pH approximately 4.5) separately (stain and nanoparticle solution were not mixed together). Copper grids were then soaked first in the nanoparticle solution for approximately 10 seconds and were then subsequently immersed in one of the staining solutions for 5 seconds. After removal from the staining solution the grid was blotted dry using Whatman filter paper (Sigma-Aldrich, Inc., St. Louis, Missouri, United States). The grid was then promptly inserted into the microscope and analyzed.

For the 50°C spotting, the same spotting procedures were followed as the room temperature spotting but with the following exceptions. The well plate was initially filled with sample and stain volumes and then inserted into a pre-warmed convection oven previously set to 50°C and were allowed to incubate for half an hour. Grids, filter paper, and tweezers were also incubated in the oven during this time. Grid spotting was performed directly in the oven. The sample concentration initially plated in the well plate was 1mg/mL but this value likely increased due to some solvent evaporation.

For the 4°C spotting, the same spotting protocols as the room temperature spotting were followed but with the following exceptions. All stains, grids, tweezers, and well plates were incubated in a 4°C cold room for one hour prior to grid spotting. The ELP-CLP conjugate sample (1mg/mL) was immersed in a 4^{o}C ice bath (with the ice bath itself being in the cold room) for half an hour prior to grid spotting.

The author would like to specially acknowledge and thank Shannon Modla for her experience and assistance with these procedures and studies.

2.4 Cell Viability and Uptake Procedures

2.4.1 Cell viability procedures

The viability of NIH-3T3 murine embryonic fibroblast cells was assessed after incubation with ELP-CLP nanoparticles. NIH-3T3 (American Type Culture Collection, Manassas, VA, United States) cells were plated into 12-well Corning Cellgro (Corning Mediatech Inc, Manassas, VA, Unite States) tissue culture plates at a density of 10000 cells/cm^2 (working volume 1mL) in Dulbecco's Modified Eagle's Media (DMEM) supplemented with 10% v/v fetal bovine serum (FBS) and 1% v/v penicillin streptomyscin ((PS) Thermo Fisher Scientific, Fairlawn, NJ, United States) and were allowed to grow for 24 hours. After 24 hours a stock solution of 2mg/mL ELP-CLP conjugate was prepared in non-supplemented DMEM and was heated to 80°C for 15 minutes. After this time, the ELP-CLP conjugate solution was allowed to cool to 37°C and form nanoparticles. Aliquots of this stock solution were then diluted down to their desired final concentrations (such as 1000 μg/mL) using concentrated DMEM media that had a final concentration after dilution of FBS 10% v/v and PS 1%v/v. The existing media on the cells was then removed and the cells were washed twice with Dulbecco's Phosphate Buffered Saline ((DPBS) Thermo Fisher Scientific, Fairlawn, NJ, United States) and then treated with the particle containing supplemented media and allowed to incubate for another 24 hours. Additionally, a separate well of cells was treated with fully supplemented media containing 1 mg/mL Cu(I) acetate (Sigma-Aldrich, St. Louis, MO, United States) as a negative control to the particles.

After the particle incubation period, the media was removed and the cells were again washed with DPBS and then subsequently stained using non-supplemented

DMEM containing 1.0 μg/mL propidium iodide ($\lambda_{ex} \approx 535$nm) and 2.5 μg/mL calcein AM ($\lambda_{ex} \approx 495$ nm) for 45 minutes at 37°C (calcein AM and propidium iodide from Thermo Fisher Scientific, Fairlawn, NJ, United States). The cells were then imaged using a Leica DMI-6000B fluorescence microscope (Leica microsystems, Buffalo Grove, IL, United States) with a 10x objective magnification. The entire process is illustrated in Figure 2.11 below.

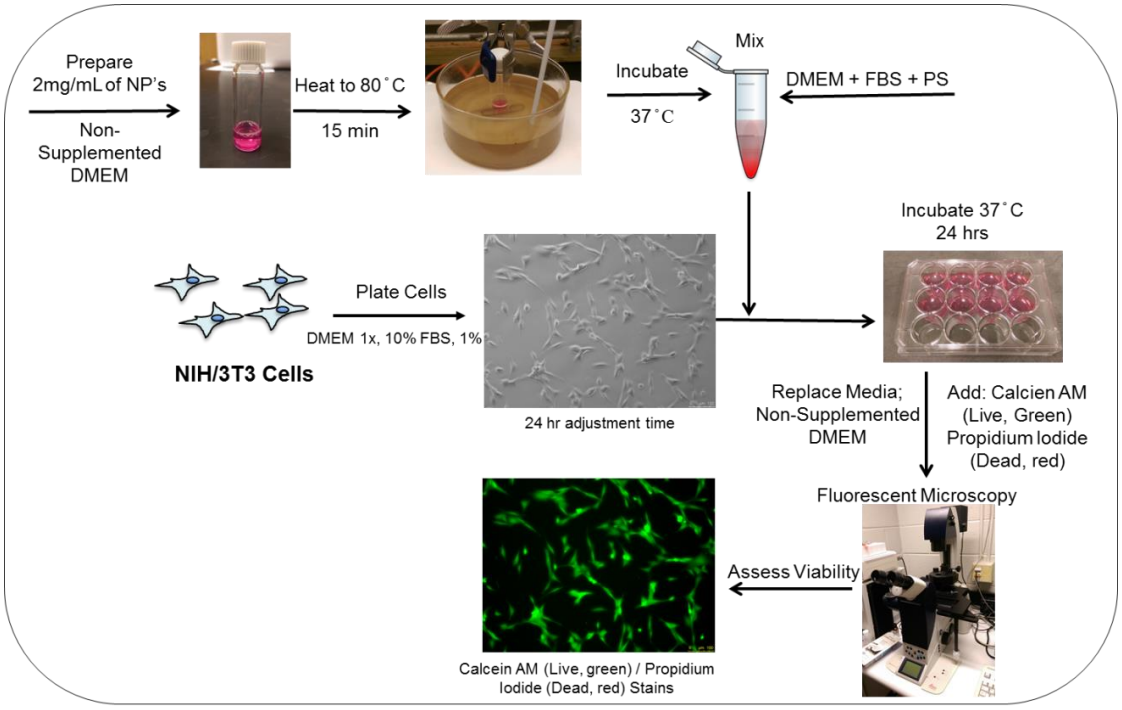

Figure 2.11: Procedural schematic for assessing NIH-3T3 cell viability of ELP-CLP nanoparticles.

2.4.2 Cell uptake procedures: fluorescence microscopy

For cell culture plate preparation, stock 6mg/mL Nutragen® collagen type I (Advanced BioMatrix, Carlsbad, CA, Unite States) was diluted to 5mg/mL in 0.2μm

filtered 30mM acetic acid in Bipoure® water (filters, acetic acid and water from Thermo Fisher Scientific, Fairlawn, NJ, United States). The diluted collagen solution was then plated (250μL) into Nunc™ 155409Lab-Tek® II chambered coverglass 8-well plates. The wells of the plate were allowed to dry out in a biosafety cabinet for four hours with the lid removed. After that time the plates were rinsed with 200 μL of DPBS two times followed by two washes with 200 μL of Biopure® water. NIH-3T3 cells were then plated into these wells at a density of 8000 cells/cm^2 with fully supplemented DMEM (10%v/v FBS and 1% v/v PS) and incubated for 24 hours at 37°C.

Prior to nanoparticle incubation with cells, nanoparticles were prepared in the same manner as the cell viability study. Briefly, a stock solution of 2mg/mL of FELP-CLP nanoparticles in non-supplemented DMEM was heated to 80°C for 15 minutes and then subsequently cooled to 37°C to elicit nanoparticle formation. Just before loading of nanoparticles to cell, this stock nanoparticle solution was diluted to 1mg/mL using fresh preheated (37°C) non-supplemented DMEM. For nanoparticle incubation with cells, 250μL of the 1mg/mL fluorescent nanoparticle non-supplemented DMEM solution was added to each cell containing well of the eight well plate. The particles were allowed to incubate with the cells for four hours at 37°C. Non-supplemented media was used for the incubation because serum starved cells are known to show enhanced uptake.

After incubation with nanoparticles for four hours, the nanoparticle serum free media was removed and replaced with fully supplemented DMEM and the cells were allowed to recover for 16 hours. After this time the supplemented media was removed and two washes with 200μL of DPBS were performed. The cells were then fixed by

adding 200μL of 4% v/v paraformaldehyde in water to each well and then incubating at room temperature with gentle shaking for 15 minutes. After this time the paraformaldehyde solution was removed and each well was washed with 200 μL DPBS two times. The well plate was subsequently stored at 4°C in DPBS until staining and imaging could be performed.

For cell nucleus staining, a stock solution of 10mg/mL Hoechst 33258 was diluted to 2 μg/mL in DPBS and added to the previously fixed cells and was allowed to incubate at room temperature for 10 minutes. After this time the stained and fixed cells were rinsed with 200 μL of DPBS. The cells were then imaged with a Leica DMI-6000B fluorescence microscope. The entire protocol is illustrated in Figure 2.12 below.

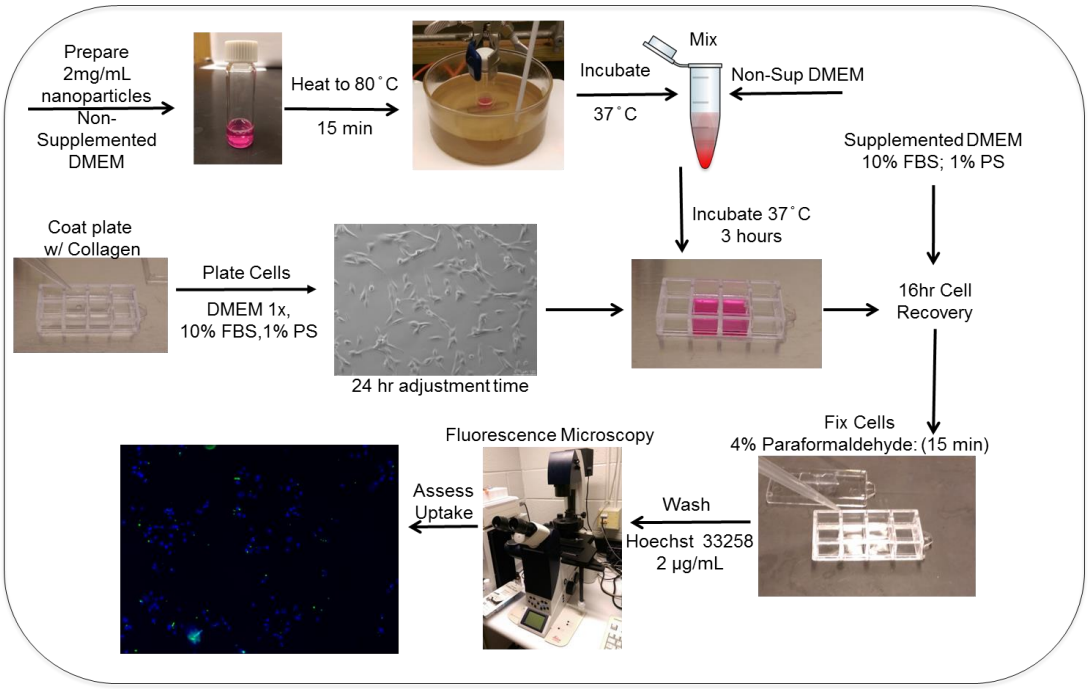

Figure 2.12: Procedural schematic for assessing FELP-CLP nanoparticle uptake into NIH-3T3 fibroblast cells by fluorescence microscopy and flow cytometry.

2.4.3 Cell uptake procedures: flow cytometry

Despite the qualitative success of the cellular uptake of the FELP-CLP nanoparticles as shown in Figure 1.8, a more quantitative assessment was desired to verify the results. Furthermore, there was also the possibility that the particles in Figure 1.8 are not necessarily internalized, but could be residing on top of the cell instead. If this were the case then the particles would have the appearance of being within the cytosol even though they are not.

Flow cytometry is a technique in which non-adhered cells are sent as a stream of fluid to multiple optical systems that detect the forward and back scattering of cellular particles as well as any fluorescent moieties that the cell may possess. Using

this technique the number of cells that contain internalized fluorescent nanoparticles can be precisely detected.

The work leading up to flow cytometry is similar to that seen in Figure 2.12. For preparation of flow cytometry however, more cells are needed for a significant number of 'events' to be analyzed by the flow cytometer detector. Therefore a 6-well Corning Cellgro (Corning Mediatech Inc, Manassas, VA, Unite States) tissue culture plate was used for plating cells at a density of 10,000 cells/cm^2. The nanoparticle formation, nanoparticle incubation time and media, and the recovery period were all identical to Figure 2.12.

However, after the 16 hour recovery period, the cells were washed with 2mL of DPBS and trypsinized with 400μL of trypsin (Thermo Fisher Scientific, Fairlawn, NJ, United States) for three to four minutes. After the trypsinization process, 600μL of fully supplemented DMEM was added to the wells to neutralize any remaining trypsin. The unadhered cells in each were then transferred to separate 15mL conical centrifuge tubes and spun at 800 rpm for three minutes using a Beckman Coulter Allegra X-22R centrifuge (Beckman Coulter, Indianapolis, IN, United States). The supernatant in each centrifuge was entirely removed leaving only the cell pellet behind. The cell pellet in each centrifuge was subsequently resuspended with approximately 300μL of cold DPBS. The suspended cells were then dispensed into a tube capped with a mesh strainer in order to remove any bulk particulate matter that would clog the flow cytometer instrument. The tubes were then put in an ice bath until analysis could begin with the cytometer. For each set of cells that were analyzed, 10,000 events were collected prior to discontinuing the run.

REFERENCES

1. Merrifield, R. B., SOLID PHASE PEPTIDE SYNTHESIS .1. SYNTHESIS OF A TETRAPEPTIDE. Journal of the American Chemical Society 1963, 85 (14), 2149-&.

2. Amblard, M.; Fehrentz, J. A.; Martinez, J.; Subra, G., Methods and Protocols of modern solid phase peptide synthesis. Molecular Biotechnology. 2006, 33 (3), 239-254.

3. Barany, G.; Kneibcordonier, N.; Mullen, D. G., SOLID-PHASE PEPTIDE-SYNTHESIS - A SILVER ANNIVERSARY REPORT. International Journal of Peptide and Protein Research. 1987, 30 (6), 705-739.

4. Chan, W.C.; White, P.D., *Fmoc solid phase peptide synthesis: a practical approach*; Oxford University Press: New York, 2004.

5. Montalbetti, C.A.G.N.; Falque, V., Amide bond formation and peptide coupling. Tetrahedron. 2005, 61, 10827-10852.

6. Valeur, E.; Bradley., Amide bond formation: beyond the myth of coupling reagents. Chem. Soc. Rev. 2009, 38, 606-631.

7. Vlieghe, P.; Lisowski, V.; Martinez, J.; Khrestchatisky, M., Synthetic therapeutic peptides: science and market. Drug Discovery Today. 2010, 15(1-2), 40-56.

8. Clement, H.; Flores, V.; Diego-Garcia, E.; Corrales-Garcia, L.; Villegas, E.; Corzo, G., A comparison between the recombinant expression and chemical synthesis of a short cysteine-rich insecticidal spider peptide. Journal of Venomous Animals and Toxins including Tropical Diseases. 2015, 21:19. 1-10.

9. Meyer, D.; Chilkoti, A., Purification of recombinant proteins by fusion with thermally-responsive polypeptides. Nature Biotechnology. 1999, 17, 1112-1115.

10. Shi, J.; Ma, X.; Gao, Y.; Fan, D.; Zhu, C.; Mi, Y.; Xue, W., Hydroxylation of human type (III) collagen alpha chain by recombinant coexpression with a viral prolyl 4-hydroxylase in *Escherichia coli*. The Protein Journal. 2017, 36(4), 322-331.

11. Rutschmann, C.; Baumann, S.; Cabalzar, J.; Luther, K.; Hennet, T., Recombinant expression of hydroxylated human collagen in *Escherichia coli*. Applied Microbiology and Biotechnology. 2014, 98(10), 4445-4455.

12. Wang, T.; Lew, J.; Premkumar, J.; Poh, C.L.; Naing, M.W., Production of recombinant collagen: state of the art and challenges. Engineering Biology. 2017, 1(1), 18-23.

13. McNaught, A.D.; Wilkinson, A.; *Compendium of Chemical Terminology*; the "Gold Book" 2nd ed. [Online]; Nic, M.; Jirat, J.; Kosata, B., Eds.; Jenkins, A., Updates.; Blackwell Scientific Publications: Oxford, 2006.

14. Cazes, J.; Scott, R.P.W., *Chromatography theory*; Marcel Dekker: New York, 2002

15. Brown, P.R.; Hartwick, R.A., *High performance liquid chromatography*; Wiley: New York, 1989

16. Hamilton, R.J.; Sewell, P.A., *Introduction to high performance liquid chromatography* 2nd ed.; Chapman and Hall: London, New York, 1982.

17. LC-GC's CHROMacademy. The theory of HPLC – Reverse phase chromatography – e-learning module. http://www.chromacademy.com /index.html (accessed Aug 23, 2017).

18. Wypych, G., *Handbook of solvents*. William Andrew Pub: Toronto, Norwich, 2001.

19. Kolb, H. C.; Finn, M. G.; Sharpless, K. B., Click chemistry: Diverse chemical function from a few good reactions. Angewandte Chemie-International Edition 2001, 40 (11), 2004-+.

20. Presolski, S. I.; Hong, V. P.; Finn, M. G., Copper-Catalyzed Azide-Alkyne Click Chemistry for Bioconjugation. Current protocols in chemical biology 2011, 3 (4), 153-162.

21. Moses, J. E.; Moorhouse, A. D., The growing applications of click chemistry. Chemical Society Reviews 2007, 36 (8), 1249-1262.

22. Luo, T. Z.; Kiick, K. L., Noncovalent Modulation of the Inverse Temperature Transition and Self-Assembly of Elastin-b-Collagen-like Peptide Bioconjugates. Journal of the American Chemical Society 2015, 137 (49), 15362-15365.

23. Grieshaber, S. E.; Paik, B. A.; Bai, S.; Kiick, K. L.; Jia, X. Q., Nanoparticle formation from hybrid, multiblock copolymers of poly(acrylic acid) and a VPGVG peptide. Soft Matter 2013, 9 (5), 1589-1599.

24. Presolski, S. I.; Hong, V.; Cho, S. H.; Finn, M. G., Tailored Ligand Acceleration of the Cu-Catalyzed Azide-Alkyne Cycloaddition Reaction: Practical and Mechanistic Implications. Journal of the American Chemical Society 2010, 132 (41), 14570-14576.

25. Meldal, M.; Tornoe, C. W., Cu-catalyzed azide-alkyne cycloaddition. Chemical Reviews 2008, 108 (8), 2952-3015.

26. Haldon, E.; Nicasio, M. C.; Perez, P. J., Copper-catalysed azide-alkyne cycloadditions (CuAAC): an update. Organic & Biomolecular Chemistry 2015, 13 (37), 9528-9550.

27. Lonsdale, D. E.; Bell, C. A.; Monteiro, M. J., Strategy for Rapid and High-Purity Monocyclic Polymers by CuAAC "Click" Reactions. Macromolecules 2010, 43 (7), 3331-3339.

28. Leophairatana, P.; Samanta, S.; De Silva, C. C.; Koberstein, J. T., Preventing Alkyne-Alkyne (i.e., Glaser) Coupling Associated with the ATRP Synthesis of Alkyne-Functional Polymers/Macromonomers and for Alkynes under Click (i.e., CuAAC) Reaction Conditions. Journal of the American Chemical Society 2017, 139 (10), 3756-3766.

29. Lambert, J.B.; Shurvell, H.F.; Lightner, D.A.; Cooks, R.G., Electronic Absorption and Chiroptical Spectroscopy. In *Organic Structural Spectroscopy*; Prentice-Hall: New Jersey, 1998.

30. Brown, T.E.; LeMay, H.E.; Bursten,B.E.; Murphy, C.; Woodward, P., *Chemistry: The Central Science*, 12th ed; Prentice-Hall: New Jersey, 2011.

31. Urry, D. W.; Shaw, R. G.; Prasad, K. U., POLYPENTAPEPTIDE OF ELASTIN - TEMPERATURE-DEPENDENCE OF ELLIPTICITY AND CORRELATION WITH ELASTOMERIC FORCE. Biochemical and Biophysical Research Communications 1985, 130 (1), 50-57.

32. Beri, R. G.; Wayte, J. R. T.; Swift, J.; Abraham, S. J.; Brown, M. E., Application of optical density probes in turbidity measurement of batch and fed batch mammalian cell culture processes. Abstracts of Papers American Chemical Society 1998, 216 (1-3), 220.

33. Saraceno, J. F.; Shanley, J. B.; Downing, B. D.; Pellerin, B. A., Clearing the waters: Evaluating the need for site-specific field fluorescence corrections based on turbidity measurements. Limnology and Oceanography-Methods 2017, 15 (4), 408-416.

34. Woody, R,. Theory of Circular Dichroism of Proteins; Fasman, G.D., Ed.; Plenum Press: New York, 1996. p 25-69.

35. Johnson, W.C., Circular Dichroism Spectroscopy and the Vacuum Ultraviolet Region. Annual Review of Physical Chemistry 1978, 29, 93-114.

36. Johnson, W. C., Analyzing protein circular dichroism spectra for accurate secondary structures. Proteins-Structure Function and Genetics 1999**,** *35* (3), 307-312.

37. Provder, T. PARTICLE SIZING AND CHARACTERIZATION. Particle Sizing and Characterization. American Chemical Society. 2004, Washington D.C. pg. 881.

38. Doob, J. L., The Brownian movement and stochastic equations. Annals of Mathematics 1942, 43, 351-369.

39. Finsy, R., PARTICLE SIZING BY QUASI-ELASTIC LIGHT-SCATTERING. Advances in Colloid and Interface Science 1994, 52, 79-143.

40. Pecora, R., Dynamic light scattering measurement of nanometer particles in liquids. Journal of Nanoparticle Research 2000, 2 (2), 123-131.

41. Einstein, A., The motion of elements suspended in static liquids as claimed in the molecular kinetic theory of heat. Annalen Der Physik 1905, 17 (8), 549-560.

42. ISO 24412:2017(E). Particle size analysis- Dynamic light scattering (DLS). International Organization for Standardization. http://www.iso.org/

43. Hackley, V. A.; Clogston, J. D., Measuring the Hydrodynamic Size of Nanoparticles in Aqueous Media Using Batch-Mode Dynamic Light Scattering. In Characterization of Nanoparticles Intended for Drug Delivery, McNeil, S. E., Ed. Humana Press Inc: Totowa, 2011; Vol. 697, pp 35-52.

44. Domingos, R. F.; Baalousha, M. A.; Ju-Nam, Y.; Reid, M. M.; Tufenkji, N.; Lead, J. R.; Leppard, G. G.; Wilkinson, K. J., Characterizing Manufactured Nanoparticles in the Environment: Multimethod Determination of Particle Sizes. Environmental Science & Technology 2009, 43 (19), 7277-7284.

45. Egerton, R.F., *Physical Principles of Electron Microscopy: An Introduction to TEM, SEM, and AEM* 2nd ed. Spring International Publishing: Switzerland, 2006.

46. Hayat, M.A., *Electron Microscopy: Biological Applications*. 3rd ed. CRC Press Inc: Boca Raton, Florida, 1989.

Chapter 3

RESULTS AND DISCUSSION

In this chapter the properties of ELP and CLP peptides and some of their resulting conjugates will be presented and discussed. Section 3.1 will provide a brief introduction to the peptides that were designed and the hypothesized outcomes of their potential conjugates and particles. The characterization of CLPs with regard to their triple helix formation and melting temperatures as well as the transition temperatures of ELPs will be highlighted in section 3.2. In section 3.3, the confirmation of conjugate products will be briefly discussed and as well as their secondary structure characterization. Lastly, section 3.4 will highlight the propensity of these conjugate systems to form nanoparticles and information regarding particles stability, thermal characteristics, and morphology will be discussed.

3.1 Introduction

As was discussed in section 1.5.3, the original ELP-CLP nanoparticle system lacks the thermal properties that impart the nanoparticle with the desired characteristics for drug delivery to degraded collagen protein. These desired thermal properties include an ELP domain that has a transition temperature in the range of 25 °C $\leq T_t \leq$ 30 °C, as well as a CLP domain that has a partially unfolded triple helix (termed hybridization region) in the range of 34 °C $\leq T_t \leq$ 45 °C. In comparison to the original nanoparticle system, raising the transition temperature of the ELP domain would enable a particle to have stimuli-responsive (in this case, hyperthermic

responsive) on-demand drug release properties. Furthermore, lowering the melting temperature of the CLP domain would shift the hybridization region of the original nanoparticle system to a more physiologically relevant temperature so that the particle could innately hybridize with degraded collagen protein in the body.

In order to make a particle that possesses this design criterion, sensible modifications to the ELP and CLP peptide sequences can be made. In order to raise the lower critical solution temperature of the ELP, either the repeat length of the ELP domain can be shortened from six to some lower repeat number, or the guest residue can be made more hydrophilic (switch phenylalanine to serine or lysine).[1] To lower the melting temperature of the CLP, the repeat length n of the $(GPO)_n$ repeat unit can be lowered, or alterations to the primary sequence can also be made.[2, 3] The focus of this work is centered on modifications to the CLP domain while maintaining the length and sequence of the ELP domain. The purpose of only altering the melting temperature of the CLP domain is to more thoroughly understand the role of CLP in particle formation and to test for any possible effects that the CLP may have in regard to the ELPs transition temperature. Preliminary work has also been completed for ELP domain modifications, but is not discussed here.

In order to create an ELP-CLP nanoparticle system that is capable of collagen protein hybridization and to more effectively study CLPs role in nanoparticle formation, a small library of CLPs was generated. The sequences synthesized include azide-$(GPO)_n$GG where n=6,7,8, and a fourth sequence was made with the sequence azide-$(GPO)_3$GFOGER$(GPO)_3$GG. With the original sequence being azide-$(GPO)_4$GFOGER$(GPO)_4$GG, all of these sequences have a smaller repeat length and therefore will most likely have a lower melting temperature than the original sequence

(T_m = 50 °C).[2, 4] Furthermore, with the exception of azide-$(GPO)_3$GFOGER$(GPO)_3$GG, all of the primary sequences have been altered by removal of the GFOGER integrin binding sequence. The GFOGER repeat unit was omitted for a number of reasons. Firstly, we are chiefly interested in having this particle target degraded collagen protein so that the ECM can be used as a drug reservoir. As such, we are not presently interested in cell adhesion and uptake of these particles which would possibly be aided by the GFOGER sequence.[5] Secondly, I hypothesize that the GFOGER integrin binding sequence cannot properly function while the particle is in its assembled state. This hypothesis is based off of the crystal structure of the GFOGER-integrin binding event, which indicates that perpendicular access of the integrin to the linear CLP sequence is required for effective binding.[6] Given the significant curvature of the vesicular wall and the GFOGER sequence being buried within the wall, it is not likely that integrins can successfully bind in this perpendicular/linear manner to the GFOGER sequence. Clearly, if the function of GFOGER is lost then there is little reason to include the sequence. Perhaps future studies can be carried out to determine the bioactivity of GFOGER in the assembled state.

With that being said, the GFOGER sequence may be of interest because of its effect on the melting temperature of the triple helix. While it has been shown that phenylalanine has significant triple helical destabilization effects, the glutamic acid and arginine residues being placed in the X_{AA} and Y_{AA} positions of (G-X_{AA}-Y_{AA}) respectively have been shown to be only slightly less stable than proline and hydroxyproline in the same positions.[3, 7] Therefore, it is reasoned that the GFOGER repeat sequence will lower the melting temperature of a CLP while still contributing

two repeat lengths to the CLP. It is for this hypothesized effect of T_m that the sequence azide-$(GPO)_3$GFOGER$(GPO)_3$GG was included in the CLP library.

It is important to note that after conjugation of these CLPs to the same $(VPGFG)_6$G' (G' is propargyl glycine) ELP sequence that the volume fraction of total CLP in the conjugate will be lower for every sequence than the previous nanoparticle system that was studied ($(VPGFG)_6$-$(GPO)_3$GFOGER$(GPO)_3$GG). From block copolymer self-assembly theory, it is known that this change in CLP volume fraction could have serious implications in regards to self-assembly that may be completely unrelated to these CLPs melting temperatures.

Eisenberg *et al* have demonstrated that by shortening the length (i.e. total volume fraction) of a poly(acrylic acid) block in a diblock polystyrene-*b*-poly(acryclic acid) copolymer while maintaining the length of the polystyrene block results in a change of aggregate morphology from micellar spheres to micellar rods to vesicles as the hydrophilic poly(acrylic acid) block gets progressively shortened.[8] Jain and Bates have reported the same trend with their poly(butadiene)-*b*-poly(ethylene oxide) copolymer system, where a progressive decrease in hydrophilic poly(ethylene oxide) weight %, while maintaining the same degree of polymerization of poly(butadiene) (same repeat length), resulted in a trend from spheres to cylinders to vesicles.[9]

While these trends in block copolymer literature are incredibly important to keep in mind, the rod-like nature of the CLP domain and the coil like nature of the ELP domain contribute to ELP-CLP self-assembly in a more complex manner than the coil-*b*-coil block copolymer systems just described.[10] As a result the self-assembly of the ELP-CLP system may be more difficult to predict than simple alterations to repeat length. Further considerations of ELP-CLP self-assembly will be discussed in more

detail below. For now it is sufficient to say that there was some risk in designing CLPs that would result in conjugates with lower hydrophilic volume fractions, but because of the rod-coil nature of the ELP-CLP system, this risk was perhaps mitigated to some degree. Despite there being numerous studies regarding amino acid propensity for triple helix formation, precise prediction of melting temperatures via sequence modifications to the previous azide-$(G\text{-}X_{AA}\text{-}Y_{AA})_{10}GG$ template would have been considerably difficult.[3, 7, 11] The effect of repeat length on T_m on was far more predictable, and as a result, the generation of a CLP library of azide-$(GPO)_nGG$, with n=6,7, and 8, was the logical starting point for assessing ELP-CLP nanoparticle formation with CLPs that possess lower T_m's.

The following section discusses characterization of the CLP library that was just discussed. Characterization of the ELP domain $(VPGFG)_6G$' is also highlighted.

3.2 Peptide Characterization

3.2.1 Circular dichroism characterization of CLPs triple helical properties

3.2.1.1 Confirmation of CLPs triple helix formation

After the CLP library was generated, the first critical step in their characterization was the confirmation that the CLPs synthesized would form a triple helix and that these triple helices could be sufficiently melted out at high enough temperatures. Utilizing circular dichroism spectroscopy, the triple helix formation for each of the CLPs in the small library was confirmed following protocols discussed in section 2.3.2.2. Figure 3.1 below showcases the circular dichroism spectra of the small CLP library at both a) 4°C and at b) 80°C.

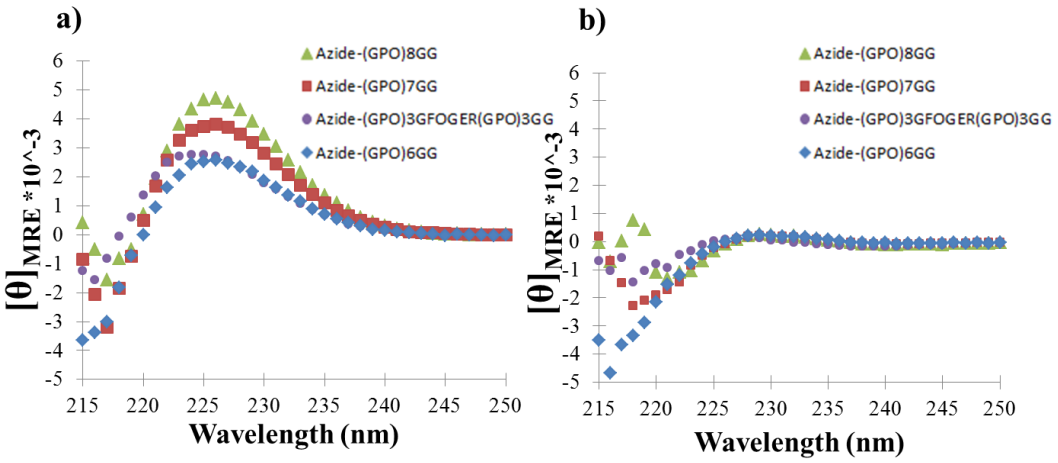

Figure 3.1: Circular dichroism spectroscopy of the small CLP library at a) 4°C and at b) 80°C. All peptides were measured in 10mM DPBS at a concentration of 0.35mM. Triple helices have a characteristic positive ellipticity maximum at 225nm.

The collagen triple helix is marked by a positive mean residue ellipticity at 225nm in a standard circular dichroism spectra output.[12] Figure 3.1a) demonstrates the ability of all the CLPs in the small library to form a triple helix at 4°C. This result is expected based on comparisons to CLPs synthesized by other groups where the shortest possible CLP with a repeat of n=6 was shown to form triple helices similar to the azide-$(GPO)_6$GG that is shown in Figure 3.1.[2] In contrast, Figure 3.1b) also shows that all of the CLPs triple helices can be unfolded upon heating to 80°C. This demonstrates that the melting temperature of all the CLPs in the library must be less than 80°C. This result was also expected given that $(GPO)_{10}$ has a melting temperature of approximately 65°C, and the fact that any CLP of the same sequence with an n lower than 10 would have a lower melting temperature.[6] Lastly, it is interesting to note that the relative intensity of the triple helical maximal ellipticity at 225nm in Figure 3.1 correlates fairly well with CLP repeat length and expected stability. Given that

every peptide was analyzed at the same concentration and that Figure 3.1 presents the data in terms of mean residue ellipticity, it is very clear that the propensity for triple helix formation of azide-$(GPO)_8$GG is greater than that observed for all of the other CLPs. Again, this result is expected since azide-$(GPO)_8$GG will have a larger melting temperature than the other CLPs due to the additional enthalpic gains provided by backbone hydrogen bonding as well as possibly additional entropic stability provided by every repeat being the idealized (GPO) repeat.

3.2.1.2 Determination of CLPs triple helical melting temperatures

After confirmation of the CLPs triple helical formation, it was then necessary to quantitatively determine each CLP's relative triple helical stability by means of characterizing their triple helical melting temperatures. The determination of the CLPs triple helical melting temperature was incredibly important since the value of the T_m would aid in choosing which CLPs should be studied for ELP-CLP conjugation. More specifically, the T_ms of each CLP are good predictors of what the triple helical melting temperature of the ELP-CLP system would be, and as a result, the T_ms would help determine the optimal hybridization region temperature range for each ELP-CLP system. As will be discussed later, the T_ms of the CLPs by themselves are only predictors because ELPs impart additional stability to ELP-CLP conjugates and as a result, the conjugates have higher triple helical melting temperatures than the CLPs by themselves.[4]

As described in section 2.3.2, the melting temperature of a CLP is found by monitoring the maximal ellipticity at 225nm as temperature is increased over time. The melting temperature itself is defined as the point where ellipticity at the 225nm wavelength changes most rapidly with respect to temperature. In this work, this point

is determined by fitting the melting curve with a Boltzmann sigmoidal function and then taking the derivative of this function with respect to temperature. The minimum of the first derivative of this curve is the point of greatest change of ellipticity over temperature and is defined as the melting temperature for that CLP.[4] There are other methods used to determine the melting temperature either by using linear interpolation or by defining the melting temperature as the point where 50% of the triple helix is in an unfolded state.[4, 13] The melting curves and their corresponding derivatives for each CLP in the small library is shown in Figure 3.2 below.

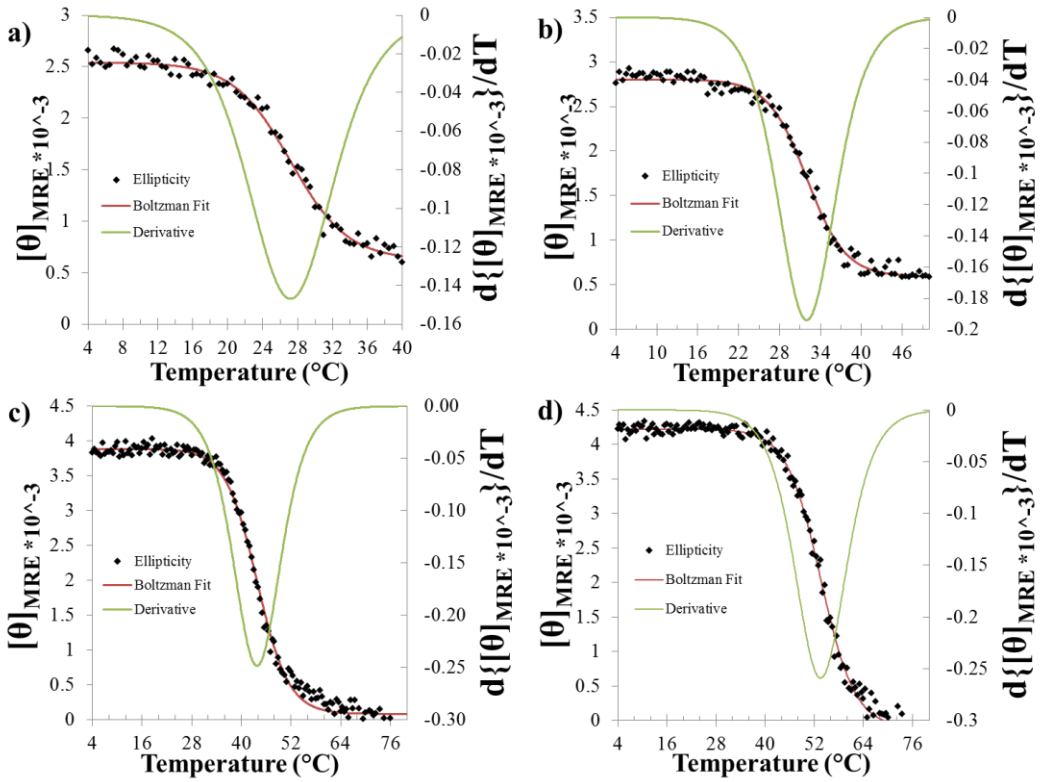

Figure 3.2: Triple helical melting curves for the small CLP library: a) azide-$(GPO)_6GG$, b) azide-$(GPO)_3GFOGER(GPO)_3GG$, c) azide-$(GPO)_7GG$, d) azide-$(GPO)_8GG$. All peptides were measured at 0.35mM in 10mM DPBS at a scanning rate of 10°C/hour at 225nm.

From Figure 3.2, the melting temperature for each CLP can be readily determined. The T_ms for azide-$(GPO)_n$GG, for n=6,7,and 8 are 27°C, 44°C, and 53°C respectively. The melting temperature for azide-$(GPO)_3$GFOGER$(GPO)_3$GG is 32°C. The increase in melting temperatures for the sequential increase in repeat length is consistent with the trends reported in literature.[2, 6] The effect of the GFOGER sequence on melting temperature is interesting.

As was hypothesized, the GFOGER sequence lowers the T_m for a CLP that is of equal repeat length, as is evident by both azide-$(GPO)_8$GG and azide-$(GPO)_3$GFOGER$(GPO)_3$GG possessing a repeat length of eight, but with a difference in melting temperature of approximately 20°C. Alternatively, the GFOGER sequence can be viewed as method to extend the repeat length of CLP without dramatically altering the melting temperature. Clearly the difference of only 5°C between azide-$(GPO)_3$GFOGER$(GPO)_3$GG and azide-$(GPO)_6$GG is quite small, and the melting temperature reported here for the GFOGER sequence is similar to a previous report.[14] Furthermore, the value of azide-$(GPO)_8$GG (T_m = 53°C) is not significantly different than the T_m previously reported from our group of the azide-$(GPO)_4$GFOGER$(GPO)_4$GG CLP (T_m = 50°C).[4] Future studies will have to more thoroughly investigate this effect, but for now it seems that the destabilization caused by the phenylalanine residue is somewhat offset by the stabilization effects of the glutamic acid and arginine residues in the following repeat.[3, 7] However, the overall destabilization effect of the GFOGER sequence is significant by comparison to a CLP with proline and hydroxyproline residues in the X_{AA} and Y_{AA} positions instead.

It is important to note that the melting temperatures reported here are not exactly the same as similar sequences in literature for a couple of important reasons.

First, the addition of the C-terminal glycines (the purpose of which is to prevent diketopiperazine formation during synthesis) as well as the N-terminal 4-azidobutanoic acid may have complicated effects on the melting temperature of these CLPs that would be somewhat different then similar CLP sequences reported in literature that do not have these moieties. Perhaps more importantly, the concentrations of CLPs used as well as the heating rate can lead to considerable differences of reported T_ms. This has been a common problem in the CLP field for some time and a true comparison of melting temperatures between CLP sequences requires consideration of these parameters which sometimes go unreported.[6, 15]

3.2.2 UV-Vis characterization of ELPs inverse transition temperature (T_t)

Just as it is necessary to confirm the triple helix forming properties of CLPs, it is equally as important to confirm the ability of ELPs to undergo an inverse phase transition to a collapsed state. It is hypothesized that this collapsed state is critical in forming the vesicular bilayer of the ELP-CLP nanoparticle system. Because the main ELP studied here is considerably short (n=6) compared to recombinant ELPs (n=40 to 200s), the transition temperature is not observable in pure water.[16] Therefore, the transition temperature of $(VPGFG)_6G$' had to be determined while dissolved in a number of different salt solutions and an extrapolation had to be performed to determine the salt-free transition temperature. While the goal is to simply confirm the transition of ELPs to their collapsed state, the determination of the transition temperature value is also valuable as a reference for the transition temperature of collapsed ELP in the nanoparticle system. The transition temperature is classically defined as the temperature at which 50% of maximal turbidity of the collapsed ELP is reached according to simple light scattering measurements.[17] Following the methods

described in section 2.3.1.2, the turbidity profiles of $(VPGFG)_6G$' in four different salt solution concentrations were generated. Figure 3.3 below illustrates these turbidity profiles as well as the extrapolation of the collected inverse transition temperatures to zero salt concentration.

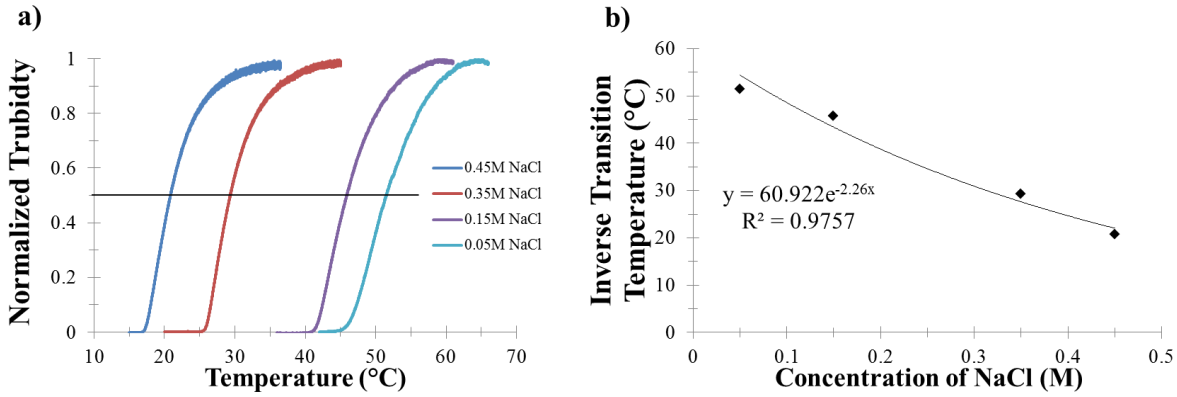

Figure 3.3: Confirmation of $(VPGFG)_6G$'s ability to go through and inverse transition collapse and phase separation: a) turbidity profiles of 0.57mg/mL $(VPGFG)_6G$' at four different salt concentrations with a heating rate of 1°C/min, b) plot of inverse transition temperature as a function of salt concentration; the data were fit with a simple exponential function in order to extrapolate to the 0M NaCl transition temperature.

From Figure 3.3a it is evident that $(VPGFG)_6G$' is able to go through an inverse transition temperature and collapse to a coacervate phase similar to larger ELPs, albeit in relatively low sodium chloride concentrations. Images of the soluble and collapsed phases can be found in Figure 1.4. The transition temperature of ELP at a NaCl concentration of 0.45M is 21°C and increases to 52°C at a NaCl concentration of 0.05M. As expected from ELP literature, the transition temperature of the ELP decreases with increasing sodium chloride concentration.[17] This is due to changes in

solvent polarity caused by the salt, which then leads to a subsequent increase in hydrophobic hydration of the hydrophobic residues.[1]

For these studies, a ELP concentration of 0.57mg/mL was chosen because this is the concentration of ELP that is present in a 1mg/mL sample of $(VPGFG)_6$-$(GPO)_7$GG ELP-CLP conjugate. Maintaining the same ELP concentration between the unconjugated and conjugated systems allows for a direct comparison of T_t values. Such a comparison will be discussed shortly.

From Figure 3.3b the transition temperatures collected from Figure 3.3a were plotted against their corresponding sodium chloride concentrations so that an extrapolation could be performed to determine the T_t at 0M NaCl. An exponential fit of the data was chosen because an exponential fit had a higher correlation for a similar T_t vs NaCl data set of a larger ELPs from ref 17 (data manually tabulated and fitted; fit not shown).[17] Utilizing this exponential fit, a T_t = 61°C was found for $(VPGFG)_6$ G' for a 0M NaCl solution.

Despite ELPs having been studied for a number of years, there is surprisingly little published literature regarding transition temperatures of short synthetic ELPs of n<10; at least to the best of our group's knowledge.[4] Furthermore, what few reports do exist are for systems with different ELP repeat lengths and primary sequences, different ELP and NaCl concentrations, and likely different heat rates that sometimes go unreported.[18] Therefore it is relatively difficult to corroborate the reported extrapolation method and value for $(VPGFG)_6$G' at 0M NaCl.

The importance in maintaining identical parameters is illustrated in supplemental Figure B.1, where similar turbidity profiles and extrapolation are performed for $(VPGFG)_5$G' but at a concentration of 1mg/mL and a heating rate of

5°C/min. While $(VPGFG)_5G'$ is indeed supposed to possess a larger T_t, it is unlikely that the difference between n=5 and n=6 is approximately 60°C. Certainly the two figures are not comparable on the basis of concentration alone, but I hypothesize the heating rate is equally as important as well.

Future work will focus on equalizing these parameters so that the two ELP systems can be properly compared. Furthermore, additional turbidity profiles can be collected for $(VPGFG)_6G'$ to obtain a more precise extrapolation to 0M NaCl. I hypothesize that 61°C is quite low compared to the true T_t for the 0M NaCl concentration. The reasoning for this is based on the fact that the transition temperature at 0 M NaCl has previously not been observed below 100°C; however this has not yet been confirmed by the methods described here (unpublished data). I suggest that the relationship between T_t and NaCl concentration becomes asymptotic as the NaCl concentration approaches 0M, similar to what is observed as the number of pentamer repeats decreases for larger ELP systems (see Figure 6 of ref 19).[19] While the determination of T_t for short synthetic ELPs is still in its infancy with regard to the field, the goal of proving the LCST transition for this system has been accomplished and shown to occur for physiologically relevant salt concentrations.[20]

3.2.3 Peptide characterization summary and conjugate selection

In the last two sections, the characterization of the properties of CLPs and ELPs that are required for ELP-CLP nanoparticle formation was described. The data confirmed the triple helix formation of CLPs as well as the transition temperature collapse of ELPs. Furthermore, the specific melting temperature of each CLP triple helix was determined as well as the current value for the $(VPGFG)_6G'$ transition temperature. These data are summarized in Table 3.1 below.

Table 3.1: Summary of triple helical melting temperatures (T_m) for CLPs as well as the current value for the transition temperature (T_t) for $(VPGFG)_6G$'. A temperature range for the T_t of $(VPGFG)_5G$' is also reported based off of the $(VPGFG)_6G$' data.

Sequence	**Tm (°C)**	**LCST (°C) [0M NaCl]**
Azide-$(GPO)_8GG$	53	N/A
Azide-$(GPO)_7GG$	44	N/A
Azide-$(GPO)_6GG$	27	N/A
Azide-$(GPO)_3GFOGER(GPO)_3GG$	32	N/A
$(VPGFG)_6$-Alkyne	N/A	61
$(VPGFG)_5$-Alkyne	N/A	$61< T_t <125$

From Table 3.1 we can make some hypotheses regarding which ELP-CLP systems that can be studied. First it is important to make the following considerations. As was discussed in section 3.1, every CLP that is conjugated to $(VPGFG)_6G$' will have a total CLP volume fraction that is less than the previous system. For the present discussion this change in volume fraction will be disregarded as predictions are not so easily made. A discussion regarding the volume fraction change will be had shortly. Furthermore, the present study is primarily focused on the use of $(VPGFG)_6G$' only (see section 3.1). Unless otherwise noted, the term 'ELP' will henceforth be used synonymously with the $(VPGFG)_6G$' sequence. Lastly, it is important to consider again that the melting temperatures reported in Table 3.1will likely increase upon ELP conjugation due to an ELP stabilization effect that was reported in the initial nanoparticle system.[4]

On the basis of melting temperatures alone we can predict that the use of azide-$(GPO)_8GG$ in an ELP-CLP system would likely have a physiologically irrelevant hybridization region similar to that shown in Figure 1.6. The hypothesized ideal hybridization region is between 34°C and 45°C (Table 1.2). With this range in

mind it is suggested that either azide-$(GPO)_3$GFOGER$(GPO)_3$GG or azide-$(GPO)_6$GG conjugated to ELP would yield a conjugate that has a triple helical melting temperature within the idealized hybridization range due to the ELPs extra stability imparting the conjugate with slightly higher T_ms than those in Table 3.1. Unfortunately, at the time this work was completed the $(VPGFG)_6$-$(GPO)_3$GFOGER$(GPO)_3$GG system had not been fully purified for analysis and is only discussed later in regards to future work. However, the $(VPGFG)_6$-$(GPO)_6$GG conjugate has been investigated and is discussed below. Additionally, $(VPGFG)_6$-$(GPO)_7$GG was also studied as a means to directly determine the impact of repeat length and melting temperature on nanoparticle formation by comparison to the $(VPGFG)_6$-$(GPO)_6$GG system.

3.3 Conjugate Characterization

3.3.1 Confirmation of conjugate product

The $(VPGFG)_6$-$(GPO)_7$GG and $(VPGFG)_6$-$(GPO)_6$GG conjugates were synthesized and purified as was described in chapter 2. The pure ELP-CLP conjugates can be characterized by a number of methods including ^{1}H-nuclear magnetic resonance spectroscopy, Fourier transform infrared spectroscopy, and trifluoroethanol gel permeation chromatography. As highlighted in section 2.2.2, reported here for the first time is the successful characterization of these ELP-CLP conjugates with high performance liquid chromatography and electrospray ionization mass spectrometry. Through electrospray ionization mass spectrometry analysis, Figure 2.9b confirms the expected product of $(VPGFG)_6$-$(GPO)_7$GG (see section 2.2.2) and Figure B.2 confirms the expected product of $(VPGFG)_6$-$(GPO)_6$GG after RP-HPLC purification (see

appendix B). These products masses are exactly confirmed and the lack of other significant ion peaks indicates that the conjugate samples are fairly pure. Although the masses indicate the high probability that the desired product was indeed made, it is best to verify the conjugation reaction by additional methods. Unfortunately, due to the low yields of these products, NMR spectroscopy could not be performed because large quantities of material are required for the analysis. However, an example of ^{1}H-NMR verification of these conjugates, Figure B.3shows the NMR spectra of $(VPGFG)_5G'$,$(GPO)_8GG$, and $(VPGFG)_5$-$(GPO)_8GG$. Specifically, ^{1}H-NMR can be used to show the consumption of the terminal alkyne proton (as well as modified chemical shift of nearby protons) of ELPs after the CuAAC conjugation has taken place.

3.3.1.1 Attenuated total reflectance Fourier transform infrared spectroscopy (ATR FT-IR)

In contrast to NMR spectroscopy, ATR FT-IR spectroscopy can be performed with very low quantities of material. A complete background of ATR FT-IR spectroscopy is beyond the scope of the present discussion, but it is generally used to associate infrared spectra of a compound to specific chemical functionalities with known frequencies.[21] For instance, the alkyne functionality of ELP can be detected from ATR FT-IR by analysis of ELPs spectra and by verifying the frequency band where the alkyne functionality would usually be present.[21] However, the alkyne functional group typically has a fairly weak intensity and so it would be better to analyze the azide functionality of CLP instead which is known to have a strong and salient frequency.[21] By comparing the presence of the azide functionality in CLPs and the lack of azide functionality in ELP-CLPs, it can be said that the azide was

consumed by the CuAAC reaction and that the conjugation reaction was successful. The azide band in infrared spectroscopy appears at the 2160 and 2080 cm^{-1} frequency and appears strongly in IR spectra.[21] Figure 3.4 below shows the IR spectra for $(VPGFG)_6$-$(GPO)_6GG$ and $(VPGFG)_6$-$(GPO)_7GG$ and each of the individual peptides for each conjugate.

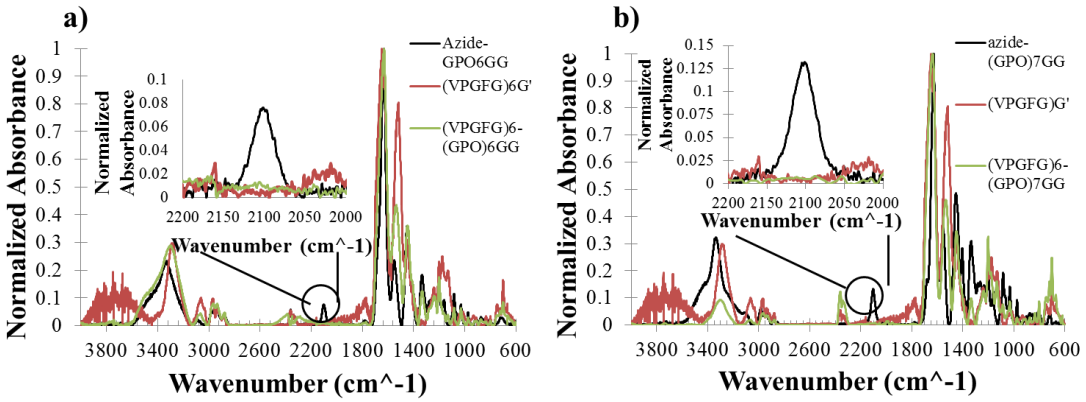

Figure 3.4: ATR FT-IR absorbance spectra for a) the $(VPGFG)_6$-$(GPO)_6GG$ conjugate and its individual peptides ($(VPGFG)_6G$'and azide-$(GPO)_6GG$), b) the $(VPGFG)_6$-$(GPO)_7GG$ conjugate and its individual peptides. The insets are enlarged sections of the entire spectra for easy visualization of the azide peaks located at 2100 cm^{-1}.

The presence of the azide peaks only for the CLP spectra and not the conjugate spectra in Figure 3.4 a & b indicates that either all of the azide was consumed in the reaction or that all of the azide containing CLP was purified out from the ELP-CLP conjugates. The data corroborates the mass spectra data and we can be reasonably certain that the products collected and purified are those that we intended to make.

3.3.2 Circular dichroism characterization of the ELP-CLP conjugate triple helix

3.3.2.1 Confirmation of ELP-CLP conjugates triple helix formation

A critical process for ELP-CLP self-assembly into vesicular nanoparticles is the formation of triple helices within the ELP-*b*-CLP conjugate. Just as with the CLPs by themselves, circular dichroism spectroscopy can be used to assess this formation by first analyzing the circular dichroic wavelength spectra of the conjugates. Furthermore, it is desired again to confirm that this triple helix formation can be melted out at high temperatures. By ensuring that the triple helix of the conjugates can be melted out, we can expect that self-assembled particles will likely dissociate at these higher temperatures due to the triple helix being required for maintaining particle stability. The confirmation of triple helix formation for both $(VPGFG)_6$-$(GPO)_7GG$ and $(VPGFG)_6$-$(GPO)_6GG$ is demonstrated in Figure 3.5 below.

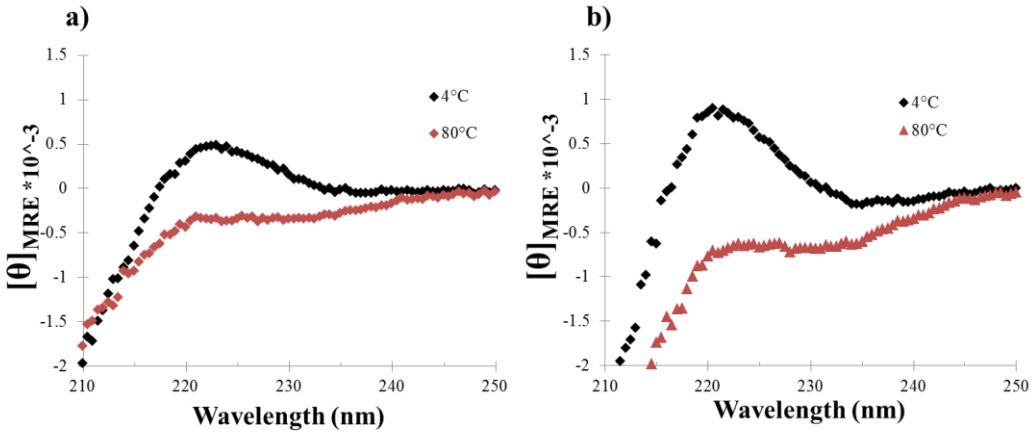

Figure 3.5: Confirmation of triple helix formation and high temperature melting for a) $(VPGFG)_6$-$(GPO)_7GG$ (0.1mM) and b) $(VPGFG)_6$-$(GPO)_6GG$ (0.35mM). The triple helix is verified by maximal ellipticity at the 225nm wavelength. The black and red curves correspond to spectra at 4°C and 80°C respectively. The solution media is 10mM DPBS.

As demonstrated by Figure 3.5, both of the conjugate systems discussed in this work are able to form triple helices as is evident by the ellipticity maxima at approximately 225nm for the 4°C curves. This result indicates that both conjugate systems are at the very least capable of taking the first step toward the self-assembly process with triple helix formation. Furthermore, Figure 3.5 indicates that both ELP-CLP triple helices are able to be melted out at 80°C, as evident by the lack of triple helical spectra for the 80°C curves. This was indeed expected as the extra stability imparted by the ELP to the melting temperature should not be so significant that the triple helices can't be melted at 80°C. The melting of the triple helices supports the notion that if particles can form then they can likely be dissociated at high temperatures similar to the previous ELP-CLP system.[4]

3.3.2.2 Determination of ELP-CLP conjugate triple helical melting temperatures

While verification of the triple helix formation is of critical importance for the self-assembly of ELP-CLP conjugates into vesicular nanoparticles, it is perhaps more useful to determine the melting temperature at which the triple helix (and as a result the possible particle) begins to unfold and dissociate. Similar to the data in section 3.2.1.2, the melting temperature of the triple helix in the ELP-CLP conjugates can be determined from analysis of the maximal ellipticity of CLPs at the 225nm mark as a function of temperature. Such temperature scans are shown in Figure 3.6 below.

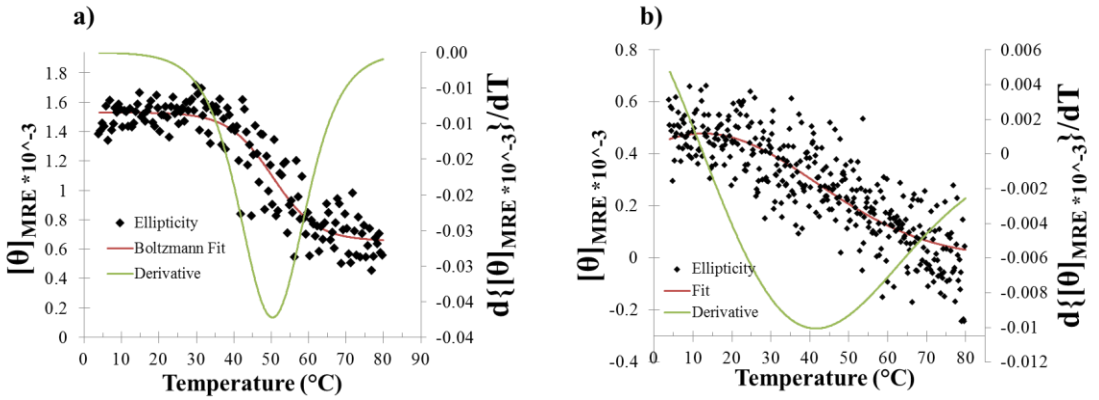

Figure 3.6: Triple helical melting curves of a) $(VPGFG)_6$-$(GPO)_7GG$ and b) $(VPGFG)_6$-$(GPO)_6GG$. Both conjugates were measured at a concentration of 0.35mM in10mM DPBS with a scanning rate of 10°C/hour while monitoring ellipticity at 225nm. Both conjugate melting curves are presented after subtraction of the ELP melting curve. The fit for $(VPGFG)_6$-$(GPO)_6GG$ was an Exp3P2 fit from Origin software.

From Figure 3.6 the melting temperature of the CLP triple helix for each ELP-CLP conjugate can be determined. The melting temperatures for ELP-$(GPO)_6GG$ and ELP-$(GPO)_7GG$ are 42°C and 50°C, respectively. Similar to what was reported in the original ELP-CLP nanoparticle system, an increase in melting temperature is observed for each conjugate.[4] This increase is likely due to the extra stability imparted by ELP chain hydrophobic contacts. An increase of 13°C is observed for the $(GPO)_6GG$ system and an increase by 6°C is indicated for the $(GPO)_7GG$ conjugate. From the melting temperatures of the these conjugates we can hypothesize that the $(GPO)_6GG$ system will likely have a hybridization temperature range that falls within the desired region of that suggested in Table 1.2. The $(GPO)_7GG$ conjugate system appears to have a melting temperature that falls just outside of the desired hybridization region. The dynamic light scattering studies of these conjugates presented later may offer a

more precise determination of the hybridization region for these potential particle systems.

There are several things worth noting in regards to the data in Figure 3.6. Most notably, the data for the $(VPGFG)_6$-$(GPO)_6GG$ conjugate do not seem to have the same general shape as $(VPGFG)_6$-$(GPO)_7GG$, and the $(GPO)_6GG$ conjugate generally appears less resolved and lacks a steep melting curve. There are a couple of things to consider with regard to this observation.

Firstly, both spectra in Figure 3.6 are intended to be spectra of the CLP domain alone. Following the work of the original ELP-CLP system, a melting curve spectra at 225 nm of the $(VPGFG)_6G'$ peptide was generated and is shown in Figure B.4 (see appendix B). The ELP melting curve spectra follow the same linear shape as that originally reported by Luo *et al*.[4] In that work, the ELP melting curve was subtracted from the conjugate melting curves so that the resulting ellipticity data would solely be representative of the CLP domain. While this procedure was repeated to obtain the spectra shown in Figure 3.6, it should be noted that the method may not be inherently correct.

If the sample in question has formed nanoparticles or at the very least the triple helix has formed, then it is hypothesized that the ELP should be in its collapsed state (see chapter 1). According to a large amount of literature, this collapsed ELP state should possess a β-turn type II (or possibly other types) structure that can be observed using circular dichroism spectroscopy.[22-24] Therefore, the conjugate raw CD spectra should possess both a triple helical and a β-turn component above the ELP-CLP conjugate triple helical melting temperature. Below this melting temperature, both components should lose their characteristic structure and adopt a random unordered

confirmation. While it hasn't been completely verified, the ELP melting curve shown in Figure B.4 as well as that reported by Luo *et al*, does not appear to adopt the properties that are indicative of β-turn type II structures.[24] I hypothesize rather that these ELP melting curves are gradual changes in random coil/disordered peptide structure as a function of temperature. If this is the case, then it would not be appropriate to subtract a random coil/disordered ELP spectra from an ELP-CLP conjugate spectra that may possess both triple helical and β-turn type II conformations above the ELP-CLP triple helical melting temperature. However, the subtraction of the ELP melting spectra in Figure B.4 would likely be appropriate after the melting temperature of the ELP-CLP domain has been reached, given that both spectra would likely correspond to random disordered peptides. Therein lies the problem; if we are trying to determine the T_m of the CLP component of the ELP-CLP conjugate, and determination of this value depends on the precise subtraction of two different sets of ELP secondary structure (β-turns below T_m, random coils above T_m) then a prior knowledge of the T_m would be required in order to determine which portion of the ELP-CLP melting curve should be subtracted with which ELP state (β-turns or extended state).

Clearly this problem is quite complex and requires significant future study of the circular dichroism of short ELPs. The purpose of this discussion was to chiefly explore the reasons for why the $(VPGFG)_6$-$(GPO)_6GG$ spectra possesses less resolution, but it has also served to call into question the current subtraction method which may have important implications for the accuracy of the $(VPGFG)_6$-$(GPO)_7GG$ melting curve data as well.

While the previous arguments may be technically correct for all ELP-CLP conjugate systems, from a practical perspective the correct ELP subtraction method may only have significant value to weak triple helical systems (such as ELP-$(GPO)_6GG$), as will now be discussed. Regardless of if the ELP is adopting a β-turn structure or not, it is well known that the circular dichroic intensity of β-turns is relatively weak in comparison to the more intense CD spectra observed for α-helices, β-sheets, and triple helices.[25] Because of the differences in intensities for these structures, it is hypothesized that ELP-CLP systems that possess a 'strong' CLP triple helix with relatively high melting temperatures will also strongly possess a CLP-like CD spectra. If the CLP-like CD spectra of an ELP-CLP is intense enough, then minor subtractions of ELP melting curves (representing random coils or not) will do little to affect the overall sigmoidal CLP melt curve shape. If an ELP-CLP system possesses a weaker CLP domain, then an incorrect subtraction of the 'wrong' kind of ELP CD spectra would result in an apparent distorted 'CLP only' CD spectrum of the conjugate.

The data in Figure 3.6 can be used to support this argument. Even after subtraction of the ELP melting curve spectra (Figure B.4), the ELP-$(GPO)_7GG$ triple helical melt curve (Figure 3.6a) follows the same sigmoidal shape that is common to the melting curve of CLPs alone (see Figure 3.2). In contrast the melting curve shape of ELP-$(GPO)_6GG$ (Figure 3.6b) is not easily discernable and the data have a higher correlation with a three parameter exponential function than a sigmoidal Boltzmann function (fit comparison not shown). Because $(GPO)_6GG$ is on the repeat unit threshold of being able to form a triple helix, its triple helical strength (mostly due to an entropic driving force) is significantly weak and as a result, it's melting

temperature and triple helical CD signal are also weak (see Figures 3.1 and 3.2).[7, 26] Due to the weak triple helix, the CD signal of the ELP domain, whether it be β-turn or random coil, is more prominent than it is in ELP-$(GPO)_7$GG or in the previous system ELP-$(GPO)_4$GFOGER$(GPO)_4$GG.[4] Therefore, not only does the melting curve of ELP-$(GPO)_6$GG (raw non-subtracted data) intrinsically appear to not resemble a CLP melting curve, but an incorrect subtraction of a random-coil ELP melting curve (such as that hypothesized for Figure B.4) from an actual β-turn formed system would result in a less resolved or less CLP-like melting curve of the CLP portion of the ELP-$(GPO)_6$GG conjugate.

Future work will have to focus on more precise methods of ELP subtraction from conjugate CD spectra to improve the data quality for ELP-CLP systems with weak triple helices. Perhaps the CD melting temperature value of the ELP-$(GPO)_6$GG conjugate is not as accurate as would be desired, but in the interim the calculated value can suffice as an estimate.

3.4 Nanoparticle Formation and Characterization of ELP-CLP Conjugates

3.4.1 Effect of CLP domain modifications on particle formation and properties

3.4.1.1 DLS analysis of particles

Due to the requirement of triple helix folding for nanoparticle formation to occur, the determination of ELP-CLP conjugate triple helical melting temperatures allows for the reasonable prediction of the temperature at which particle formation would begin to occur. As is discussed in section 2.3.3.2, the procedure for making particles begins by heating a 1mg/mL sample of ELP-CLP conjugates in pure water well above their melting temperature and performing a hot filtration of the sample into

a standard quartz cuvette. The hot filtration ensures the removal of large dust contaminants while conjugate is in a state where particles cannot form. The cuvette and sample are then slowly cooled to room temperature in a controlled fashion using the DLS instrument which simultaneously cools and monitors the sample for particle formation. The analysis of particle formation in terms of the number average particle diameter and derived count rate (the theoretical number of photons hitting the detector; or relative scattering intensity) during this cooling process is shown in supplemental Figures B.5 and B.6 for $(VPGFG)_6$-$(GPO)_7GG$ and $(VPGFG)_6$-$(GPO)_6GG$, respectively.

From Figure B.5, particle formation of the $(VPGFG)_6$-$(GPO)_7GG$ conjugate was clearly shown to occur both by visual observation and by dynamic light scattering results. More specifically, the increase in number average diameter as the temperature was lowered to 50°C and below suggests the formation of nanoparticles began to occur at the triple helical melting temperature that was determined from CD. This result was indeed anticipated and it seems the determined melting temperature of the $(VPGFG)_6$-$(GPO)_7GG$ conjugate from CD is corroborated by DLS. As further confirmation, the derived count rate parameter also increases as a function of temperature and correlates well with the observed particle diameter. This is expected as the number of particles increases, so too should the relative number of photons that reach the detector. The correlation of derived count rate with diameter has been reported in the previous ELP-CLP system as a means to qualitatively verify particle formation.[4, 27] A different representation of the data in Figure B.5 is shown in Figure B.7 where instead of averages, the number distributions of particles is plotted as a function of temperature.

To ensure that the particles were able to maintain stability at room temperature over a time period in which they could be stored prior to drug delivery applications, the particle diameter and count rate of the $(VPGFG)_6$-$(GPO)_7$ particles was continuously monitored for close to 35 hours, as shown in Figure B.8 (see Appendix B). From Figure B.8, the particles were shown to maintain a consistent size and retain stability over 35 hours highlighting their successful storage when not in use.

After the particles were initially formed, an analysis of number diameter distributions was performed as the nanoparticle suspension was heated in a stepwise fashion over time. The purpose of this study was to confirm the cooling trend observations that took place during particle formation, but was also done to gain a more detailed picture of the potential collagen protein hybridization region for this system. The results of the $(VPGFG)_6$-$(GPO)_6GG$ number diameter particle distribution as a function of heating is shown in Figure 3.7. Replicate data for a separate batch of particles is shown in Figure B.9.

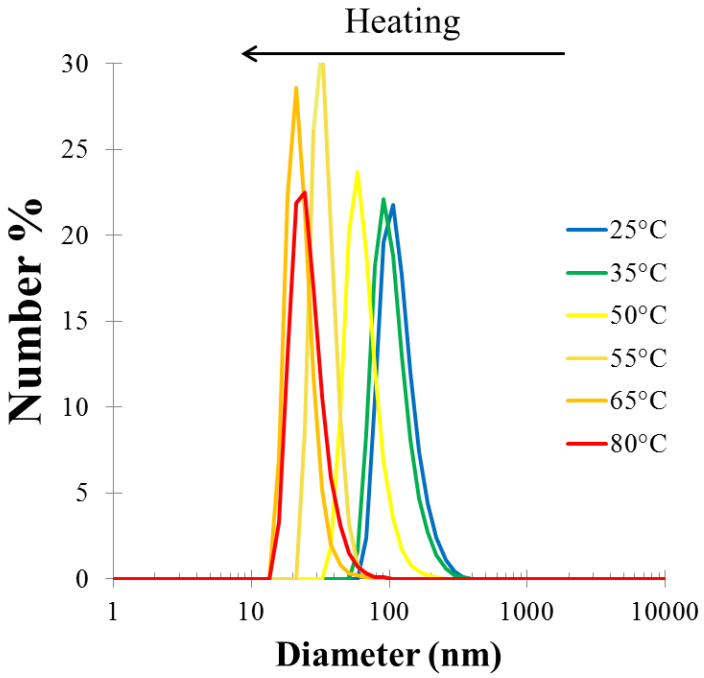

Figure 3.7: Dynamic light scattering analysis of $(VPGFG)_6$-$(GPO)_7GG$ nanoparticle suspension as a function of stepwise heating. Each data point represents the average of three diameter measurements.

The first observation to be made from Figure 3.7 is the overall similarity in particle number diameter distributions to that of Figure B.7. In both figures the particles possess larger (approximately 100nm) diameters below, and smaller diameters above, the 50°C melting temperature. In Figure 3.7, the apparent 50°C melting temperature transition is again observed. Lastly, we can see a significant difference in size between the 35°C and 50°C, as well as 50°C and 55°C temperature data points. This suggests a significant difference between distributions from when the particle is formed at 35°C to when the particle is beginning to melt at 50°C to more complete melting and particle dissolution at 55°C. The slight change in distribution from 35°C to 50°C suggests that this temperature range is near the edge of particle

stability and likely falls within the upper end of the suggested CLP-collagen hybridization region (Table 1.2). It is difficult to tell from Figure 3.7 the precise range of the proposed hybridization region for this particle, but future studies that collect more data points between the 35°C and 50°C temperature region may shed more light on the precise nature of the hybridization region and its specific effects on nanoparticle size.

In contrast to the $(VPGFG)_6$-$(GPO)_7GG$ system, the $(VPGFG)_6$-$(GPO)_6GG$ conjugate did not readily form particles upon cooling to and below its 42°C triple helical melting temperature (Figure B.6). There are a couple of reasons that might explain this observation. First it should be noted that the sample for which the data in Figure B.6 was generated possessed a concentration that was slightly lower than 1mg/mL (approximately 0.9mg/mL) due to the low yields obtained in initial syntheses. While the decrease in concentration certainly can lead to a decrease in light scattering, 0.9mg/mL would certainly be expected to still form nanoparticles given that low critical micelle concentrations are common for block copolymer like systems, such as the case for the ELP-CLP system.[8] Nonetheless, a replicate study should be performed with larger concentrations to confirm the inability of this conjugate to form nanoparticles.

One reason why nanoparticle formation may not be occurring is possibly due to the triple helix of the $(GPO)_6GG$ CLP domain simply being too weak to act as a sufficient nucleation center to elicit the LCST collapse of the ELP domain. As has been previously discussed, the $(GPO)_6GG$ CLP has the lowest triple helical melting temperature as well as the weakest normalized residue triple helical CD intensity of all the CLPs in the small library, as is evident by Figures 3.2 and 3.1 respectively. The

lower melting temperature of $(GPO)_6GG$ in comparison to the CLP with one repeat longer ($(GPO)_7GG$) is in part due to $(GPO)_6GG$ having a higher entropic preorganization cost than $(GPO)_7GG$ due to lack of additional imino acids to contribute to conformational stability. Therefore, in comparison to ELP-$(GPO)_7GG$, the CLP domain of ELP-$(GPO)_6$ GG overall has a lower degree of chain order. It can then be reasoned that this more unordered triple helix may not impart the ELP chains with a high enough order to substantially increase the change of entropy of the waters of hydrophobic hydration and therefore not elicit an inverse transition temperature collapse.

In order to test this hypothesis, future work can be aimed at creating CLPs of the same volume fraction as $(GPO)_6GG$ but with significantly higher melting temperatures. This can be achieved by replacing the hydroxyproline residues with fluoroproline (Flp) residues. As discussed in Chapter 1, fluoroproline residues in the Y_{AA} position yield 'hyperstable' triple helices in comparison to hydroxyproline residues in the same position.[28] This stabilization has been shown to be the result of subtle differences in the (exo) ring pucker conformation caused by the difference of fluorine's and hydroxyl's electronegativity.[6] In this regard, the fluorproline CLPs have been ascribed with an entropic basis for stabilization while hydroxyproline CLPs have both entropic and enthaplic contributions to stability.[29] With this in mind, we can then expect that a $(Gly\text{-}Pro\text{-}Flp)_6GG$ ($T_{m,estimated} \approx 45°C$) sequence will provide the additional order that is needed to modify the change of entropy of hydrophobic hydration and result in the inverse transition collapse of ELPs that is required for nanoparticle formation.[6]

3.4.1.2 TEM analysis of particles

With the apparent formation of nanoparticles for the $(VPGFG)_6(GPO)_7GG$ system, both by visual observation and by dynamic light scattering (Figures B.5, B.7, and 3.7), it was necessary to determine if the observed particles are forming the same vesicular morphology as that observed in the previous $(VPGFG)_6$-$(GPO)_4GFOGER(GPO)_4GG$ system.[4] Perhaps the simplest way to determine the nanoparticle morphology is to view the particles via transmission electron microscopy (TEM). Following the protocols described in section 2.3.4, previously ionized TEM carbon coated Cu grids were dipped in 17μL solutions of 1mg/mL solution of disperse (DLS verified) $(VPGFG)_6$-$(GPO)_7GG$ nanoparticles. Similar spotting was performed with 1wt% phosphotungstic acid (PTA) so that the grids would be negatively stained to improve the contrast of nanoparticles. These spotting protocols were performed both at room temperature and at the 50°C melting temperature of the ELP-$(GPO)_7GG$ particles. Figure 3.8 below shows typical TEM images of both the 25°C and 50°C incubated ELP-$(GPO)_7GG$ nanoparticles stained with PTA.

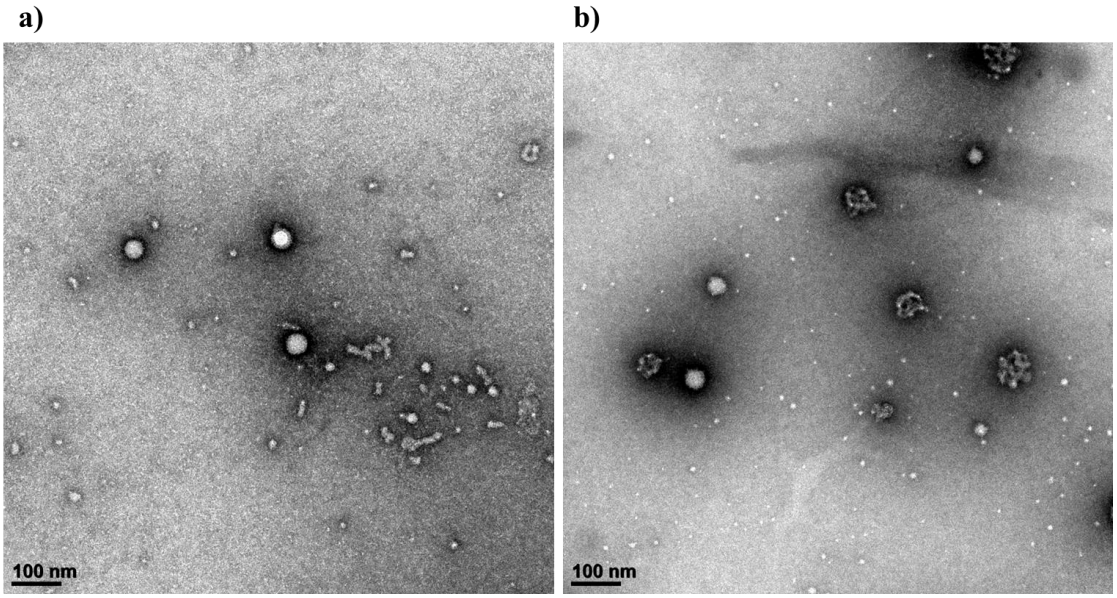

Figure 3.8: TEM images of 1wt% PTA stained $(VPGFG)_6$-$(GPO)_7GG$ nanoparticles previously incubated at a) 25°C and b) 50°C for thirty minutes prior to grid spotting.

As seen in Figure 3.8a, spherical nanoparticles of approximately 45nm in diameter are observed for the 25°C incubation and spotting temperature. In contrast, objects seen in Figure 3.8b seem to consist of nanoparticles that are in a melted and broken state or are on their way toward complete dissociation. The presence of the nanoparticles at 25°C and the apparent thermal decomposition of the same nanoparticles at 50°C, corroborate both the dynamic light scattering results that indicate particle formation as well as the thermal melting temperature at 50°C that was confirmed both by DLS and CD. It can be noted that not all particles in Figure 3.8b are in the melted state, but this might be expected given that the incubation was precisely at the melting temperature. Additionally from Figure 3.8a, we can hypothesize that the observed spherical particles are likely to be vesicular as opposed to being micellar.

This hypothesis is based off of two observations. First the nanoparticles seem to have a dark corona surrounding a light interior. A vesicular bilayer wall will possess some thickness in comparison to the interior of the nanoparticle. One can then imagine that an electron beam will transmit through the center of a vesicular nanoparticle more easily than it would the coronal outer edges because the coronal edges is where the bilayer is present in greatest thickness in the Z-direction (the plane going into the page). In other words, the bilayer on the outer edges of the nanoparticle possesses nearly the entire height of the nanoparticle; whereas the very center of the nanoparticle should only possess two bilayers of thickness (one on top and one at the bottom of the particle in the Z-direction). Therefore, based on the transmission of the electron beam, and observing opacity in the outer nanoparticle corona in comparison to the inner nanoparticle interior, we can then speculate that this variation in opacity from outside to inside is indicative of the vesicular structure.

The second observation is that of the size of the nanoparticle itself. From CLP literature we know that every (G-P-O) repeat unit possesses a unit length of approximately 0.9nm.[6, 30] We can then estimate the length of the $(GPO)_7GG$ CLP to be approximately 6.3nm. Furthermore, from radius of gyration calculations (calculations not shown for brevity) of the collapsed ELP domain, we can estimate the collapsed ELP domain to possess a total length of approximately 1.7nm. This calculated value is in good accord with the reported unit height of a β-spiral, which our collapsed ELP would theoretically be expected to form given that a single β-spiral turn consists of three pentamers (with approximately two turns per one spiral revolution). [1, 16, 22] This brings the total length of the ELP-$(GPO)_7GG$ conjugate to be approximately 8nm. Therefore, if spherical micelles were forming instead of vesicles, then we would

expect to see particles with a diameter of approximately 16nm, due to the ELPs forming a single central core with a CLP exterior corona.

Additionally, there is no significant expectation that micellar structures would form in the first place. From block copolymer assembly literature trends, this micellar assembly would theoretically be fairly implausible given that the original system was a vesicular structure and that decreasing the hydrophilic block (CLP) could only lead to a continued vesicular structure or large compound (inverted) micelles (this structure is unlikely due to the rod-like nature of CLPs).[8, 9] As an example, Yoon *et al* showed that a polyproline sequence conjugated to a cell penetrating peptide maintained vesicular nanoparticle morphology as the hydrophilic volume fraction was reduced.[31]

Based off of this discussion and the apparent size of the particles being approximately 45nm, we can then say that the vesicular structure is the most plausible. With the calculated conjugate length of 8nm, the total bilayer length should be 16nm. With the two sides of the 45nm particle wall equaling 32nm total, only about 13nm of diameter make up the interior spherical space. While this may seem small, it is geometrically plausible and it should be enough space for small molecule cargoes. A few other things are important to mention here. First the particle sizing is performed for the observable light interior and does not include the dark corona. If there is a portion of the dark corona that consists of the bilayer wall then this extra length should be included in the particle sizing analysis. Second, the cited 45nm size applies to Figure 3.5a with a sample size of three. Similar particle sizes however can be seen in Figure B.10 and B.11 for the PTA and uranyl acetate stains respectively, and some variation of size is observed. Future work can focus on replicate studies, perhaps with

higher concentrations of particles (post assembly) to increase the number of particles per image.

One last important note is the difference in sizes between TEM and DLS. The DLS indicates the size of particles to be approximately 100nm in diameter while TEM shows sizes approximately half this value. When making comparisons between these techniques it is important to remember the difference between the DLS hydrodynamic diameter and the dry geometric diameter.[32] While researchers will commonly report success when these two techniques yield identical diameters, in reality the two diameters represent completely different values given that they are in two completely different environments. Had the differences between the two results been much greater then perhaps there would be cause for concern, but the observed difference is in the realm of possibility.

3.4.2 Inverse transition temperature of the $(VPGFG)_6$-$(GPO)_7GG$ nanoparticle

3.4.2.1 DLS

Noting the observation of the lack of formation of the $(VPGFG)_6$-$(GPO)_6GG$ conjugate and the hypothesis that this is caused by the higher entropy possessed by the $(GPO)_6GG$ triple helix, it was then logical to determine the possible effect of the $(GPO)_7GG$ CLP on the collapsed ELP-CLP nanoparticles inverse transition temperature. Since it is hypothesized that the ELP is in the collapsed state when the nanoparticle is assembled and that the nanoparticle maintains consistent stability at 25°C, then there may exist a temperature below 25°C in which the nanoparticle can dissociate via rehydration and extension of the ELP chains through the inverse transition temperature effect. This can simply be tested via DLS by cooling the

1mg/mL$(VPGFG)_6$-$(GPO)_7$GG nanoparticle solution from 25°C to 5°C and observing changes to particle diameter and photon count rate. The number distributions of particle sizes of $(VPGFG)_6$-$(GPO)_7$GG conjugate are plotted as a function of cooling and are shown in Figure 3.9 below.

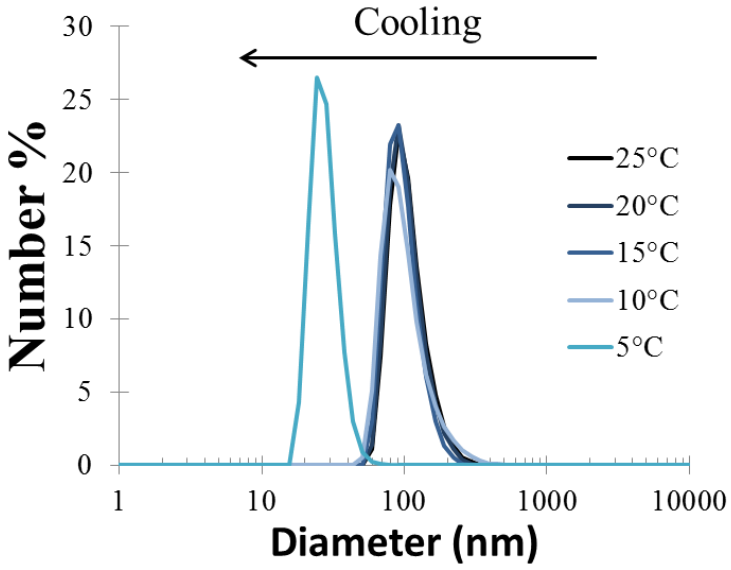

Figure 3.9: Dynamic light scattering particle distributions of $(VPGFG)_6$-$(GPO)_7$GG conjugate as the nanoparticles are slowly cooled down from 25°C to 5°C. The inverse temperature transition occurs between 10°C and 5°C as is indicated by the significant change in particle size distributions at these temperatures.

As demonstrated by Figure 3.9, number particle size distributions are largely maintained at lower temperatures until the temperature changes from 10°C to 5°C, at which point there is a marked shift in the particle size distribution. Replicate data for a separate batch of particles is shown in Figure B.12 in the appendix. This dramatic shift in particle size within a narrow temperature window (5°C) is indicative of an inverse

transition change similar to that observed in Figure 3.3 and as that in other ELP transition temperature reports.[18, 33] From Figure 3.9, we know the transition temperature occurs between 5°C and 10°C . Future work will be focused on obtaining a more precise value within that range, but for now it may be sufficient to approximate the inverse transition temperature for this conjugate as 7.5°C. At this transition temperature, full ELP chain extension occurs and the particle completely dissociates into triple helical conjugates with spread out hydrated ELP chains. The overall transition is likely akin to the reverse process of Figure 1.4.

3.4.2.2 TEM

In order to verify the DLS results, TEM can be performed on particles that have been incubated below 7.5°C. Similar to what was observed for the 50°C incubation of the particles in Figure 3.8b, we would expect to find broken up particles or misshapen particles. Figure 3.10 below highlights two representative images of $(VPGFG)_6$-$(GPO)_7GG$ particles that were incubated at 4°C following the protocol discussed in section 2.3.4.2.

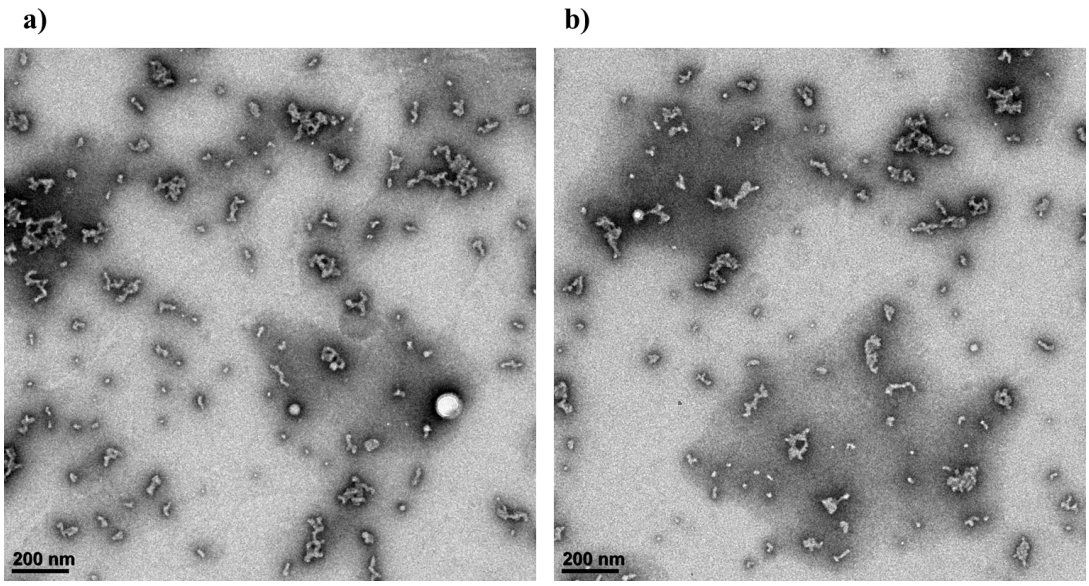

Figure 3.10: TEM images of $(VPGFG)_6$-$(GPO)_7GG$ nanoparticles that were incubated at 4°C for thirty minutes prior to cold spotting and staining onto TEM grids. Images a) and b) are of the identical sample on the same grid but are different by their locations on the grid.

Similar to what was observed by DLS in Figure 3.9, the TEM images of the $(VPGFG)_6$-$(GPO)_7GG$ conjugate indicate that the nanoparticles have broken up and dissociated completely. We know from Figure 3.5 that the conjugate is indeed forming a triple helix, so the dissociation must be affiliated with the ELP domain. Therefore it seems fairly clear that the lower critical solution temperature is indeed being observed for this conjugate system. It is not immediately clear what the nature of the dissociated product morphology is representative of, but upon first glance there doesn't appear to be any significant order to the structures implying they are simply monomeric triple helical random aggregates.

3.4.2.3 Discussion and hypotheses

From the result of the $(VPGFG)_6$-$(GPO)_6GG$, we knew that it was possible for the $(VPGFG)_6$-$(GPO)_7GG$ system to possess an inverse transition temperature, but the result was not necessarily expected since it had traditionally been thought that modifications to ELP domains primary sequence or repeat length would be required to make the transition temperature of the nanoparticle system observable (>4°C).

The hypothesis postulated as an explanation for the lack of $(VPGFG)_6$-$(GPO)_6GG$ nanoparticle formation can also apply to the present observation of an inverse transition temperature for the $(VPGFG)_6$-$(GPO)_7GG$ system. In comparison to the original $(GPO)_4GFOGER(GPO)_4GG$ CLP, $(GPO)_7GG$ has a lower melting temperature and likely has a lower normalized triple helical stability as well.[4] It is difficult to say without specific thermodynamic measurements whether the additional triple helical stability of the original CLP is primarily entropic or enthalpic in origin, but it is likely to be some combination of both. Nonetheless it is possible that the increased triple helical stability of the $(GPO)_4GFOGER(GPO)_4GG$ imparts higher order to the $(VPGFG)_6G$' ELP chains than the $(GPO)_7GG$ CLP. As thoroughly discussed above, the lower order of the $(VPGFG)_6$-$(GPO)_7GG$ conjugate would result in an increase to the change of entropy of hydrophobic hydration and thereby increase the inverse transition temperature. Similar to the test proposed for the $(GPO)_6GG$ CLP repeat, a $(VPGFG)_6$-$(Gly\text{-}Pro\text{-}Flp)_7GG$ would likely be a worthy test conjugate to determine if the effect of the $(GPO)_7GG$ CLP is the result of its melting temperature. If this is indeed the case then the $(VPGFG)_6$-$(Gly\text{-}Pro\text{-}Flp)_7GG$ would not be expected to possess a lower critical solution temperature at all. The same test but with an opposite expected outcome could also be conducted with the $(VPGFG)_6$-$(GPO)_3GFOGER(GPO)_3GG$ conjugate since $(GPO)_3GFOGER(GPO)_3GG$ has a lower

melting temperature than $(GPO)_7GG$. In this case it would then be expected that the lower critical solution temperature of the conjugate would increase. This is indeed planned as future work to probe the role of the CLP melting temperature on the inverse transition temperature more thoroughly.

Although the melting temperature of the CLP could indeed be the root cause of the observed LCST transition of the ELP-$(GPO)_7GG$ particle as well as the lack of formation of the ELP-$(GPO)_6GG$ conjugate system, it is important to recognize the possible significance of the total volume fraction of the CLP domain as well. As was briefly discussed earlier in this chapter, the volume fraction of the $(GPO)_7GG$ conjugate is significantly lower than that of the original $(GPO)_4GFOGER(GPO)_4GG$ CLP system, and as a result differences in self-assembly and morphology are certainly possible between the two systems.

From self-assembly theory, it is well known that decreasing the hydrophilic chain length can lead to a decrease in hydrophilic chain-chain repulsion, which in turn can lead to an increase in hydrophobic chain stretching.[8, 31, 34] It could then stand to reason that this ELP chain stretching is decreasing the order of the ELP chains and thereby also modifying the change in entropy of hydrophobic hydration.

Similar to the melting temperature hypothesis, this chain stretching hypothesis can easily be tested by modifying the CLP sequences in the ELP-CLP conjugate. Specifically, the $(GPP)_{10}$ CLP has been shown to possess a melting temperature that is approximately the same as that of $(GPO)_7GG$ but possess three more repeat lengths than $(GPO)_7GG$.[6] Because of this, the ELP-$(GPP)_{10}GG$ sequence would be able to directly test the effect of $(GPO)_7GG$'s repeat length on the hydrophobic chain stretching without significant alterations being present to the melting temperature. If

the chain stretching hypothesis was correct then we would expect the nanoparticle lower critical solution temperature observed in Figure 3.9 and Figure 3.10 to disappear for the ELP-$(GPP)_{10}$GG conjugate sequence. Preliminary work has already been completed regarding the synthesis of this peptide, and future work will focus on the CuAAC conjugation to ELP.

It should be noted briefly that the chain length hypothesis is based on chain-chain repulsion which in turn affects the hydrophobic stretching and order of the ELP domain. While it is postulated here that the primary effector of hydrophilic chain-chain repulsion is the length of the hydrophilic CLP domain, chemical effects such as the sequence and overall hydration structure of the hydrophilic domain may also be key to differences observed in this CLP-CLP chain repulsion. It has been reported in the literature that $(GPP)_{10}$GG possess significantly lower quantity of water surrounding its triple helical chains than its (GPO) counterparts.[6] This difference in hydration shell could cause a significant difference with regard to the CLP-CLP chain repulsion that is hypothesized for the proposed $(GPP)_{10}$GG conjugate. A superior CLP that is to be used for testing the chain length hypothesis would then have to have minimal differences in hydration structure to that of (GPO) CLPs and also possess an identical melting temperature. Unfortunately it is difficult to predict *de novo* the precise hydration shell or melting temperature of any CLP just from its sequence alone. Therefore, future studies will have to suffice for maintaining the same melting temperature and consider the role CLP hydration states as needed.

REFERENCES

1. Urry, D. W., Physical chemistry of biological free energy transduction as demonstrated by elastic protein-based polymers. Journal of Physical Chemistry B 1997, 101 (51), 11007-11028.

2. Wang, A. Y.; Mo, X.; Chen, C. S.; Yu, S. M., Facile modification of collagen directed by collagen mimetic peptides. Journal of the American Chemical Society 2005, 127 (12), 4130-4131.

3. Persikov, A. V.; Ramshaw, J. A. M.; Brodsky, B., Collagen model peptides: Sequence dependence of triple-helix stability. Biopolymers 2000, 55 (6), 436-450.

4. Luo, T. Z.; Kiick, K. L., Noncovalent Modulation of the Inverse Temperature Transition and Self-Assembly of Elastin-b-Collagen-like Peptide Bioconjugates. Journal of the American Chemical Society 2015, 137 (49), 15362-15365.

5. Knight, C. G.; Morton, L. F.; Peachey, A. R.; Tuckwell, D. S.; Farndale, R. W.; Barnes, M. J., The collagen-binding A-domains of integrins alpha(1)beta(1) and alpha(2)beta(1) recognize the same specific amino acid sequence, GFOGER, in native (triple-helical) collagens. Journal of Biological Chemistry 2000, 275 (1), 35-40.

6. Shoulders, M. D.; Raines, R. T., Collagen Structure and Stability. In Annual Review of Biochemistry, Annual Reviews: Palo Alto, 2009; Vol. 78, pp 929-958.

7. Persikov, A. V.; Ramshaw, J. A. M.; Kirkpatrick, A.; Brodsky, B., Amino acid propensities for the collagen triple-helix. Biochemistry 2000, 39 (48), 14960-14967.

8. Mai, Y. Y.; Eisenberg, A., Self-assembly of block copolymers. Chemical Society Reviews 2012, 41 (18), 5969-5985.

9. Jain, S.; Bates, F. S., On the origins of morphological complexity in block copolymer surfactants. Science 2003, 300 (5618), 460-464.

10. Olsen, B. D.; Segalman, R. A., Self-assembly of rod-coil block copolymers. Materials Science & Engineering R-Reports 2008, 62 (2), 37-66.

11. Persikov, A. V.; Ramshaw, J. A. M.; Kirkpatrick, A.; Brodsky, B., Peptide investigations of pairwise interactions in the collagen triple-helix. Journal of Molecular Biology 2002, 316 (2), 385-394.

12. Persikov, A. V.; Xu, Y. J.; Brodsky, B., Equilibrium thermal transitions of collagen model peptides. Protein Science 2004, 13 (4), 893-902.

13. Krishna, O. D.; Kiick, K. L., Supramolecular Assembly of Electrostatically Stabilized, Hydroxyproline-Lacking Collagen-Mimetic Peptides. Biomacromolecules 2009, 10 (9), 2626-2631.

14. Luo, J. N.; Tong, Y. W., Self-Assembly of Collagen-Mimetic Peptide Amphiphiles into Biofunctional Nanofiber. Acs Nano 2011, 5 (10), 7739-7747.

15. Engel, J.; Bachinger, H. P., Structure, stability and folding of the collagen triple helix. In Collagen: Primer in Structure, Processing and Assembly, Brinckmann, J.; Notbohm, H.; Muller, P. K., Eds. Springer-Verlag Berlin: Berlin, 2005; Vol. 247, pp 7-33.

16. Rodriguez-Cabello, J. C.; Prieto, S.; Reguera, J.; Arias, F. J.; Ribeiro, A., Biofunctional design of elastin-like polymers for advanced applications in nanobiotechnology. Journal of Biomaterials Science-Polymer Edition 2007, 18 (3), 269-286.

17. Meyer, D. E.; Chilkoti, A., Purification of recombinant proteins by fusion with thermally-responsive polypeptides. Nature Biotechnology 1999, 17 (11), 1112-1115.

18. Nuhn, H.; Klok, H. A., Secondary Structure Formation and LCST Behavior of Short Elastin-Like Peptides. Biomacromolecules 2008, 9 (10), 2755-2763.

19. Chilkoti, A.; Dreher, M. R.; Meyer, D. E., Design of thermally responsive, recombinant polypeptide carriers for targeted drug delivery. Advanced Drug Delivery Reviews 2002, 54 (8), 1093-1111.

20. Prough, D. S.; Bidani, A., Hyperchloremic metabolic acidosis is a predictable consequence of intraoperative infusion of 0.9% saline. Anesthesiology 1999, 90 (5), 1247-1249.

21. Lambert, J.B.; Shurvell, H.F.; Lightner, D.A.; Cooks, R.G., Electronic Absorption and Chiroptical Spectroscopy. In Organic Structural Spectroscopy; Prentice-Hall: New Jersey, 1998

22. Urry, D. W., PROTEIN ELASTICITY BASED ON CONFORMATIONS OF SEQUENTIAL POLYPEPTIDES - THE BIOLOGICAL ELASTIC FIBER. Journal of Protein Chemistry 1984, 3 (5-6), 403-436.

23. Urry, D. W., ENTROPIC ELASTIC PROCESSES IN PROTEIN MECHANISMS .1. ELASTIC STRUCTURE DUE TO AN INVERSE TEMPERATURE TRANSITION AND ELASTICITY DUE TO INTERNAL CHAIN DYNAMICS. Journal of Protein Chemistry 1988, 7 (1), 1-34.

24. Reiersen, H.; Clarke, A. R.; Rees, A. R., Short elastin-like peptides exhibit the same temperature-induced structural transitions as elastin polymers: Implications for protein engineering. Journal of Molecular Biology 1998, 283 (1), 255-264.

25. Perczel, A.; Hollósi, M,. Turns. In Circular Dichroism and the Conformational Analysis of Biomolecules; Fasman, G.D., Ed.; Plenum Press: New York, 1996. p 285-381.

26. Mizuno, K.; Boudko, S. P.; Engel, J.; Bachinger, H. P., Kinetic Hysteresis in Collagen Folding. Biophysical Journal 2010, 98 (12), 3004-3014.

27. Luo, T. Z.; David, M. A.; Dunshee, L. C.; Scott, R. A.; Urello, M. A.; Price, C.; Kiick, K. L., Thermoresponsive Elastin-b-Collagen-Like Peptide Bioconjugate Nanovesicles for Targeted Drug Delivery to Collagen-Containing Matrices. Biomacromolecules 2017, 18 (8), 2539-2551.

28. Hackley, V. A.; Clogston, J. D., Measuring the Hydrodynamic Size of Nanoparticles in Aqueous Media Using Batch-Mode Dynamic Light Scattering. In Characterization of Nanoparticles Intended for Drug Delivery, McNeil, S. E., Ed. Humana Press Inc: Totowa, 2011; Vol. 697, pp 35-52.

29. Holmgren, S. K.; Taylor, K. M.; Bretscher, L. E.; Raines, R. T., Code for collagen's stability deciphered. Nature 1998, 392 (6677), 666-667.

30. Nishi, Y.; Uchiyama, S.; Doi, M.; Nishiuchi, Y.; Nakazawa, T.; Ohkubo, T.; Kobayashi, Y., Different effects of 4-hydroxyproline and 4-fluoroproline on the stability of collagen triple helix. Biochemistry 2005, 44 (16), 6034-6042.

31. Bella, J.; Eaton, M.; Brodsky, B.; Berman, H. M., CRYSTAL-STRUCTURE AND MOLECULAR-STRUCTURE OF A COLLAGEN-LIKE PEPTIDE AT 1.9-ANGSTROM RESOLUTION. Science 1994, 266 (5182), 75-81.

32. Yoon, Y. R.; Lim, Y. B.; Lee, E.; Lee, M., Self-assembly of a peptide rod-coil: a polyproline rod and a cell-penetrating peptide Tat coil. Chemical Communications 2008, (16), 1892-1894.

33. Pecora, R., Dynamic light scattering measurement of nanometer particles in liquids. Journal of Nanoparticle Research 2000, 2 (2), 123-131.

34. Israelachvili, J. N., Intermolecular and Surface Forces, 3rd Edition. Intermolecular and Surface Forces, 3rd Edition 2011, 1-674.

Chapter 4

CONCLUSIONS AND FUTURE WORK

4.1 Conclusions

The extracellular matrix is known to play significant roles in a number of different diseases.[1] Yet modern treatments of such diseases are largely based on systemic delivery of small molecule therapeutics.[2] Furthermore, many nanoparticle drug delivery strategies rely on the passive targeting to diseased ECM and what active targeting is engineered possesses no specificity for diseased tissue over healthy tissue.[3-5] The development of nanoscale drug delivery vehicles that can explicitly target diseased ECM is still in its infancy. Collagen like peptides (CLPs) offer their properties as denatured collagen protein hybridizers as a means to create such drug carriers.[6,7] In an effort to exploit these properties, the Kiick research group developed a novel elastin-*b*-collagen polypeptide (ELP-CLP) nanoparticle that has potential for active targeting to denatured collagen protein.[8] However, the developed particle lacks the physiologically relevant CLP melting temperatures for sufficient hybridization to take place. Furthermore, the ELP domain has potential for being utilized for on-demand drug release properties through exploitation of its inverse transition temperature properties.

This work has been primarily focused on shortening the length of the CLP domain of the ELP-CLP nanoparticle system to create a particle that is more physiologically relevant for targeted hybridization to denatured collagen protein. A small library of CLPs were synthesized and characterized by circular dichroism to aide

in the determination of what ELP-CLP conjugate systems are to be made. From this library the CLPs $(GPO)_6GG$, $(GPO)_3GFOGER(GPO)_3GG$, and $(GPO)_7GG$ possessed melting temperatures that may yield ELP-CLP conjugates with physiologically relevant CLP-collagen protein hybridization temperatures. Of these, $(GPO)_6GG$ and $(GPO)_7GG$ were chosen to as the CLP domains for the ELP-CLP conjugates. These conjugates were synthesized, purified, characterized, and tested for nanoparticle formation, with only the $(GPO)_7GG$ conjugate forming particles.

With this conjugate a measure of success has been achieved by with respect to the original goal of making the CLP domain more physiologically relevant. The $(VPGFG)_6$-$(GPO)_7GG$ (ELP-shorter CLP) nanoparticle that has been shown to have a theoretical hybridization region centered around 45°C in comparison to the previous system that had a hybridization region centered around 65°C. This new nanoparticle system has roughly similar dimensions to the previous one and possesses an apparent vesicular morphology. Furthermore, it was discovered that the shortened CLP domain also created an upper temperature shift of the inverse transition temperature of the ELP domain, as was demonstrated by the particles being capable of fully solubilizing below the observed 7.5°C transition temperature. This finding is significant and highlights both the impact of the CLP domain on the ELP transition temperature, as well as providing information as to how future modifications can be made to raise the transition temperature further to create a particle that is capable of safe hypothermal nanoparticle degradation and drug release in the body.

4.2 Future Work

From the work presented in Chapter 3, there are two central hypotheses as to why the $(GPO)_6GG$ did not form nanoparticles and the $(GPO)_7GG$ did. These

hypotheses also apply as an explanation for why an LCST transition was observed for the $(GPO)_7GG$ nanoparticle system. The first of these hypotheses is termed the melting temperature hypothesis and postulates that the triple helical stability and melting temperature of the CLP domain is root cause of both the observed LCST transition and the lack of $(GPO)_6GG$ nanoparticle formation. This assertion is based on the speculation that CLPs with lower triple helical stability impart conjugated ELP chains with a state of lower order which in turn affects the change in the increase of entropy of hydrophobic hydration that takes place during the inverse transition temperature ELP collapse.

The second hypothesis is termed the chain length hypothesis. Similar to the melting temperature hypothesis, the order of the ELP chains is believed to be affected but the source of the lower order is due to hydrophobic chain stretching of the ELP in the assembled state that is ultimately the result of CLP domain being shorter in comparison to the original ELP-CLP system.

Short term future work will be focused on testing these hypotheses directly but synthesizing new ELP-CLP conjugates that possess specific melting temperatures and repeat lengths. More specifically, the melting temperature hypothesis is perhaps best tested through synthesis of $(Gly\text{-}Pro\text{-}Flp)_6GG$ where the repeat length is identical to that of $(GPO)_6GG$ but the melting temperature should be approximately 20°C higher.[9] We can may conclude that the melting temperature hypothesis is correct if nanoparticle formation occurs for this fluoroproline conjugate system.

Similarly, the chain length hypothesis can directly be tested by conjugation of ELP to $(GPP)_{10}GG$ CLP. The melting temperature of $(GPP)_{10}GG$ is approximately equal to that of $(GPO)_7GG$, but with a three more repeat lengths. It is reasoned that if

this chain length hypothesis is correct then we would expect the transition temperature of the ELP-CLP particle to not occur due to the decreased hydrophobic chain stretching that would result from the $(GPP)_{10}GG$ increased chain-chain repulsion.

With regard to longer term future work there are numerous things to explore with the ELP-CLP conjugate system. The short term future work will hopefully provide guidance regarding ways to continue lowering the hybridization temperature of the ELP-CLP conjugate. Similarly, the LCST of the ELP-CLP nanoparticle may be able to be fine-tuned for the purposes of on-demand drug delivery. For instance, it would be interesting to test an ELP that possessed five phenylalanine residues and one serine residue as way to inch up the transition temperature of the ELP-$(GPO)_7GG$ conjugate system. When a more idealized ELP-CLP nanoparticle that possesses the desired drug delivery properties is made, future experiments can be focused on testing the ability of these nanoparticles to successfully hybridize to collagen scaffolds. This can be done by through the incorporation of fluorescent dye moieties onto the a fraction of the nanoparticles surface by simply amide coupling chemistries with C-terminal carboxyl CLPs. This also includes encapsulation of dyes within the nanoparticles to determine the drug delivery capabilities of these ELP-CLP conjugates.

With regard to the future it is also important to consider possible issues with ELP-CLP nanoparticle hybridization to denatured collagen protein. This includes the possibility that a particle that is designed to partially unfold for hybridization may also have compromised stability and possibly releases drug cargo in an uncontrolled fashion. To this end a future nanoparticle system can be designed that is composed of both hybridizing CLP domains as well as particle stabilizing domains. It is envisioned

that such a system would also employ the use of hyperstable fluoroproline CLPs as is shown in Figure 4.1 below.

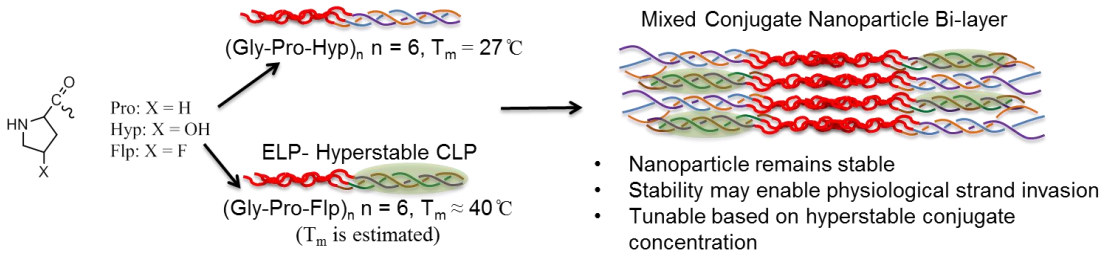

Figure 4.1: Envisioned mixed conjugate ELP-CLP nanoparticle. Fluoroproline CLPs would be used to stabilize the particle while hydroxyproline CLPs would be used as hybridization domains to denatured collagen protein.

As seen in Figure 4.1 a mixed conjugate nanoparticle system may offer a way to ensure cargo is retained within the particle while the particle still possesses hybridization capabilities.

REFERENCES

1. Lu, P. F.; Takai, K.; Weaver, V. M.; Werb, Z., Extracellular Matrix Degradation and Remodeling in Development and Disease. Cold Spring Harbor Perspectives in Biology. 2011, 3 (12), 1-24.

2. Järveläinen, H.; Sainio, A.; Koulu, M.; Wight, T. N.; Penttinen, R., Extracellular Matrix Molecules: Potential Targets in Pharmacotherapy. Pharmacological Reviews 2009, 61 (2), 198-223.

3. Allen, T. M.; Cullis, P. R., Drug delivery systems: Entering the mainstream. Science 2004, 303 (5665), 1818-1822.

4. Petros, R. A.; DeSimone, J. M., Strategies in the design of nanoparticles for therapeutic applications. Nature Reviews Drug Discovery 2010, 9 (8), 615-627.

5. Yu, S. M.; Li, Y.; Kim, D., Collagen mimetic peptides: progress towards functional applications. Soft Matter 2011, 7 (18), 7927-7938.

6. Wang, A. Y.; Mo, X.; Chen, C. S.; Yu, S. M., Facile modification of collagen directed by collagen mimetic peptides. Journal of the American Chemical Society 2005, 127 (12), 4130-4131.

7. Wang, A. Y.; Foss, C. A.; Leong, S.; Mo, X.; Pomper, M. G.; Yu, S. M., Spatio-temporal modification of collagen scaffolds mediated by triple helical propensity. Biomacromolecules 2008, 9 (7), 1755-1763.

8. Luo, T. Z.; Kiick, K. L., Noncovalent Modulation of the Inverse Temperature Transition and Self-Assembly of Elastin-b-Collagen-like Peptide Bioconjugates. Journal of the American Chemical Society 2015, 137 (49), 15362-15365.

9. Shoulders, M. D.; Raines, R. T., Collagen Structure and Stability. In Annual Review of Biochemistry, Annual Reviews: Palo Alto, 2009; Vol. 78, pp 929-958.

Appendix A

SUPPORTING INFORMATION FOR CHAPTER 2

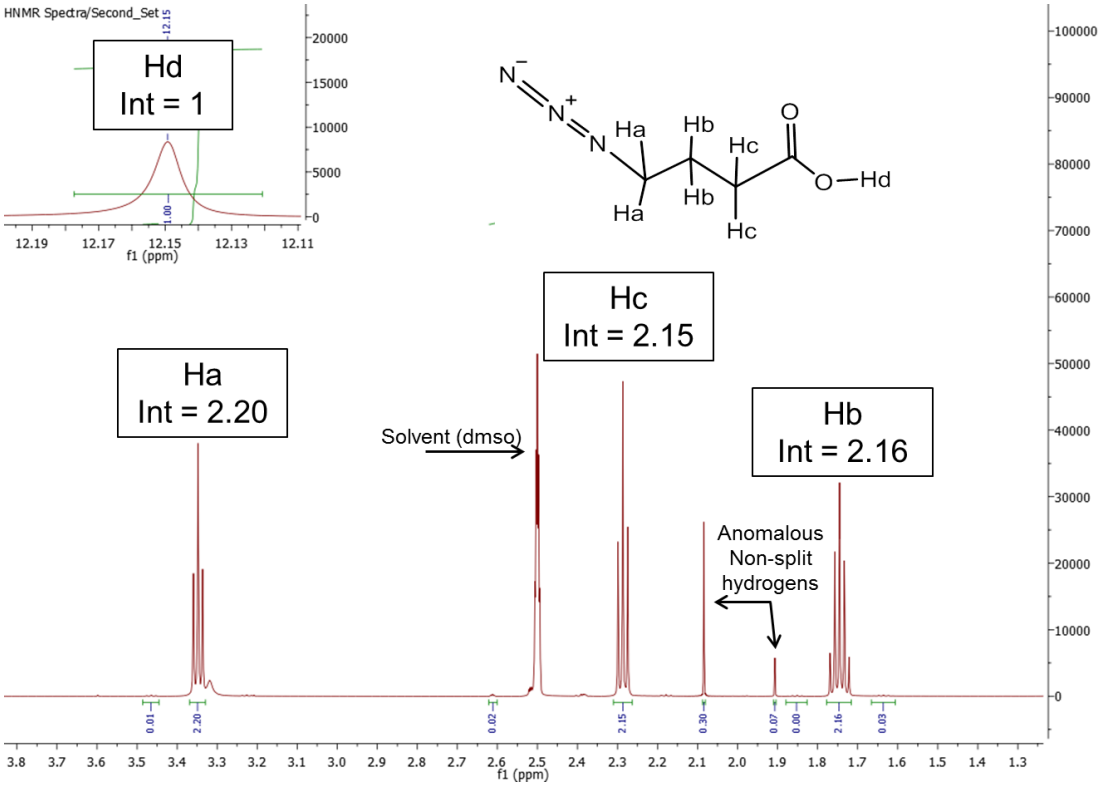

Figure A.1: [1]H-NMR spectroscopy of 4-azidobutanoic acid. Peaks are labelled according to the illustrated structure. The inset is of the carboxyl proton with large chemical shift. Integrations (abbreviated Int) match up well with the expected proton quantities on the molecule. The lack of significant perturbations of the Ha chemical shift indicate the reagent is considerably pure.

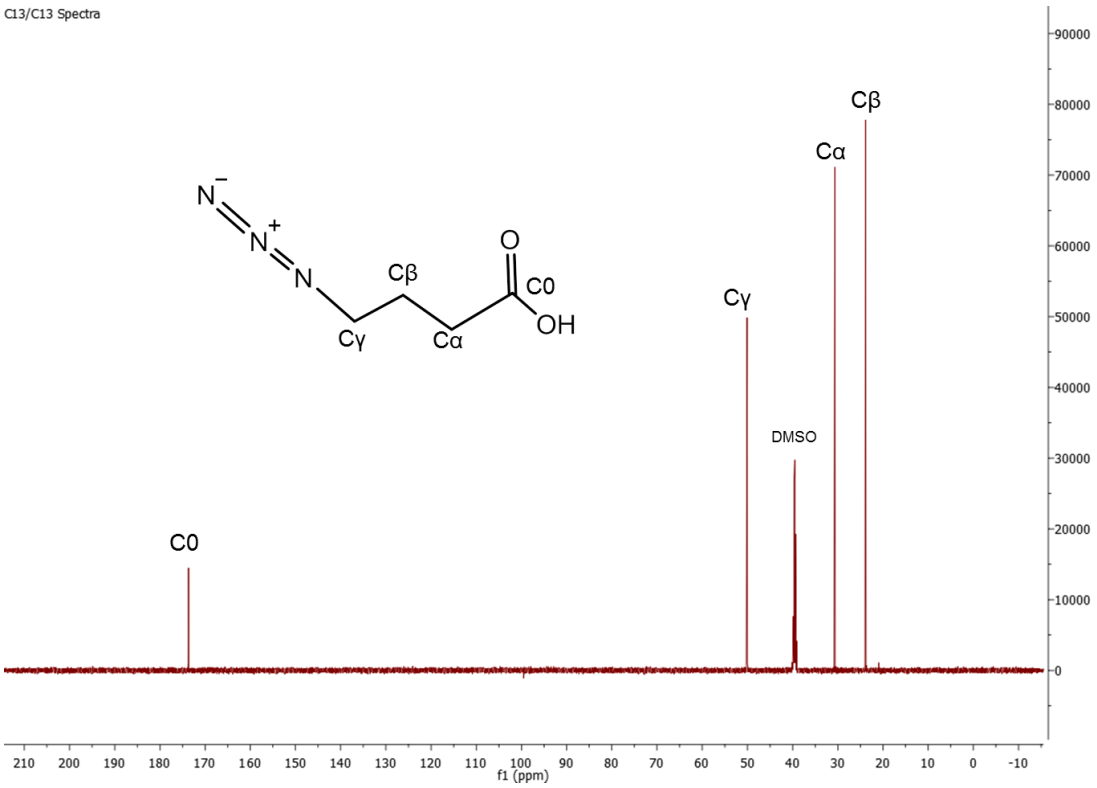

Figure A.2: ^{13}C-NMR spectroscopy of 4-azidobutanoic acid. The carbons labelled in the molecule are also labelled on the spectra peaks. The lack of significant perturbations to the chemical shift of the gamma carbon (proximal to the azide) indicate that the azides electron withdrawing properties are not significantly altered indicating the azide is intact and that the reagent is fairly pure. Additionally, the gamma carbon chemical shift adjacent to the azide is identical to the chemical shift of a carbon adjacent to an azide as reported in the literature (see Mahou, R., Wandrew, C. *Polyermers*. 4(1): 561-589. 2012).

Figure A.3: Example image of dissolution of ELP-CLP conjugate. In this image $(VPGFG)_6$-$(GPO)_6GG$ conjugate is attempted to be dissolved in pure water. The conjugate had previously been dialyzed with 500 Da dialysis tubing for 7 days. Since no visible spectrum chromophores are present in the conjugate, it is reasonable to conclude that the aberrant color is indicative of the copper molecules still present in the sample.

Appendix B

SUPPORTING INFORMATION FOR CHAPTER 3

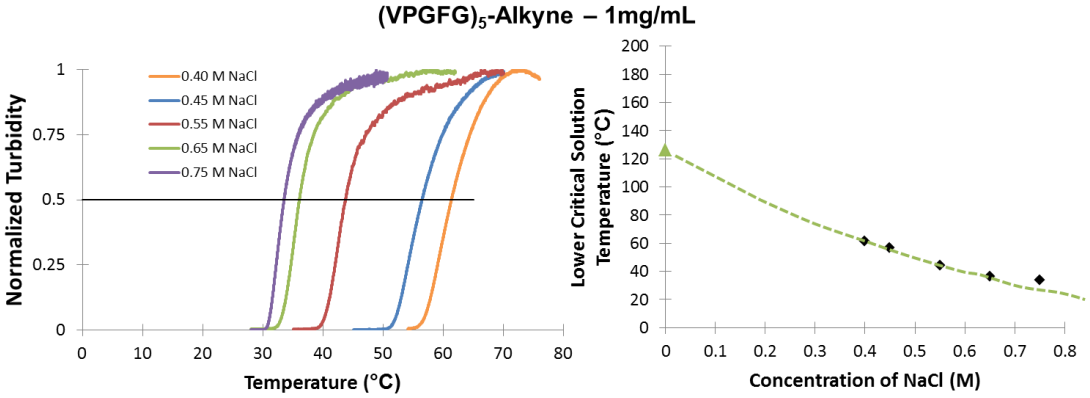

Figure B.1: Turbidity profiles for $(VPGFG)_5G$' (left) and the extrapolation of the found transition temperatures as a function of salt concentration (right) to the 0M transition temperature. The concentration of the ELP was 1mg/mL for every profile, and the heating rate was 5°C/min.

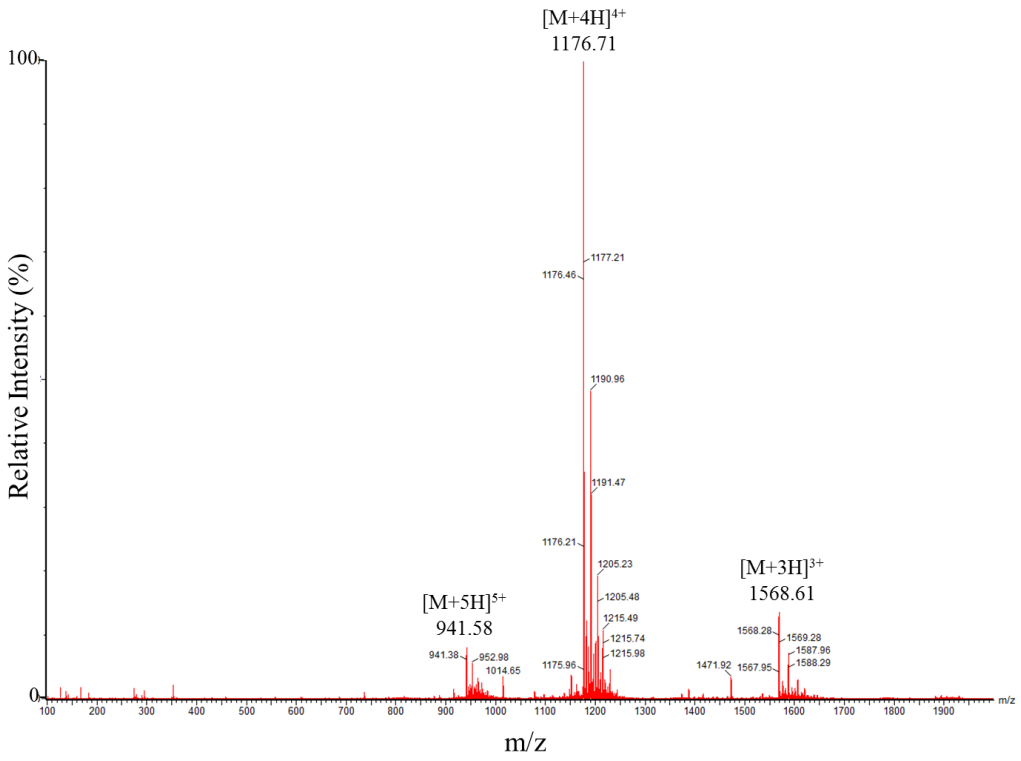

Figure B.2: Electrospray ionization mass spectrometry of RP-HPLC purified $(VPGFG)_6$-$(GPO)_6GG$. Expected mass = 4700.3 with the observed adducts m/z = 941.58 $[(M+5H)^{5+}$, calcd = 941.01], m/z = 1176.71 $[(M+4H)^{4+}$, calcd = 1176.08], and m/z = 1568.61 $[(M+3H)^{3+}$, calcd = 1567.7] .

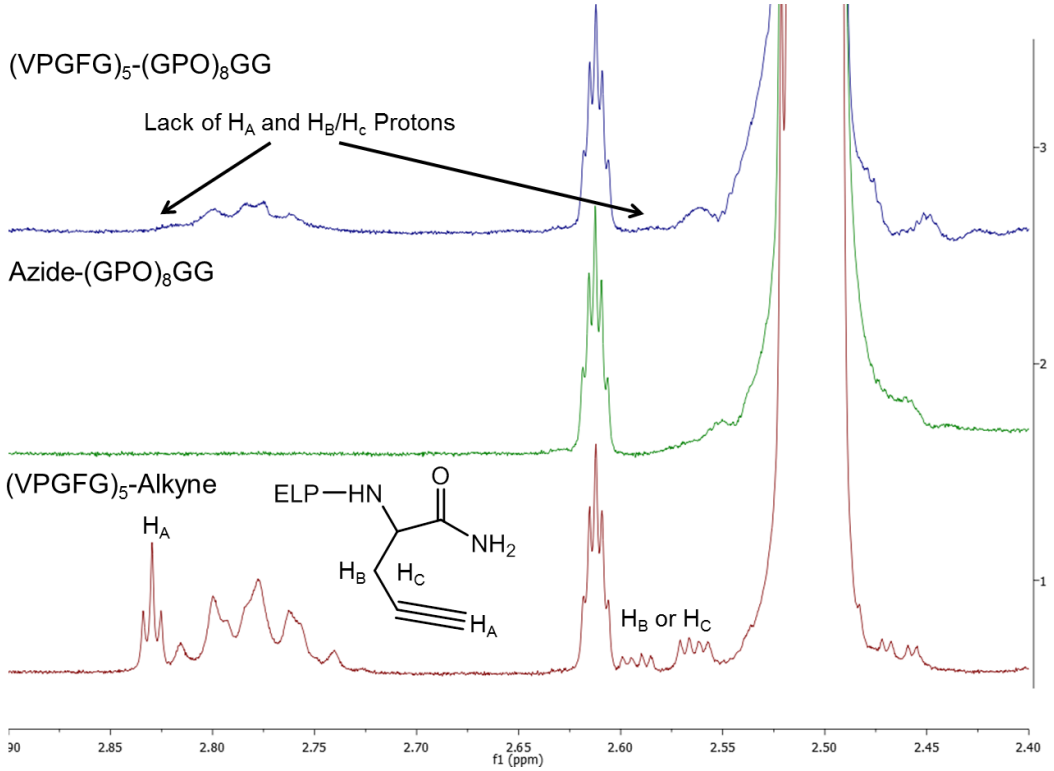

Figure B.3: ^{1}H-NMR spectroscopy of $(VPGFG)_5G$', Azide-$(GPO)_8GG$, and $(VPGFG)_5$-$(GPO)_8GG$. Note that the protons indicated in the ELP spectra appear to be consumed (Ha) or altered (Hb/Hc) according to the conjugate spectra.

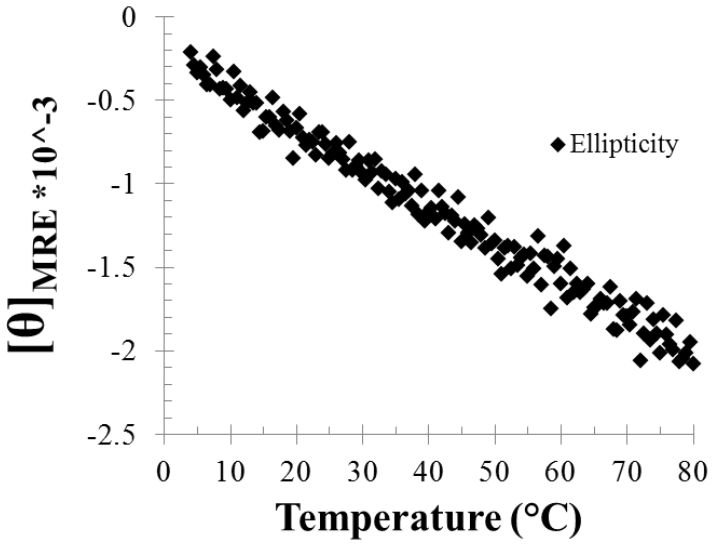

Figure B.4: Thermal melting curve of $(VPGFG)_6G$' analyzed at 225nm with at 10°C/hour heating rate. The concentration of the ELP was 0.35mM in 10mM DPBS.

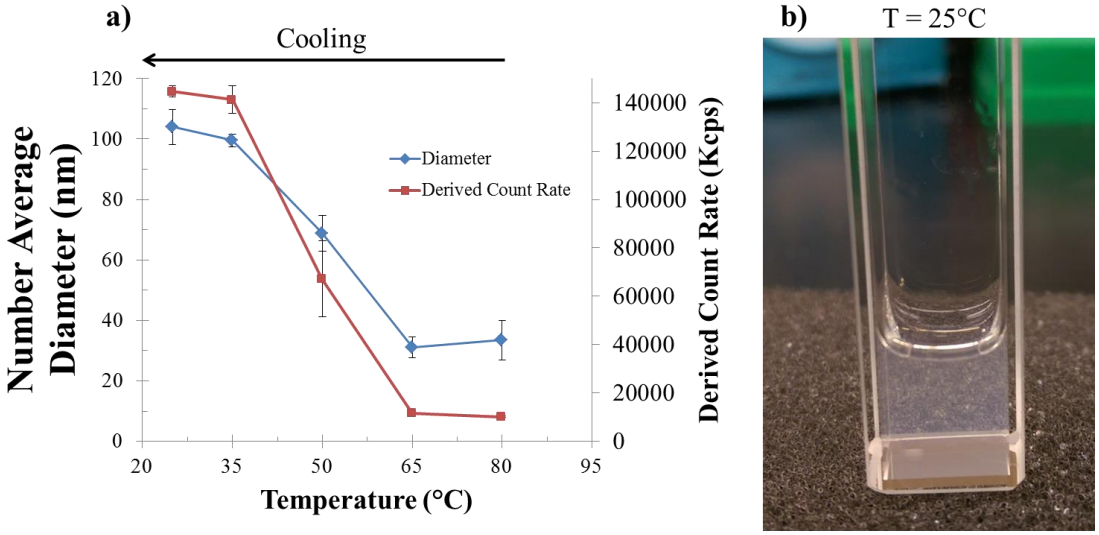

Figure B.5: Confirmation of nanoparticle formation of $(VPGFG)_6$-$(GPO)_7GG$ by a) dynamic light scattering and b) visual observation of dispersed particles.

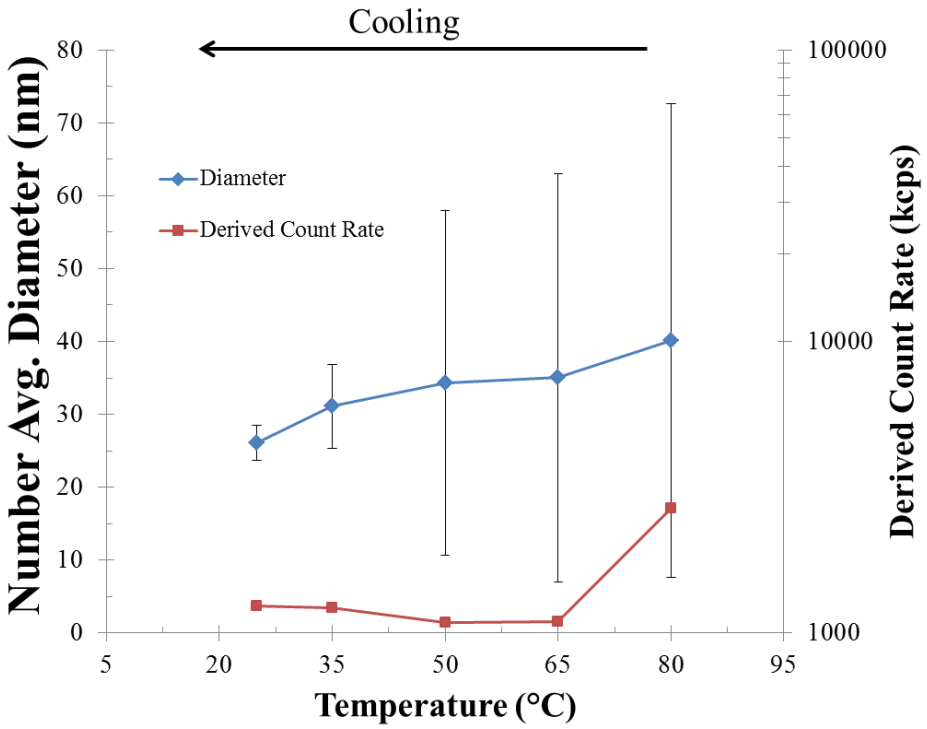

Figure B.6: Nanoparticle formation attempt of $(VPGFG)_6$-$(GPO)_6GG$ by dynamic light scattering. The low diameters as well as the significant low count rate indicate the lack of scattering that would be expected from a particle dispersion.

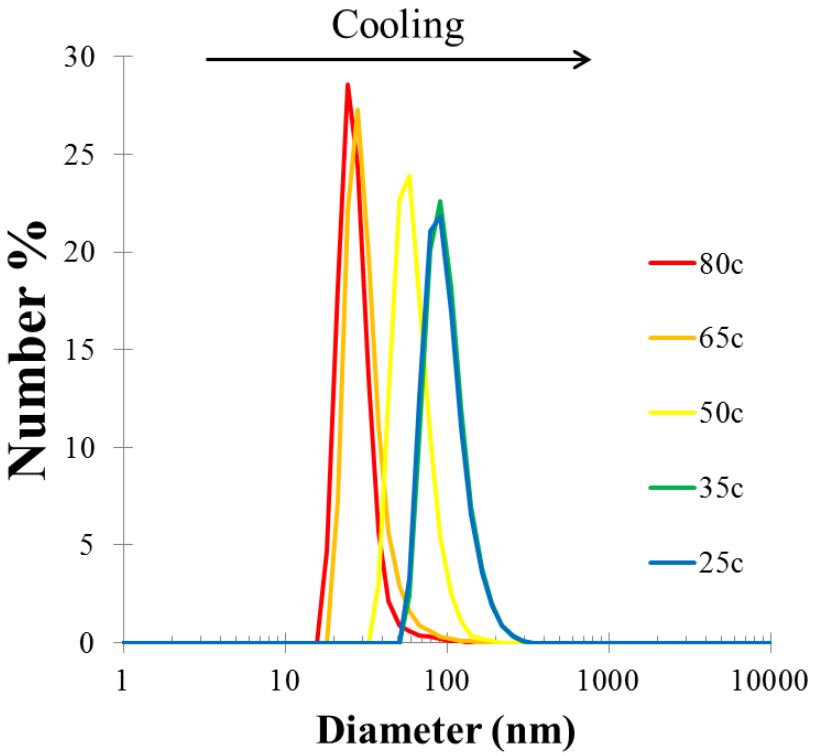

Figure B.7: Number distributions of particle sizes as particles begin to form upon cooling of$(VPGFG)_6$-$(GPO)_7GG$ conjugate.

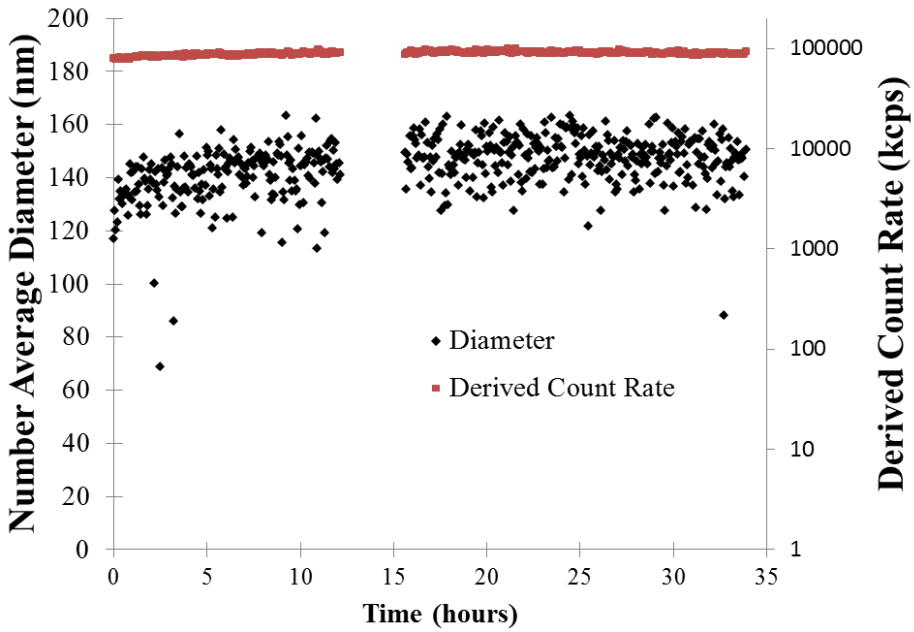

Figure B.8: $(VPGFG)_6$-$(GPO)_7GG$ nanoparticle stability at 25°C over a 34 hour analysis period. A three hour break in the data was due to use of the instrument for a separate nanoparticle system.

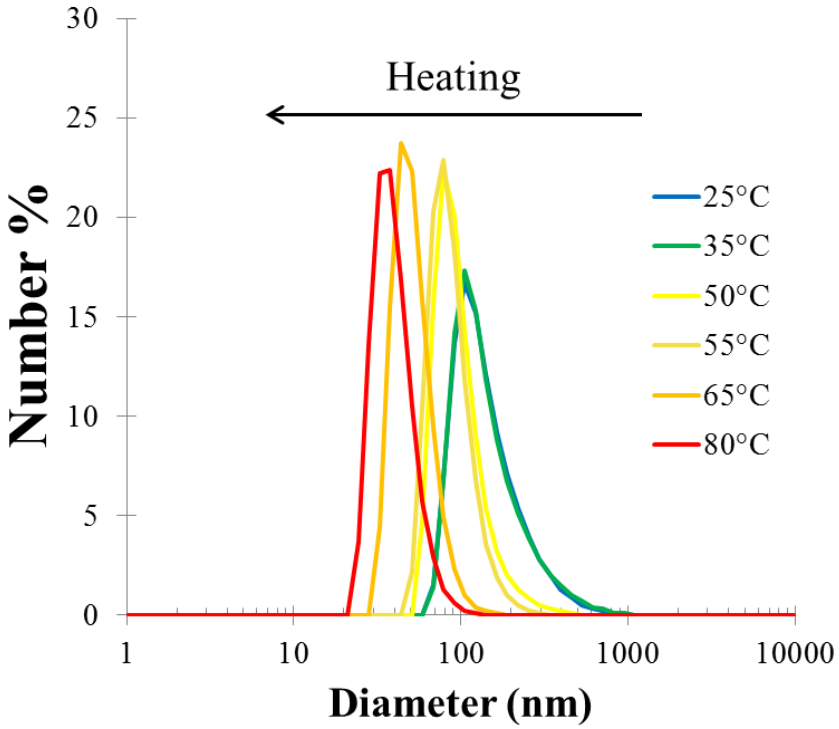

Figure B.9: Replicate data of number diameter distributions of $(VPGFG)_6$-$(GPO)_7GG$ particles as a function of heating. The trend is the same as that seen in Figure 3.7.

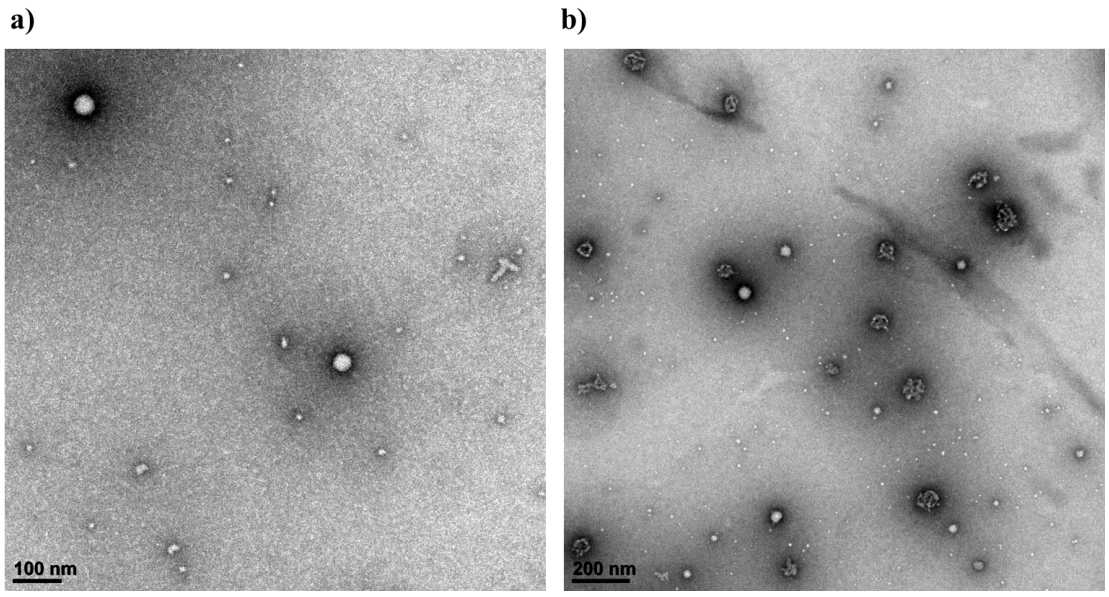

Figure B.10: $(VPGFG)_6$-$(GPO)_7GG$ nanoparticles stained with phosphotungstic acid (pH 7) that were incubated for thirty minutes at a) 25°C and b) 50°C.

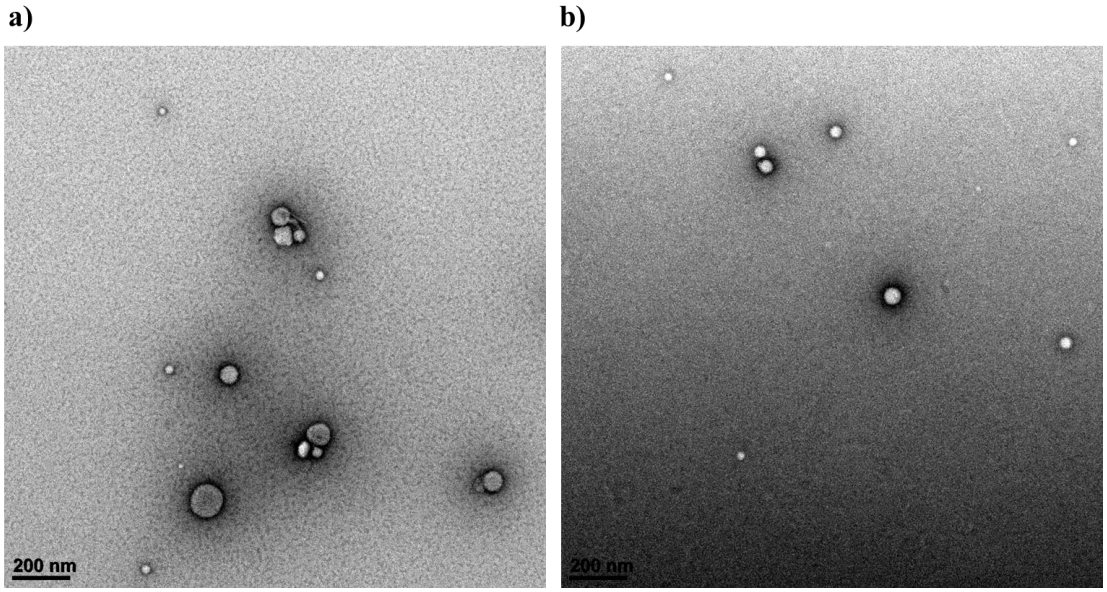

Figure B.11: $VPGFG)_6$-$(GPO)_7GG$ nanoparticles stained with uranyl acetate (pH 4.5) that were spotted at 25°C. a) and b) are different images from different grids but are from an identical sample.

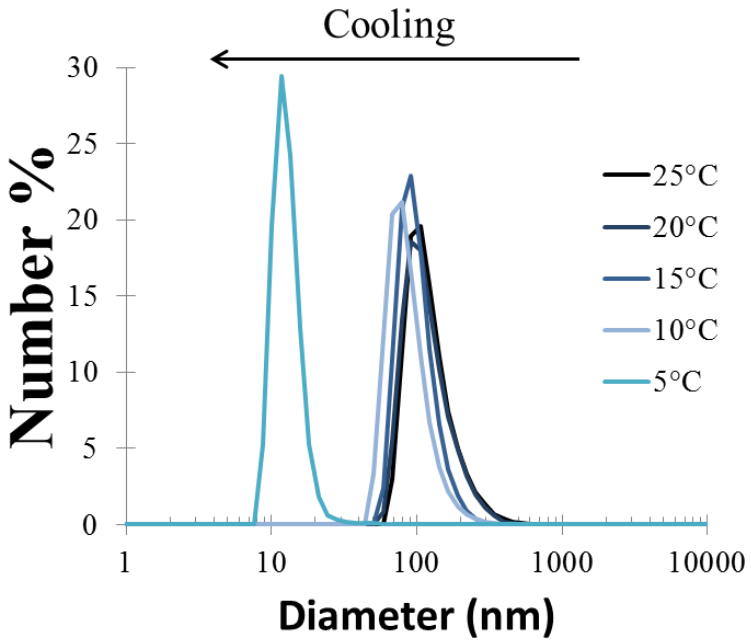

Figure B.12: Number distributions of particle diameters of $(VPGFG)_6$-$(GPO)_7GG$ as function of temperature as the particles are cooled from 25°C to 5°C. The data shown here are a replicate sample/batch of the data shown in Figure 3.9 and follow the same trends and possess apparently similar transition temperatures.

Appendix C

FIGURE REPRINT PERMISSIONS

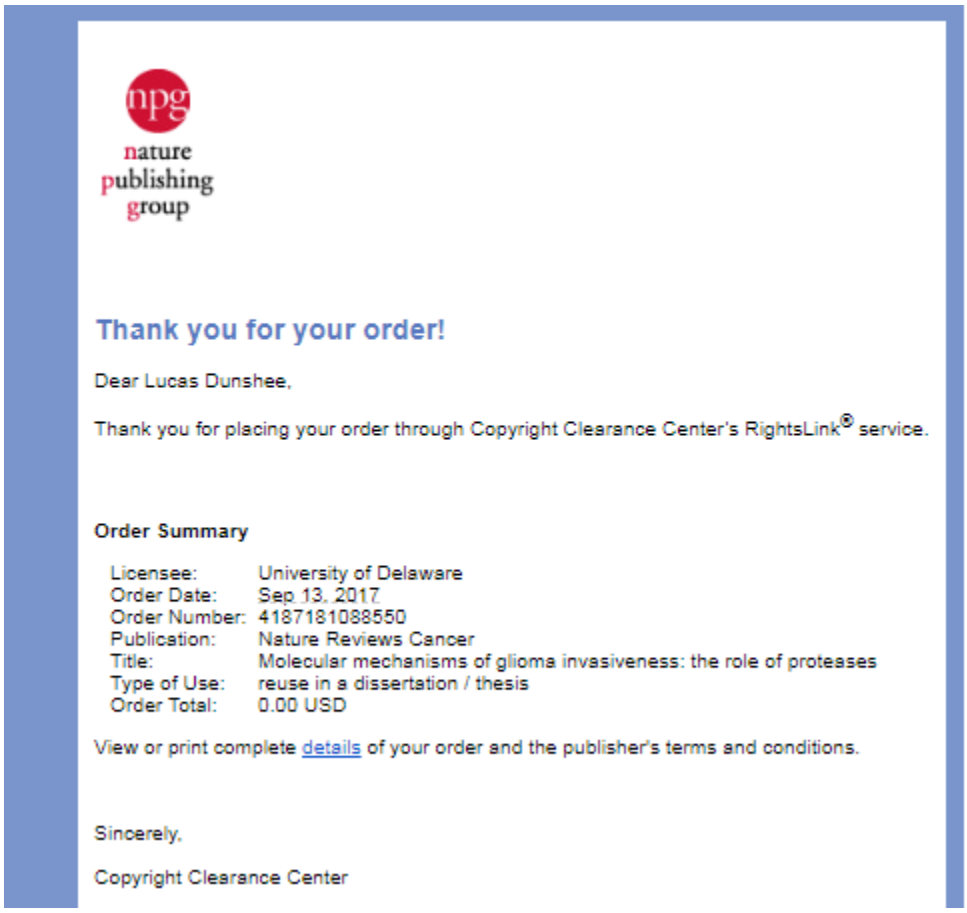

nature publishing group

Thank you for your order!

Dear Lucas Dunshee,

Thank you for placing your order through Copyright Clearance Center's RightsLink® service.

Order Summary

Licensee:	University of Delaware
Order Date:	Sep 13, 2017
Order Number:	4187181088550
Publication:	Nature Reviews Cancer
Title:	Molecular mechanisms of glioma invasiveness: the role of proteases
Type of Use:	reuse in a dissertation / thesis
Order Total:	0.00 USD

View or print complete details of your order and the publisher's terms and conditions.

Sincerely,

Copyright Clearance Center

Thank you for your order!

Dear Lucas Dunshee,

Thank you for placing your order through Copyright Clearance Center's RightsLink® service.

Order Summary

Licensee:	University of Delaware
Order Date:	Oct 6, 2017
Order Number:	4202901183129
Publication:	Soft Matter
Title:	Collagen mimetic peptides: progress towards functional applications
Type of Use:	Thesis/Dissertation
Order Total:	0.00 USD

View or print complete details of your order and the publisher's terms and conditions.

Requesting Permission

Anyone may, without requesting permission, use original figures or tables published in PNAS for noncommercial and educational use (i.e., in a review article, in a book that is not for sale), provided that the full journal reference is cited and, for articles published in volumes 90–105 (1993–2008), "Copyright (copyright year) National Academy of Sciences." Commercial reuse of figures and tables (i.e., in promotional materials, in a textbook for sale) requires permission from PNAS.

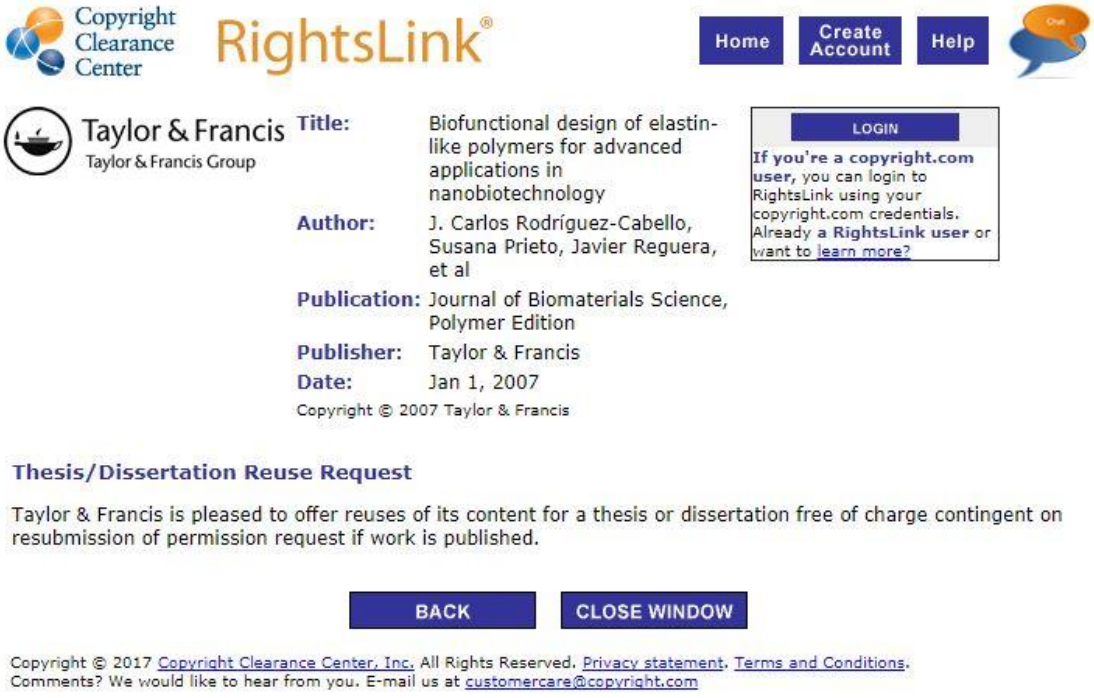

Copyright Clearance Center RightsLink®

Home | Create Account | Help

Taylor & Francis
Taylor & Francis Group

Title: Biofunctional design of elastin-like polymers for advanced applications in nanobiotechnology

Author: J. Carlos Rodríguez-Cabello, Susana Prieto, Javier Reguera, et al

Publication: Journal of Biomaterials Science, Polymer Edition

Publisher: Taylor & Francis

Date: Jan 1, 2007

Copyright © 2007 Taylor & Francis

LOGIN

If you're a copyright.com user, you can login to RightsLink using your copyright.com credentials. Already a RightsLink user or want to learn more?

Thesis/Dissertation Reuse Request

Taylor & Francis is pleased to offer reuses of its content for a thesis or dissertation free of charge contingent on resubmission of permission request if work is published.

BACK | CLOSE WINDOW

Copyright © 2017 Copyright Clearance Center, Inc. All Rights Reserved. Privacy statement. Terms and Conditions.
Comments? We would like to hear from you. E-mail us at customercare@copyright.com